Electronic Theses and Dissertations, 2004-2019

2011

Encapsulated Nanostructured Phase Change Materials For Thermal Management

Yan Hong
University of Central Florida

STARS Citation

Hong, Yan, "Encapsulated Nanostructured Phase Change Materials For Thermal Management" (2011). *Electronic Theses and Dissertations, 2004-2019*. 2052.
https://stars.library.ucf.edu/etd/2052

ENCAPSULATED NANOSTRUCTURED PHASE CHANGE MATERIALS FOR THERMAL MANAGEMENT

by

YAN HONG
M.S. General Research Institute for Nonferrous Metals, 2007
B.S. Xi'an Jiaotong University, 2003

A dissertation submitted in partial fulfillment of the requirements
for the degree of Doctor of Philosophy
in the Department of Mechanical Materials and Aerospace Engineering
in the College of Engineering and Computer Science
at the University of Central Florida
Orlando, Florida

Spring Term
2011

Major Professor: Ming Su

ABSTRACT

A major challenge of developing faster and smaller microelectronic devices is that high flux of heat needs to be removed efficiently to prevent overheating of devices. The conventional way of heat removal using liquid reaches a limit due to low thermal conductivity and limited heat capacity of fluids. Adding solid nanoparticles into fluids has been proposed as a way to enhance thermal conductivity of fluids, but recent results show inconclusive anomalous enhancements in thermal conductivity. A possible way to improve heat transfer is to increase the heat capacity of liquid by adding phase change nanoparticles with large latent heat of fusion into the liquid. Such nanoparticles absorb heat during solid to liquid phase change. However, the colloidal suspension of bare phase change nanoparticles has limited use due to aggregation of molten nanoparticles, irreversible sticking on fluid channels, and dielectric property loss.

This dissertation describes a new method to enhance the heat transfer property of a liquid by adding encapsulated phase change nanoparticles (nano-PCMs), which will absorb thermal energy during solid-liquid phase change and release heat during freeze. Specifically, silica encapsulated indium nanoparticles, and polymer encapsulated paraffin (wax) nanoparticles have been prepared using colloidal method, and dispersed into poly-α-olefin (PAO) and water for high temperature and low temperature applications, respectively. The shell, with a higher melting point than the core, can prevent leakage or agglomeration of molten cores, and preserve the dielectric properties of the base fluids. Compared to single phase fluids, heat transfer of nanoparticle-containing fluids have been significantly enhanced due to enhanced heat capacities. The structural integrity of encapsulation allows repeated uses of nanoparticles for many cycles.

By forming porous semi crystalline silica shells obtained from water glass, supercooling has been greatly reduced due to low energy barrier of heterogeneous nucleation.

Encapsulated phase change nanoparticles have also been added into exothermic reaction systems such as catalytic and polymerization reactions to effectively quench local hot spots, prevent thermal runaway, and change product distribution. Specifically, silica-encapsulated indium nanoparticles, and silica encapsulated paraffin (wax) nanoparticles have been used to absorb heat released in catalytic reaction, and to mitigate the gel effect during polymerization, respectively. The reaction rates do not raise significantly owing to thermal buffering using phase change nanoparticles at initial stage of thermal runaway. The effect of thermal buffering depends on latent heats of fusion of nanoparticles, and heat releasing kinetics of catalytic reactions and polymerizations. Micro/nanoparticles of phase change materials will open a new dimension for thermal management of exothermic reactions.

ACKNOWLEDGMENT

I would like to express my sincere gratitude to my advisor, Dr. Ming Su for his guidance, inspiration, encouragement and support. I appreciate the guidance and help from my co-advisor Dr. Louis Chow. I learned a lot of useful knowledge from our weekly meeting in the past three years. I thank my dissertation committee members Dr. Kevin Coffey, Dr. Patrick Schelling, and Dr. Helge Heinrich for thoughtful discussion and valuable suggestions.

I thank Dr. Wei Wu, who has helped me on heat transfer measurements; Dr. Shujiang Ding, who has helped me on synthesis of polymer encapsulated nanoparticles; Dr. Jianjun Hu at Air force Research Lab, who has helped me on in-situ heating transmission electron microscopy. Without their great help and generous support, this dissertation will not be possible.

I want to thank Dr. Liyuan Ma, Dr. Minghui Zhang, Dr. Qi Zhang, Dr. Zhaoyong Sun, and lab fellows Chaoming Wang, Mainul Hossain, and Zeyu Ma.

I also want to thank administrative staffs at NanoScience Technology Center (NSTC), Advanced Materials Processing and Analysis Center (AMPAC), and Department of Mechanical, Materials and Aerospace Engineering (MMAE).

TABLE OF CONTENTS

LIST OF FIGURES

LIST OF TABLES

CHAPTER 1 INTRODUCTION

1.1 Background of This Study

Heat transfer fluids (HTFs) have many industrial and civil applications, which include energy storage, heat transfer and electronic cooling. Traditional HTFs such as water, glycols and fluorocarbons, however, have inherently poor heat transfer performance due to their low thermal conductivities. Researches are being carried out to improve the heat transport properties of HTFs. High thermal conductivity materials, such as silver, copper, alumina, CuO, SiC and carbon nanotubes have been added into HTFs for enhancing heat transfer properties based on Maxwell heat transfer law established in 19 century.[1] At first, microscale solid particles with millimeter sizes were blended into base fluids to make slurries. But, those large particles usually cause troublesome problems such as abrasion, phase separation and clogging, etc., which substantially limits the practical applications. The situation changed when Choi and his colleagues revisited this field with nanoscale metallic particles and carbon nanotube suspensions.[2] They suspend various metal and metal oxides nanoparticles in several different fluids aiming to find promising results that coincident with theoretical calculations, however, Chen argued that when the size of particle is smaller than the average free path of heat carriers (electrons, phonons, or molecules), the heat carrier transport is ballistic or non-local, and Fourier's law is not applicable.[3-4] In fact, thermal conductivity decreases rapidly with decreasing particle size.[5] There is no systematic experimental investigation on size dependent conductivity. On the other hand, the large interface areas between the nanoparticles and the heat transfer fluids increase the heat transfer rate,[6] so nanosheets, nanorods, and nanowires, which have large surface areas, perhaps are favorable to significantly increase the thermal conductivity of nanofluids. Many mechanisms have been proposed to describe anomalous thermal conductivity increase in nanofluids, such as Brownian motion of nanoparticles; high thermal conductive liquid layer at liquid/solid particle interface; nanoparticle clustering in nanofluids, etc. Brownian motion of nanoparticles is too slow to directly transport a significant amount of heat through a nanofluid, however, it could have an important indirect role to produce a convection-like micro-environment around the nanoparticles and particle cluster to increase the heat transfer; the presence of an ordered interfacial liquid molecule layer seems to be not solely responsible for the anomalous increase of thermal conductivity, especially this mechanism works well only when the particle size is smaller than 10 nm; nanoparticles clustering have both positive and negative effects on the increase of the thermal conductivity.[7] There was a concerted effort to conclusively establish whether the anomalous increase of thermal conductivity is real. More than fifteen groups of researchers round the globe participated in collecting indigenous data on the measurement of thermal conductivity for identically prepared nanofluid. The data was collected in a website and analyzed and reported in the Journal of Applied Physics late in 2009.[8] The thermal conductivity of the nanofluids increases with particle concentration and aspect ratio. The systematic difference in the absolute values is negligible among the various experimental approaches and such difference tends to disappear when the data are normalized. Recent effective medium theory studied by Nan et al. was found to be in good agreement with the experimental data, there is no anomalous enhancement of thermal conductivity in the nanofluids.[9]

Until recently, the use of nanoscale phase change materials (PCMs) as additives in base fluids attracts much attention by taking advantages of latent heat of fusion, the effective heat capacity of the fluids can be greatly enhanced while the fluidic properties of the fluids still remain. There are a lot of PCMs such as metals, salt hydrates, fatty acids, esters, polyethylene glycols and paraffin. Microscale or nanoscale encapsulated phase change materials provide portable heat storage and transfer system by coating with protective shells around those particles. The particles can be dispersed into a single phase HTF. With the use of nanoparticles of PCMs with high thermal conductivity, the heat capacity of nanofluids is expected to be improved.

1.2 Rationales behind the Nano-PCMs Suspension

Since phase change materials have large heat capacities than base fluids, as shown in Table 1, it is then a straightforward logic to increase the heat capacity of fluids by adding phase change materials.[10-12] However, if solid particles of micrometer diameters are added into bases fluids to make suspensions, the increase in thermal properties of the suspensions are insignificant even at high particle loading, and at the mean time, large particles may cause many problems:

1) Large particles are easy to settle out from the base fluids, especially in low speed circulation or intermittent working conditions, which will not only lose the enhancement in the heat capacity, but also form a sediment layer at the surface of channels, increasing the resistance and impairing the heat transfer property of the base fluids. Further more, the large size of particles or agglomerates of these particles cause severe clogging problems, i.e. at low flow rate of base fluids or in small microchannels;

2) The erosion of the pipelines by the coarse and stiff particles increases rapidly due the large particles carry too much momentum and kinetic energy, which may cause damage to the surface, especially when the speed of the circulation increases;

3) Noticeable heat capacity and heat transfer coefficient enhancement are resulted from high particle concentration, which leads to increase in viscosity.

Table 1. Heat capacities of common phase change materials and coolants.

Materials		Heat capacity (J/g·K)	Latent heat of fusion (J/g)	Viscosity at 25ºC (mPa·s)
Heat transfer fluid	Water	4.2	-	0.89
	Ethylene glycol	0.59	-	16.6
	Engine oil	2.0	-	20
	FC-72	1.1	-	0.64
	Poly-Alpha-Olefin	2.7	-	7.3
Phase change materials	n-Octadecane	-	243.5	-
	Indium	-	28.52	-
	$NaNO_3/KNO_3$	-	100.7	-
	Stearic acid	-	211.6	-

A large variety of nanoscale materials have been made, with outstanding features such as large surface area to volume ratio, small sizes, and high mobility. After nanoparticles are dispersed into the base fluid, the interactions between nanoparticles or between nanoparticles and agglomeration after melting may also result in the clogging of microchannels, especially for dielectric immersed cooling system, the conductive metal nanoparticles may result in short circuit during circulation. As a result, it is necessary that the phase change materials be encapsulated in high dielectric constant materials prior dispersing into base fluids so as to maintain the dielectric properties.

The nano-PCMs have been made and encapsulated using the state-of-the-art colloidal methods. The thermo-physical properties of colloid suspension are measured by differential scanning calorimeter (DSC) and tested on a heat transfer loop. This work is innovative for several reasons: (1) enhancement of heat transfer through the latent heat of nano-PCMs is more straightforward and practical than that through the thermal conductivity; (2) non-melting shells prevent leakage or aggregation of molten nanoparticles and reaction of nanoparticles with liquids; and (3) encapsulation of metal nanoparticles inside dielectric shells allows immersion cooling of electronic devices.

1.3 Objective of Present Research

The objectives of this research are as follows: 1) develop mass production methods of preparing nano-PCMs suspensions; 2) investigate the physical and thermal properties of nano-PCMs; 3) maintain the dielectric properties of the base fluid; 4) find the physical mechanism behind the relative heat capacity enhancement of nano-PCM suspensions through the investigation of the effects of nanoparticles properties, and heat transfer loop test; 5) reduce the supercooling of nano-PCM by providing a suitable nucleate sites for heterogeneous nucleation; 6) monitoring the thermal runaway of exothermic chemical reactions by using phase change nanoparticles.

1.3.1 Develop mass production methods of nano-PCM suspensions

There have been many nanoparticles synthesis methods as documented in literature, such as chemical reduction, thermal decomposition, laser ablation, chemical vapor deposition, lithography, sputtering, etc. However, most of them are still in gram level and therefore are not suitable for mass production due to the high cost, low yield, and many other factors. Herein, we developed a two-step method for synthesis of encapsulated single component and multi-component low melting temperature metallic phase change nanoparticles and a one-step method for synthesizing polymeric encapsulated phase change nanoparticles. Those methods can be classified as miniemulsion or nanoemulsion methods, where bulk phase change materials are mixed with high viscous liquid and heated above the melting points of those phase change materials. The liquid phase change materials are emulsified into nanoscale under the vigorous stirring or sometimes assisted by high power sonication. The as formed nanoparticles are then stabilized by surfactant and encapsulated by nonmelting shell later or directly encapsulated with high-melting-point shell to prevent from agglomeration after cooling down to room temperature in chapter 3.

1.3.2 Physical property of nano-PCMs colloidal suspension

The solid-liquid phase change behavior, size distribution, viscosity and stability are investigated in chapter 4. Encapsulated phase change nanoparticles need to be both physically and thermally stable after many cycles repeating, an in-situ transmission electron microscopy (TEM) study has been done on the stability of core-shell structure on a heating stage inside the TEM chamber. The phase change behavior and stability can be directly observed by STEM mode and EDX mode.

1.3.3 Dielectric properties of colloid suspension containing nano-PCM

For some microelectronic cooling system, the direct immerse cooling needs dielectric coolant, the incorporating of bare metallic nanoparticles may cause short circuit and damage the devices due to the clustering of nanoparticles. Therefore, the phase change nanoparticles have been encapsulated and the dielectric property has been measured using dielectric measurement equipment (LCR-meter) so as to prove that the dielectric properties of the base fluid have been reserved or enhanced.

1.3.4 Heat transfer behavior investigation

The heat transfer behavior is investigated by a self-built heat loop test and differential scanning calorimetry in chapter 4. At the same flow rate of fluid, the heat that can be removed depends on the heat capacity of the coolant, while the heat capacity can be greatly enhanced by suspending phase change nanoparticles by fully utilizing the large latent heat of fusion. The heat transfer coefficient and heat capacity enhancement of encapsulated indium and wax nano-PCMs colloidal suspensions have been studied. On the other hand, the efficiency of phase change during the heat loop test was also investigated by comparing the resident time in the heat exchanger and the melting time of nanoparticles, the fast melting speed will help the efficiency of heat capacity enhancement.

1.3.5 Reduce the supercooling

The relative heat capacity enhancement is depending on latent heat of fusion of phase change materials and supercooling. The latent heat of fusion is a fixed value, but the supercooling will greatly affect the enhancement. Supercooling is a common phenomenon exists in nanoscale phase change materials, which is determined by the nucleation energy for the forming of solid nuclei, which can be greatly eliminated by providing suitable nucleate sites for heterogeneous nucleation. A porous semicrystalline shell has been provided to reduce the supercooling. Some other effects also have been studied in chapter 5.

1.3.6 Thermal runaway monitoring

Thermal runaway of an exothermic chemical reaction usually results in server temperature ramping without suitable control. The thermal runaway affects the yield, selectivity and safety of many reactions including catalytic reaction, polymerization, and electrochemical energy conversion, etc. The thermal runaway of heterogeneous catalytic reactions can cause side reactions, catalyst deactivation, and loss in productivity or selectivity, and lead to explosion if released reaction heat cannot be removed quickly. A similar effect in polymerization is also called auto-acceleration or gel effect, in which positive feedback will speed up polymerization, and result in heat accumulation due to increased viscosity. In the case of electrochemical reaction, thermal runaway is the major cause of battery explosion due to temperature rise.

The temperature of heterogeneous reactions is controlled by proportional-integral-derivative (PID) unit, where temperature around or inside a reactor will be monitored continuously. However, the performance of temperature control unit is not sufficiently small to detect microsize hot spots. The heat conduction delay from hot spots to thermal couple leads to ineffectiveness in temperature control. An effective way to monitor the thermal runaway and quench local hot spots is to add phase change materials that undergo phase change at certain temperature where the latent heat of fusion will contribute significantly to the heat capacity of mixture and suppress thermal runaway.

Chapter 6 describes the use of encapsulated phase change nanoparticles to control the thermal runaway of catalytic reactions and polymerizations, where nano-PCMs change phases from solid to liquid when absorbing heat released from those exothermic reactions. The core materials are metal nanoparticles or paraffin wax nanoparticles, which change phases at suitable temperature. The high melting point shells are made of silica or polymer, and are stable at operating conditions to prevent the leakage or oxidization of core material. Due to their small sizes, inert surfaces, and large heat-absorbing capabilities, nano-PCMs can be mixed homogeneously with solid catalysts or monomers to quench local hot spots before accumulation of heat energy at a large scale, thus breaking the positive feedback loop between the reaction rate and temperature, and postponing onset of thermal runaway by absorbing reaction heat. Two highly exothermic reactions, platinum catalyzed methanol oxidation, and polymerization of methyle methacrylate (MMA) have been used as examples to prove the generality of this approach.

CHAPTER 2 LITERATURE REVIEW

2.1 Importance of Thermal Management

The semiconductor industries are taking a large amount of efforts to reduce the size of the electronic devices. With the increase in calculation speed and reduction in the size, the growth in power density is expected to increase further over the next decade. The increasing power density indicates the thermal management plays an important role in determining the future development. The heat load in process equipment by a thermal management consortium also projects the increasing trend of power dissipation. Advanced cooling technique is required to meet this stringent thermal requirement.[13]

The failure in electronics during operation occurs mainly due to several factors and is shown in Figure 1. The major factor that results failure in electronics is temperature, the vibration, humidity and dust only play a minor role. The minimize package dimensions while increasing powder density have pushed the use of air cooling with heat sink or mechanical fan to the limit, therefore, thermal management is a key enabling technology in the development of advance electronics. It is a necessary part of any competitive power density environment.

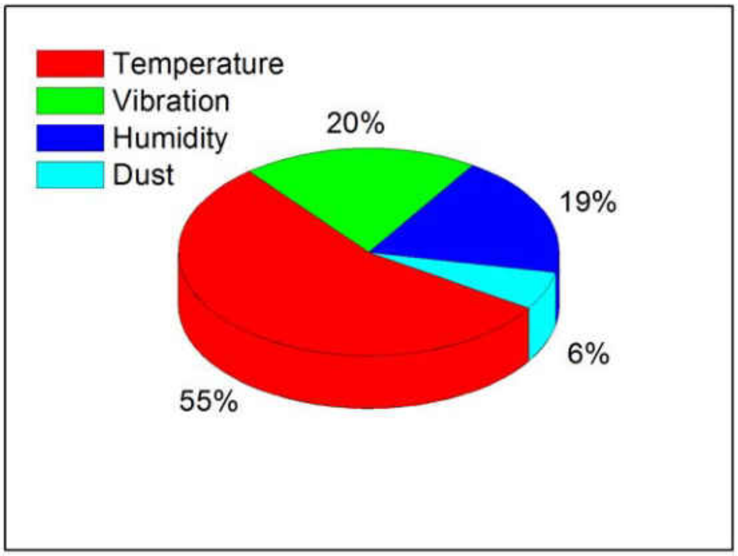

Figure 1. Failure in electronic components.

The high chip temperature results in thermal failures such as mechanical stresses focus, thermal de-bonding and thermal failure. The mean time of failure in electronics is exponentially proportional to the reciprocal of temperature increase on electronics:[14]

$$MTF = AJ^2 \exp(E_a / KT) \tag{1}$$

The plotted curve is shown in Figure 2. When the temperature increases 10ºC, the mean time of failure will decrease for 60%; while the temperature increases for 20ºC, the mean time of failure will decrease for 75%.

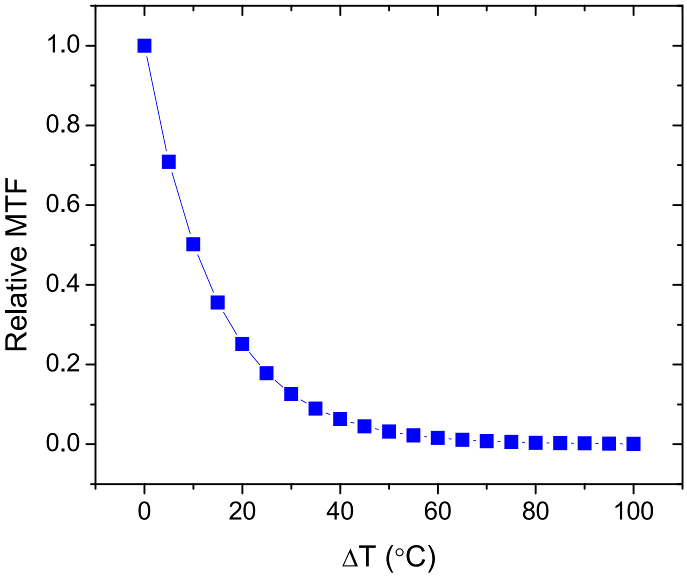

Figure 2. Relative mean time of failure of electronics versus temperature increase.

2.2 Thermal Management Technique

2.2.1 Classification of cooling methods

Practically, cooling technique is categorized into active cooling techniques and passive cooling techniques, Active cooling technique offer high cooling capacity assisted by mechanical enforcement. They allow temperature control that can be below ambient temperatures. Air or liquid jet impingement, forced liquid convection, spray cooling thermoelectric coolers and refrigeration systems are current cooling techniques.

Cooling methods can be classified into four broad categories in order of increasing on the heat transfer effectiveness by assuming that the temperature difference between the electronic surfaces and ambient is 80ºC (ambient and surface temperature are 20 and 100ºC, respectively): radiation and natural convection (155-1550 W/m^2), forced air-cooling (800-16000 W/m^2), forced liquid cooling(11000-930000 W/m^2), and liquid evaporation (15500-1400000 W/m^2).[15] The heat transferred for different methods are shown in Figure 3.

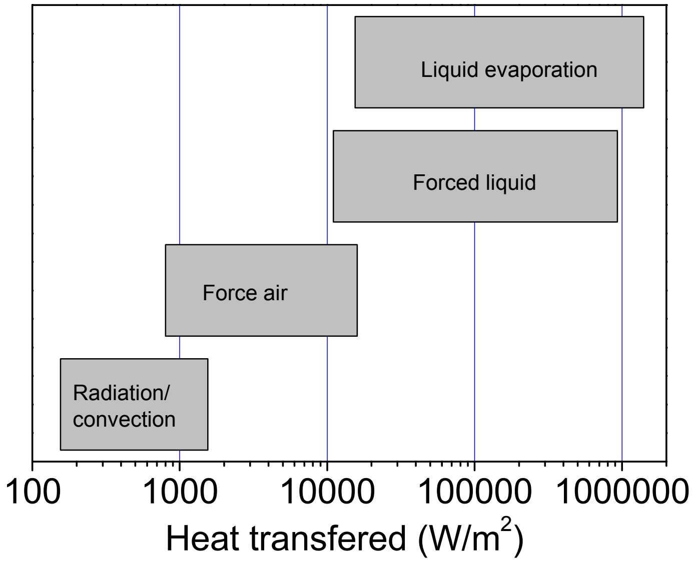

Figure 3. Range of conventional heat transfer modes.

So far, cooling method reported by various literatures can be classified into the following categories: air cooling, liquid cooling, heat pipes, refrigeration cooling, thermoelectric cooling, and phase change material based cooling, which are shown in Table 2. The chosen of cooling methods depends on heat removal requirement, working conditions, and device safety, etc. The cost is also considered as an important parameter in large industry productions.

Table 2. Various cooling methods and their applications.

Cooling method	Classification	Applications	References
Air cooling	Natural convection/radiation	Low power electronics	16-18
	Forced convection	Low power electronics	19
	Heat sink enhancement	Chip circuit boards	20
Liquid cooling	Emerge cooling	Microelectronic	21
	Pool boiling	Electronic equipment	22-24
	Jet impingement	High heat flux electronic	25-31
	Spray cooling	High flux chips	32
Heat pipes	Direct/indirect	Large heat flux cooling	33-35
Refrigeration cooling	High density cooling	Fusion power system/laser mirror	36
Thermoelectric cooling	Single stage	Pulsed operation device	37-39
	Multi stage	Hermetic devices	40
Phase change materials based cooling	Heat transfer	Portable devices	41-42
	Energy storage	Reduce fluctuations	43-45

Among the cooling methods, air cooling is the simplest and principal method. In many cases air flowing devices are in stalled at the bottom or top of a column of boards to provide sufficient cooling. Liquids have high heat transfer coefficients than gases for high power electronics. Liquid cooling can be both direct and indirect. Refrigeration cooling is usually used in large systems and work stations that need large efficiency. It is a low cost, reliable and mature technology and mostly applied in temperature range of -20 to 40°C. The thermoelectric cooling is a solid state heat pump, which can be used for temperature below ambient temperature application. A heat pipe is a heat transfer device by using large latent heat of liquid-vapor phase change property which capable of transferring large quantify of heat with a small temperature drop. The heat pipe cooling device consist evaporator, adiabatic and condenser sections. The evaporated gas will transport the heat from hot part to cold part, and condensed at cold part, the liquid will flow back to hot part by gravity and wick effect. This closed loop process continues as long as heat is applied. The solid-liquid phase change material can also be used to absorb heat from hot part and release heat to the cold part by using the unique properties of latent heat of fusion.

2.2.2 Mechanism of heat transfer in nanofluids

In classical theory, heat is transmitted by three distinct modes: conduction, convection, and radiation. In the last two decades, there have been many mechanisms emerged to interpret the measured thermal conductivity enhancement. However, most of them can be classified into two groups: conduction and convection. In the convection group, the explanations include Brownian motion of nanoparticles, the interfacial ordering of liquid molecules on the surface of nanoparticles.[46-50] The Brownian motion of nanoparticles could transfer the heat through the molecules convection movement, however, the larger time scale than that for the thermal diffusion of base liquid and weak temperature dependence on the Brownian motion of nanoparticles have suggested that it is not a dominant mechanism.[51] The effective thermal conductivity depends on the particle size, the small particle size will increase the interfacial resistance and lead to deterioration of the thermal conduction of nanofluids, therefore, the liquid molecular layering mechanism has also been excluded.[52-53] Many experiments have been carried out with nanoparticles formed from those high thermally conductively materials including aluminum oxide (Al_2O_3), copper (Cu), copper oxide (CuO), gold (Au), silver (Ag), silicon carbide (SiC), titanium carbide (TiC), titanium oxide (TiO_2), and carbon nanotubes. The base fluids used most commonly are water, engine oil, and ethylene glycol.[7, 54-56] Those studies show that the nanoparticles structuring or clustering theory gives good agreement with Maxwell model for aggregates suspensions.

It should be noted that the enhancement in thermal conductivity alone is not sufficient enough to prove that nanofluids can improve the heat transfer ability. The performance in convective environments is a stronger evidence to evaluate the nanofluids. Few studies have been done on investigating the natural convection of nanofluids compared to forced convection and pool boiling. Because the viscosity will be increased by adding nanoparticles, therefore, natural convection in nanofluids usually results in decreased heat transfer coefficient.[57] However, some numerical and experimental results showed that enhancement can be achieved by adding copper nanoparticles in ethylene glycol, and by adding alumina nanoparticles in water.[58-59] The reason is probably due to random motion of nanoparticles. Forced convection heat transfer is widely used in nanofluids, but there is limited literature to fully explains this behavior in nanofluids. Furthermore, several of the research papers available seem to contradict each other as some data shows an increase in convection as the particle volume fraction is increased,[60-61] while other result shows little enhancement or even a reverse effect as the particle density and concentration were increased.[62]

2.3 Phase Change Materials

2.3.1 Phase change materials for energy storage

Since many energy sources such as solar energy are intermittent in nature, energy storage plays important roles in conserving extra available energy. Solar energy is only available during the day. Therefore, efficient thermal energy storage can collect the excess heat for later use. Similar problems arise in heat recovery systems where the waste heat generation rates and availability periods are different. Hence, the successful application of solar energy and waste heat recovery depend on the appropriate method of energy storage that used.

The most common method of thermal energy storage is the sensible heat method. For example, water is still used in liquid based heat storage systems, while a rock bed is used for air based systems. These methods are capable of providing space heating during the night from the stored heat during the day. However, they are heavy and bulky in size. Solid to liquid phase change materials adsorb a lot of heat energy during phase changes without temperature rise, the large latent heat of fusion compared to heat capacity is promising for thermal energy storage and heat transfer.[63-65] Unlike the sensible heat storage method, the phase change materials storage method provides much higher storage density, and with a smaller temperature difference when storing and releasing heat.[66-67] Many different PCMs have been studied including paraffin waxes, salt hydrates, fatty acid, eutectic of compounds.[68-69] Depending on applications, PCMs are selected based on their melting points (Table 3). For example, PCMs below 15ºC are used for air conditioning applications, while PCMs that melt above 90ºC are used for absorption refrigeration. All other materials that melt between these two temperatures can be applied in solar energy storage applications.

Table 3. Thermophysical properties PCMs investigated for different application.

Compound	Melting point (ºC)	Latent heat (J/g)	Heat capacity (J/g·K)	Thermal conductivity (W/m·K)	Density (g/cm^3)	References
H_2O	0	335	4.2	2.4	1000	67, 70
n-Octadecane	27.7	243.5	2.66(L)/2.14(S)	1.15(L)/1.19(S)	0.79(L)/0.86(S)	71-72
$CaCl_2 \cdot 6H_2O$	29.9	187	2.2(L)/1.4(S)	0.53(L)/1.09(S)	1.53(L)/1.71(S)	67, 73
Paraffin wax	32.1	251	1.92(L)/3.26(S)	0.224(L)/0.514(S)	0.83	74
Capric acid	32.0	152.7	-	0.153(L)	0.88(L)/1.00(S)	75
Polyethylene glycol 900 (PEG)	34.0	150.5	2.26	0.188	1.1(L)/1.2(S)	76
Lauric acid	41-43	211.6	2.27(L)/1.76(S)	1.6	0.86(L)/1.76(S)	77
Stearic acid	41-43	211.6	2.27(L)/1.76(S)	1.6	0.86(L)/1.00(S)	78
$Ba(OH)_2 \cdot 8H_2O$	48.0	265.7	-	0.653(L)	1.94(L)	
Paraffin wax	40-53	251	1.92(L)/3.26(S)	0.224(L)/0.514(S)	0.83	79
Commercial paraffin wax	52.2	243.5		0.15	0.77(L)/0.81(S)	80
$Mg(NO_3)_2 \cdot 6H_2O$	89.0	162.8	-	0.49(L)/0.61(S)	1.45(L)/1.63(S)	81
$MgCl_2 \cdot 6H_2O$	116.7	168.6	2.61(L)/2.25(S)	0.57(L)/0.70(S)	1.45(L)/1.57(S)	82
Indium	157.5	28.52	0.23	81.8	7.02(L)/7.31(S)	83
$NaNO_3/KNO_3$	220.0	100.7	1.35	0.56	1.92	84-86
Tin	231.9	59.2	0.23	66.8	6.99(L)	-
$ZnCl_2/KCl$	235.0	198.0	-	0.8	2.48	84-86
Bismuth	271.5	54.07	0.12	7.92	9.81(S)	-
$NaNO_3$	310.0	172.0	1.82	0.5	2.26	84-86
KNO_3	330.0	266.0	1.22	0.5	2.11	84-86
NaOH	318.0	165.0	2.08	0.92	2.10	84-86
KOH	380.0	149.7	1.47	0.5	2.04	84-86
$ZnCl_2$	292.0	75.0	0.74	0.5	2.91	84-86
$LiF-CaF_2$	767.0	816.0	1.77	1.70(L)/3.8(S)	2.39	84, 87

Extensive efforts have been made to apply the latent heat storage method to solar energy systems. For example, a new method for satellite power testing using PCMs has been put forwarded by Revankar.[68] PCMs used in solar power system are series of metal cells that is liquid under high temperatures, the released heat when experiencing cold darkness can then used to generate electricity by thermoelectric device. The system can generate at least three times more power than batteries of comparable size, which can be taken as a possible alternative to conventional satellite solar power system that rely on batteries.

However, there are several important barriers that limited the use of latent heat storage: 1) most PCMs used for thermal storage usually have low thermal conductivity, and the low thermal conductivity requires the use of large surface. Therefore, heat transfer enhancement techniques are usually required for latent heat storage applications.[88] Various methods are proposed to enhance the heat transfer in a latent heat thermal store, i.e. metallic fillers, metal matrix structures, finned tubes and aluminum shavings were used to improve paraffin's thermal conductivity; 2) phase segregation and supercooling problems are also important issue. For example, even though high latent heat PCMs like salt hydrate has high storage density, however, it is hard to maintain and usually decreases with cycling, which is because most hydrated salts melt congruently with the formation of lower hydrated salt, making the process irreversible and leading to the continuous decline in their storage efficiency; 3) insufficient long term stability of the storage materials requires that some protection methods must be done to the corrosion between the PCMs and containers and degradation in their properties.

2.3.2 Phase change materials for heat transfer

Nanofluid have been studied a lot on increasing the thermal conductivity of the base fluid. This concept has been extended by using PCMs as nanoparticles, which goes well rather than simply increasing the thermal conductivity of a heat transfer fluid.[89] Some theoretical calculation has been done by Han, et al. that when the volume fraction of nano-PCM suspension is 8%, the enhancement on the specific heat during the working temperature can be 20%, but there are still many problems needed to be addressed as we discussed in the introduction part, for example, the super-cooling is result from many factors like size factors, nucleation processes, and it must be greatly reduced so as to put the nano-PCM suspensions into use; one the other hand, the high viscosity that brought about by the adding of PCM nanoparticles will also increasing the power of rotator.

2.3.3 Phase change materials for solid memory devices

Non-volatile solid state memories have fast random access memories have become very popular and widespread. They can be found in personal music players or digital cameras, and is replacing or supplemental hard drives in other electronics such as computers. This storage concept has been proved so successful so far that it is a big advancement in semiconductor technology. The most recent approach is utilizing phase change materials. The mechanism of phase change memory concept is shown in Figure 4. The information is stored in the high resistance state, and when a PCM in the high resistance amorphous state is heated above the glass transition temperature by applying an electrical pulse, the amorphous phase changed into stable crystalline state. To switch back to the amorphous state, the material is heated much higher above the melting temperature by a larger current pulse. Rapid cooling quenches it in the amorphous state. Since the two states have very distinct electrical resistances, the stored information can be read easily. A current pulse of high intensity and short duration (bottom) is used for amorphization, while a pulse of lower intensity but longer duration (top) crystallization.[90]

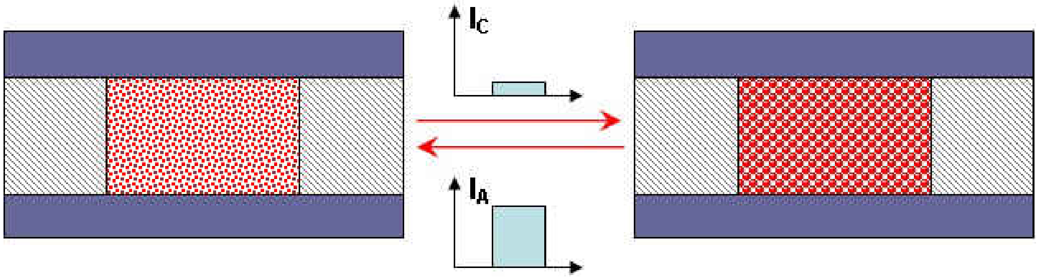

Figure 4. Electrical switching of PC materials for non-volatile electronic storage.

2.3.4 Phase change materials for bio-detection

The melting of crystalline nanoparticles absorb heat and generate sharp melting peaks on Differential Scanning Calorimetry (DSC), which are used as thermal signatures to determine the existence and concentration of DNA, proteins, or even cancer cells.[91-93] Multiple DNA and proteins can be detected by using different nanoparticles that melt at different temperature in order to create a one-to-one correspondence between one type of nanoparticle and one type of DNA, where each type of protein can only be captured by one probe DNA that connected to the corresponding detecting PCM nanoparticles (Figure 5). The amount of protein is determined by the enthalpy of fusion. The multiplicity is much high than other detection methods because of the narrow melting peaks and wide temperature range.

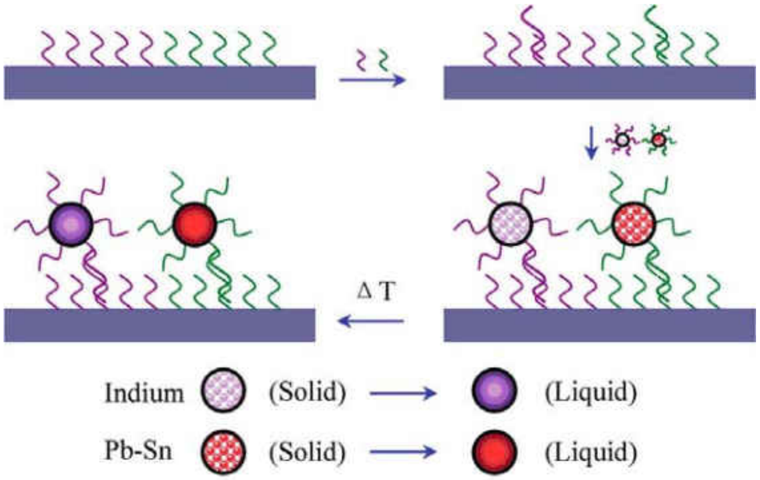

Figure 5. Scheme of detecting DNA biomarkers using phase change nanoparticles.

2.3.5 Phase change materials for thermal insulating

The PCMs have been used in buildings[94-96] and textiles[97]. The ability to store thermal energy is important for effective use of solar energy and internal energy in buildings. The low thermal mass of light-weight building materials tend to have high temperature fluctuations, which result in high heating and cooling demands. Using the thermal energy storage of PCM that has a melting point from 15 to 35ºC is one of the most effective ideas for effective utilization of this kind of materials in thermal insulating field. It is reported that more than 500 natural and synthetic PCMs are known.[98] Those PCMs differ from one another in their phase change temperatures and latent heat. Many PCMs like paraffin[99-101] and hydrated salt[102] have very large latent and are suitable for monitoring the temperature fluctuations.

Before applying PCMs to buildings or textile structure clothes, the PCMs should be encapsulated in very small spheres to contain them while in a liquid state. The shell should have several properties: 1) higher melting point than the PCMs in the cores; 2) robust enough to carry the PCMs when experienced mechanical actions, heat and some chemicals; 3) good thermal conductivities; 4) small super-cooling. There are two effects the PCMs can perform: cooling effect and heating effect. When the ambient temperature is higher than the phase change temperature of PCM, it melts to absorb heat, and when the temperature is lower than the phase change temperature, the PCM will freeze to release heat, which will somehow prohibit the temperature fluctuations.

2.4 Nanoparticles Synthesis and Encapsulation Technique

The sizes of PCMs play important roles in determining their melting behaviors. It has been shown that if the size of PCM is reduced by a factor of 10, the time required for complete melting will reduce by a factor of 100.[103] In order to fully exploit the latent heats of fusion, it is desired to have the PCM as small as possible so that it can melt instantaneously. On the other hand, the stability also depends on the particle size, if ignoring the interactions between particles, the smaller the nanoparticles, the more stable of the colloidal suspension. In many cases the PCM should be encapsulated to prevent leakage upon melting, which can lead to the agglomeration of PCMs and the temperature delay in the following melting cycle.[63] A non-melting ceramic or polymer shell can be made around small PCM to form encapsulated phase change particles.[104-106] Microencapsulated PCMs with diameter of 10-100 μm have been synthesized and dispersed in a liquid to adsorb heat energy, but such particles have large heat absorption delay because of large particle size, which can cause the decrease of heat removing efficiency in case of high power electronics. If could be synthesized, the nano-sized encapsulated PCM particles suspended in a liquid can melt in a much shorter time to enhance the heat capacity. A large variety of nanostructured crystals can be synthesized to improve the thermal transport properties of base fluids. Encapsulated nanoparticles made from metals, paraffin wax, fat, acid, salt hydrate, etc. can be synthesized and dispersed into heat transfer fluids, such as water, poly-alpha-olefin, ethylene glycol, hydrocarbons and fluorocarbons with or without surfactant to stabilize the suspensions.

2.4.1 Metallic nanoparticles synthesis and encapsulation

2.4.1.1 Synthesis

So far, nanoparticles can be synthesized from either chemical or physical methods. The last decade has witnessed the successful synthesis of metal nanocrystals in a variety of shapes through the chemical methods, which have many options on controlling the shapes obtained crystals, which include sphere, cube, and octahedron, etc. The chemical synthesis methods are involved composition changes that induced by heating, reducing or light catalysis, which includes sol-gel,[107-109] thermal decomposition,[110-116] chemical reduction[117-125] and photo-induced reactions.[126-127] Physical methods include direct sizes reduction, such as cryomilling,[128-132] emulsion,[133-138] or vapor phase condensation like thermal evaporation,[139-142] laser ablation,[143-144] sputtering[145-148] and electron beam lithography.[149-154] Those methods only introduce shape and size changes from the raw materials. The list of chemical and physical methods is shown in Table 4.

Table 4. Metallic nanoparticles synthesis protocols

Chemical	**Physical**
Sol-gel	Emulsion
Thermal decomposition	Cryomilling
Chemical reduction	Laser ablation
Light reduction	Lithography
Chemical vapor deposition	Sputtering
… …	… …

Chemical methods have good control on the shapes, chemical and catalytic properties by controlling the nucleation process. The sol-gel, chemical vapor deposition and electron chemical deposition methods are usually used for prepare thin layer on a flat substrate; light reduced reaction and thermal decomposition methods have good control over the sizes and monodispersity, but the high cost and low yield have limited their applications. Chemical reduction method like using sodium borohydride ($NaBH_4$) and other reductants have been used for the synthesis metallic nanoparticles, which is possibly the high yield method of nanoparticles synthesis. Physical methods also have fast developed in the last decades, the simple physical changes from bulk materials to nanoscale particles can produce high purity and well patterned nanopartricles, but some of them have very low yield like lithography (electron beam, printing, imprinting, and dip-pen lithography),[155-157] laser ablation and sputtering methods, while some other methods like cryomilling and emulsion methods have very high yield. Cryomilling, the mechanical attrition of powders within a cryogenic medium (approximately 77 K), is a method of strengthening materials through grain size refinement and the dispersion of fine nanoparticles. The technique was developed as a means to decrease both the size of these particles and their spacing by using a strong electromagnetic alloy bars to mill the raw materials into nanoscale powders at low temperature. Cryomilling method has a high yield but large size distributions and shape varieties, which is not appropriate for orienting nanoparticles synthesis strategy.

Miniemulsion method has been well developed since its discovery 30 years ago, which has been the subject of numerous investigations ranging from the fundamental to the applied. Initially, this method is used to synthesize polymer nanoparticles, however, in the last decade, researchers have begun to use this method for a novel method of synthesis low melting temperature metals and alloys such as indium, tin, bismuth, lead, cadmium, lead-bismuth, etc.[134, 137-138, 158] This solution-based approach that allows to process metals with melting points below 400ºC as monodispersed spherical colloids in large quantities, and with diameters controllable in the range of tens nanometers to micrometers. The solvents should have high boiling points and viscosities, which allow the metals or alloys to form uniform nanoscale liquid droplets under strong shear rate either through magnetic or mechanical stir, sometimes high power sonication is used to assist reducing the particle size and increasing the uniformity.[133, 159] The shear stress in a liquid is proportional to the viscosity and relative velocity gradient in the direction perpendicular to the layers. Most common liquid solvents are silicone oil, ethylene glycol, polyalphaoleffin, etc. On the other hand, surfactants like PVP, oleyamine, and some acid are added in the solvent to stabilize the nanoparticles. The simple and low cost miniemulsion technique has been one of the most favorable synthetic techniques.

2.4.1.2 Encapsulation of metal nanoparticles

Metal nanoparticles have many promising catalytic and biomedical applications since the end of last century. However, bare nanoparticles usually need to be encapsulated for better use of metal nanoparticles including rich surface chemistry, high biocompatibility, controllable porosity, and good optical properties. Many different core-shell structures i.e. metal/alloy in titania, carbon, silica, zirconia, cerium dioxide, polymers, and metals,[160] etc. have been found on published journals. The most common shell material is silica because of its unique physical, optical properties and diverse applications. The advanced high-quality synthesis of dense and porous silica encapsulated nanostructures are experiencing increasing research interest for catalytic, drug delivery, surface enhanced Raman scattering detection, photo-thermal therapy, colorimetric diagnostics and so on.

The research on monodispersed silica nanoparticles can be traced to year of 1968, where a sol-gel method of synthesis spherical silica nanoparticles in aqueous solutions of methanol, ethanol and isopropanol under various catalytic conditions was studied by Stöber.[161] This sol-gel method has been greatly used for encapsulation of metal nanoparticles since the last two decades.[162] The precursors of silica are mostly of tetraethyl orthosilicate (TEOS) and sodium silicate.[163-164] The surface of metal nanostructures usually modified with bifunctional molecules in order to increase the strength of silica attachment or controlling the thickness of silica shell. Examples include 3-aminopropyl-trimethoxysilane,[165] cetyltrimethyl ammonium bromide (CTAB),[166-167] etc. On the other hand, some acid or base catalysts care needed to accelerate the reaction speeds. Ammonia hydroxide is usually taken as the catalyst for condensation of TEOS, while dilute hydrofluoric acid is usually added into solutions for the hydrolysis of sodium silicate,[168] or a certain amount of ethanol is added into aqueous solution for silica to precipitate.[169] The obtained silica encapsulated nanoparticles need to be either dried at 90ºC in vacuum or heated above 110ºC to remove all the water.

Currently, the large-scale production and surface modification of various silica coated metal nanoparticles still remain a great challenge for practical commercialization though straightforward gram level synthesis of silica coated gold, silver, indium and platinum nanoparticles have been realized in lab. Multifunctional silica encapsulated optical devices, electronics and magnetic nanostructures are creating new opportunities for novel applications. With the wonderful application potential, titania and zirconia encapsulated metal nanoparticles are expected to receive more intensified research interest as alternatives of silica-encapsulated metal nanoparticles.

2.4.2 Synthesis of encapsulated polymer nanoparticles

Polymer nanoparticles and nano-capsules with different encapsulated materials are of great interest for a number of applications such as functional coatings, inks, adhesives as well as some pharmaceutical and biomedical applications. For the preparation of core-shell nanoparticles from radically polymerized monomers, the miniemulsion polymerization is method is often used.[170] Miniemulsions consist of well-dispersed, stable droplets that created from high shear forces applied either from ultrasound or mechanical stir, or even both. The size of the emulsions depends on the ultrasound power, stirring speeds, and amount of stabilizers. The stabilizer should show good solubility in the disperse phase, but at the meantime, it should also show a lower solubility in the continuous phase (the disperse phase is the solvent of phase change materials that will form small droplets in base solvent, where the base solvent is call continuous phase). Depends on solubility of the phase change materials and the disperse phase, miniemulsion method could be divided into two categories: oil-in-water and water-in-oil. In case of oil-in-water miniemulsion, the disperse phase should be hydrophobic, and in case of water-in-oil miniemulsion, it should be hydrophilic. After the droplets suspension was formed, each droplet will be a nanoscale reactor carrying different reactions i.e. crystallizations,[171] esterification,[172] sol-gel reactions[173] and polymerizations.[174] Among those processes, the radical polymerization miniemulsion method is the most popular technique. The polymerization process relies on diffusion of monomers through either the disperse phase or continuous phase. Radical polymerization can be performed with many different vinylic monomers ranging from hydrophobic to hydrophilic. Examples of hydrophobic monomers include styrene, acrylate, metharylates, fluoroacrylates, etc. In case of hydrophobic polymerization, water was usually selected as the continuous phase. The miniemulsion method is excellently suitable for encapsulation a variety of different materials ranging from hydrophobic to hydrophilic, from solid to liquid, and from inorganic to organic.

The encapsulation of different compounds at different phases or different solubility with the monomers is slightly different. If the compounds are soluble in the dispersed monomer phase, the encapsulation procedure will be easy and straightforward, where the component will be dissolved into the monomer prior to the miniemulsification step. During the polymerization, the component is entrapped in the polymer particles. As effective diffusion is suppressed in miniemulsions, the concentration of the compound in the monomer is retained during the polymerization process. After polymerization, depending on the hydrophobicity change from monomer to polymer, the compound could be either trapped in the polymer or form a core shell structure, where the dispersed phase of the direct miniemulsion consists of an organic liquid which represents a solvent for monomer, but not a solvent for the polymer. By tuning the surface tension of the participating interface in the system, phase separation occurs in such a way that the non-solvent is engulfed by the growing polymeric shell, leading to complete encapsulation of the inside liquid. For example, when encapsulating hexadecane with poly(methyl methacrylate) (PMMA), the large differences in hydrophilicity lead to capsules independent of the use of surfactants.[175] In case of Polystyrene (PS), the copolymerization with hydrophilic monomers such as acrylic acid,[176] methacrylic acid (MAA),[177] or N-sopropylacrylamide (NIPAM),[178] which lead to the formation of large fraction of capsules. The size and shell thickness can be adjusted by changing the ratio of core and shell materials. Another possibility for the formation of nanocapsules is to direct the polymerization reaction to the interface of nanodroplets and the continuous phase.[176, 179] Besides the phase separation, interfacial polymerization, precipitation polymerization can be used for the capsulation of an aqueous core with polymer shell. After aqueous droplets are obtained through miniemulsification, the solvent is evaporated and the polymer precipitates onto the aqueous droplets, forming a core-shell structure.[180] In addition to the organic compounds, metal complexes, and solvent soluble components, the insoluble solid materials can also be encapsulated. However, since most of the inorganic materials have to be hydrophobized prior to encapsulation because of their hydrophilicity.

2.5 Materials Characterization Technique

2.5.1 Microstructure characterization

2.5.1.1 Scanning electron microscopy

Scanning Electron Microscope (SEM) is a microscope that uses electrons to form images, which was developed in the early 1930's.[181] It has become one of the most powerful methods for physical properties characterization. The large depth of field and higher resolution provides a variety of advantages over optical microscopes. A typical SEM contains a chamber, an electron gun, magnetic condenser lenses, two deflection coils, one stigmator, an objective lens, two apertures, a sample stage and multiple detectors. The structure of an SEM is shown in Figure 6. A beam of electrons is produced by the filament at the top of the microscope and follows a vertical path through electromagnetic fields and lenses, which focus the beam on the sample. Signals that can be produced by an SEM include secondary electrons, back-scattered electrons (BSE), characteristic X-rays, light (cathodoluminescence), specimen current and transmitted electrons, and different detectors convert them into signals that will be sent to a displaying screen, which produces the final image. The most common imaging mode collects low-energy (<50 eV) secondary electrons that are ejected from the k-orbit of the specimen atoms by inelastic scattering interactions with beam electrons. Due to their low energy, these electrons originate within a few nanometers from the sample surface. Back scattered electrons (BSE) are beam electrons that are emitted from the sample by elastic scattering. Because the intensity of the BSE signals are related to the atomic number (Z) of the specimen, the obtained images can provide information about the element distributions in the sample, but the specimen need to be very smooth on the surface.

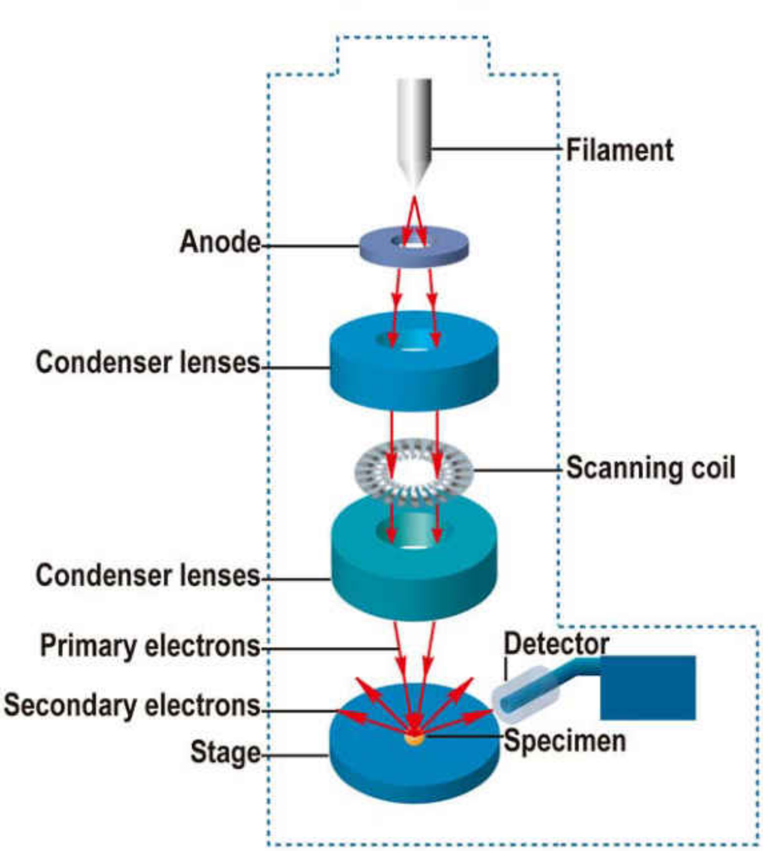

Figure 6. Schematic of scanning electron microscopy and the signal resources.

In order to obtain a good image in the SEM, the surface of specimen must be electrically conductive and grounded to prevent the accumulation of electrostatic charge at the surface. Nonconductive specimens usually coated with an ultrathin coating of electrically conductive material, commonly gold, deposited on the sample either by low vacuum sputter coating or by high vacuum evaporation to prevent being charged when scanned by the electron beam, and especially in secondary electron imaging mode, this causes scanning faults and other image artifacts. The sample is placed in a small chamber that is at a vacuum of about 10^{-4} Pa. Argon gas and an electric field causes an electron to be removed from the argon, making the argon atoms positively charged. The argon ions then become attracted to a negatively charged gold foil. The argon ions knock gold atoms from the surface of the gold foil. These gold atoms fall and settle onto the surface of the sample producing a thin gold coating.

By 2009, The world's highest SEM resolution at high beam energies (0.4 nm at 30 kV) is obtained with the Hitachi S-5500.[182] At low beam energies, the best resolution is achieved by the Magellan system from FEI Company (0.9 nm at 1 kV).[183] In this section, the phase change nanoparticles before and after the encapsulations are characterized by a Zeiss (Ultra 55) SEM operated at 10 keV to image the morphology. The samples for SEM observation are prepared by depositing small drops of indium nanoparticle in ethanol suspension on silicon substrates, and imaged with gold coating for 20 nm.

2.5.1.2 Transmission electron microscopy

Transmission electron microscopy (TEM) is a technique that an electron beam transmits through an ultra thin specimen and interacts with the specimen as it passes through where an image is obtained during the absorption of electrons and magnified onto an imaging device including fluorescent screens, photographic films, or CCD cameras. TEM is capable of imaging at a significantly higher resolution than optical microscopes due to the small de Broglie wavelength of electrons, which can be written as[184]

$$\lambda = \frac{h}{\sqrt{2meV}} \tag{2}$$

where *h* is the plank's constant (6.62×10^{-34} m^2/kg·s), *m* is the mass of electron (9.0×10^{-31} kg), *e* is the charge of electron (1.6×10^{-19} V), *V* is the excitation voltage. The most common TEMs are 100 kV and 200 kV, which have resolutions of 0.0037 and 0.00251 nm. If the excitation voltage is 1 MV, then the resolution could be 0.00087 nm, which is thousand times higher than the most powerful TEM so far.

A transmission electron microscope (TEM) includes many modes such as high-resolution TEM (HRTEM), selected area electron diffraction (SAED), X-ray diffraction analysis (XRD), high angle annular dark field (HAADF) STEM tomography, Energy-filtered TEM **(**EFTEM**)** and electron energy-loss spectroscopy (EELS) and energy dispersive X-ray analysis (EDX). Among those modes, the bright field imaging mode is the most common mode of operation for a TEM. The contrast formation is formed directly by occlusion and absorption of electrons in the sample. Crystal structure or lattice defects can also be investigated by HRTEM.[185]

In the SAED mode, the electron beam undergoes Bragg scattering, which in the case of a crystalline sample disperses electrons into the back focal plane. By placing apertures like objective aperture in the back focal plane, the desired Bragg reflections can be selected or excluded, thus only parts of the sample that are causing the electrons to scatter. If the reflections that are selected do not include the unscattered beam, then the image will appear dark wherever no sample scattering to the selected peak is present, as such a region without a specimen will appear dark. This is known as a dark-field image. The specimen can be tilt on the specimen holder to obtain specific diffraction conditions, and apertures above the specimen allow to select electrons that would otherwise be diffracted in a particular direction from entering the specimen.

By carefully selecting the orientation of the sample, it is possible not only to determine the position of defects but also to determine the type of defect. For the single crystal case the diffraction pattern depends on the orientation of the specimen and the structure of the sample. This obtained image provides information about the space group symmetries in the crystal and the orientation of crystal to the beam path.

EELS is an advanced technique of TEM, a magnetic spectrometer allows for the selection of particular energy values, which are associated with the way the electron interacts with the sample. EELS spectrometers can often be operated in both spectroscopic and imaging modes, allowing for either isolation or rejection of elastically scattered beams.

2.5.1.3 Atomic force microscopy

The atomic force microscopy (AFM), which depends on forces between the tip and the sample that lead to a deflection of cantilever according to Hooke's law, has been widely used to study the surface nanostructures and mechanical properties of materials, or produce arbitrarily ordered nanoscale patterns with high spatial resolution.[186-188] An AFM can be operated in contact mode, tapping mode, conductive mode, and liquid mode. This AFM contains a piezoelectric tube and a square four quadrant laser detector, an electrically driven sample stage with the capacity of analyzing 50 samples according to a pre-set program. The stage can move in two dimensions to align a desired sample. In addition, an inbuilt video system with ×400 magnification allows users to identify an interested area on the sample (Figure 7). For nano-education purpose, a teaching assistant has been assigned to place samples, install AFM tip and align laser, as well as monitor the access to AFM. Other than that, every operation can be carried out in remote mode.

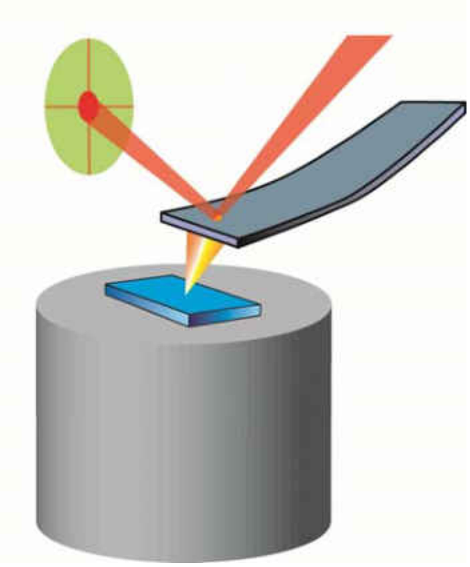

Figure 7. Structure of a typical AFM.

An important application of AFM is to derive the morphology, size, and roughness of a sample's surface. All imaging parameters such as scan rate, image resolution, imaging force, and integral gain values can be adjusted during imaging process. Some important operation functions such as zoom-in, zoom-out, and move-to-center can be carried out in real time. The data analysis such as 3D visualization, smoothing, cross section and distribution analyses can also be carried. AFM offers extremely high Z sensitivity, and is suitable for surface roughness measurement. AFM can also be controlled to operate in tapping mode, where the frequency change of a vibrating microcantilever is used to construct image. In order to operate in tapping mode, the resonant frequency has to be derived by monitoring the excited vibration of microcantilever. A few resonant peaks will appear at different frequencies, from which the resonant frequency is determined as the strongest peak. AFM can measure the mechanical properties of samples by applying defined forces onto samples and observing their deformation.[189-192] In the force distance curves, the repulsive force between an AFM tip and one sample is monitored when the tip is moved from far away to contact the sample. AFM can also be used to generate nanoscale features through nanolithography.

2.5.2 Determine the composition

2.5.2.1 Energy dispersive X-ray spectroscopy

Inorganic compound compositions usually determined by an analytical technique Energy-dispersive X-ray spectroscopy (EDX/EDS). It is one of the X-ray fluorescence spectroscopy which relies on the investigation of a sample through interactions between electromagnetic radiation and matter, analyzing X-rays emitted by the matter in response to being hit by electrons. Its capabilities are due to the fundamental principle that each element has a unique atomic structure allowing X-rays that are characteristic of an element's atomic structure to be identified uniquely from one another.[193] To stimulate the emission of characteristic X-rays from a specimen, a high-energy beam of electrons is focused on the sample. The atom within the sample contains unexcited state electrons in discrete energy levels. The incident beam excites an electron in an inner shell, ejecting it from the shell while creating a vacancy where the electron was. An electron from an outer, higher-energy shell then fills the hole, and the difference in energy between the high energy and the lower energy shells can be released in the form of an X-ray.[194] This allows the elemental composition of the specimen to be measured by an energy-dispersive spectrometer (Figure 8).

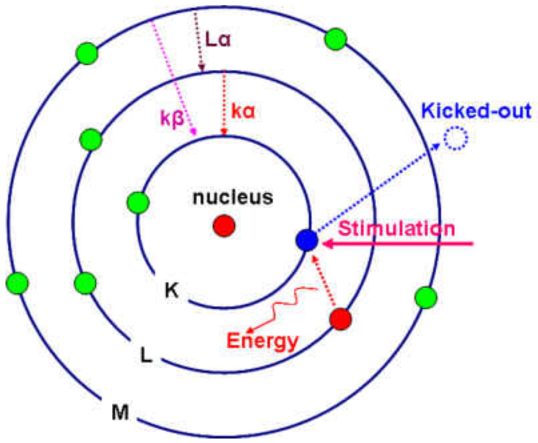

Figure 8. X-ray generation theory.

2.5.2.2 Fourier Transmission Infrared Spectroscopy

EDX is more suitable to investigate the composition of inorganic materials, while in order to study the organic like polymeric materials, there exists some other characterization technique i.e. Fourier transform infrared (FTIR) spectroscopy and nuclear magnetic resonance spectroscopy (NMR).[195] FTIR is a technique which is used to obtain an infrared spectrum of absorption, emission, photoconductivity or Raman scattering of a solid, liquid or gas. The key part of an FTIR is a Michelson interferometer. Light generated from the polychromatic infrared source is collimated and directed to a beam splitter and about 50% is transmitted towards the moving mirror. Light is reflected from the two mirrors back to the beam splitter and (ideally) 50% of the original light passes into the sample compartment. There, the light is focused on the sample. On leaving the sample compartment the light is refocused on to the detector. The difference in optical path length between the two arms to the interferometer is known as the retardation. An interference diagram is obtained by varying the retardation and recording the signal from the detector for various values of the retardation (Figure 9). An FTIR spectrometer simultaneously collects spectral data in a wide spectral range, which confers a significant advantage over a dispersive spectrometer that measures intensity over a narrow range of wavelengths at a time. The resulting spectrum represents the molecular absorption and transmission, creating a molecular fingerprint of the sample. Like a fingerprint no two unique molecular structures produce the same infrared spectrum. This makes infrared spectroscopy useful for several types of analysis: 1) identify unknown materials; 2) determine the quality or consistency of a sample; 3) determine the amount of components in a mixture. FTIR spectroscopy and microscopy have been mostly used in the mid-IR region of 4000-600 cm^{-1}.[196] Only a few research studies from the early 1970s report the use of far-infrared spectroscopy (600-50 cm^{-1}) on inorganic compounds.[197-198]

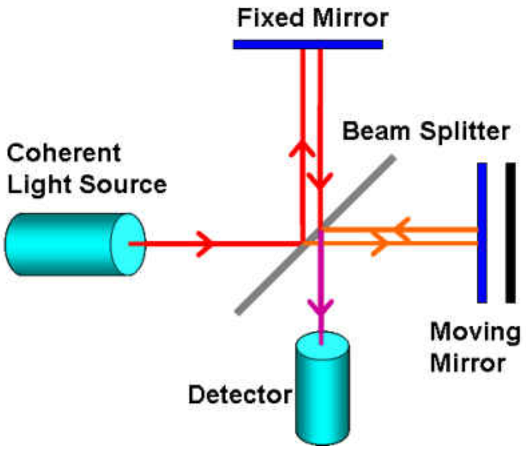

Figure 9. An interface diagram of Fourier transform infrared spectroscopy.

2.5.3 Latent heat and heat capacity measurement

Differential scanning calorimetry (DSC) is a thermal analytical technique to measure the phase change temperature as well as the heat capacity of the sample, where different amount of heat is required to increase the temperature of a sample and reference when heated and cooled linearly at the same rate, which was controlled by a temperature feed back program. The schematic mechanism of a heat compensation DSC is shown in Figure 10. The reference sample should have a known heat capacity over the range of temperatures to be scanned.

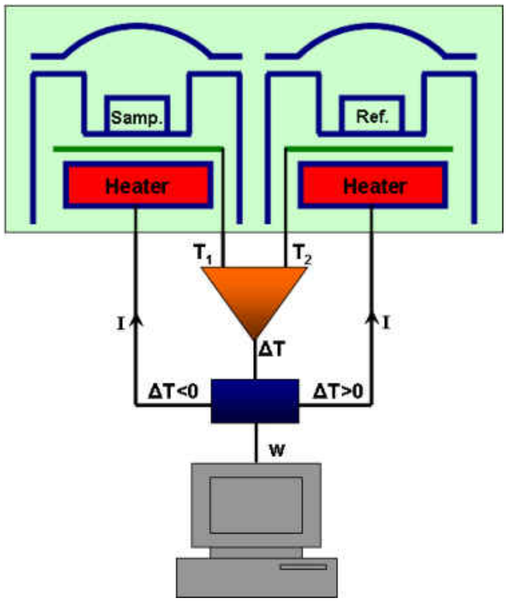

Figure 10. Schematic of heat compensation DSC machine.

The basic principle underlying DSC is that, when the sample undergoes a phase transition, more or less heat will need to flow to it than the reference to maintain them both at the same temperature. Whether more or less heat need to flow into the sample depends on whether the process is exothermic or endothermic. By observing the difference in heat flow between the sample and reference, DSC is able to measure the phase transition temperature, the amount of heat absorbed or released during such transitions. DSC may also be used to observe more subtle phase changes, such as glass transitions. It is widely used in industrial settings as a quality control instrument due to its applicability in evaluating sample purity and for studying polymer curing. An alternative technique, which shares much in common with DSC, is differential thermal analysis (DTA). In DTA it is the heat flow to the sample and reference that remains the same rather than the temperature. The temperature difference between sample and reference is recorded. Both DSC and DTA provide similar information. Many modern commercial DTA are usually called heat flux DSC. The result of a DSC experiment is a curve of heat flux versus temperature or versus time. There are two different conventions: exothermic reactions in the sample shown with a positive or negative peak, depending on the kind of technology used in the experiment. This curve can be used to calculate enthalpies of transitions by integrating the phase transition peak, which can be expressed using the following equation:

$$\Delta H = \frac{A}{m} \tag{3}$$

where *ΔH* is the enthalpy of transition, A is the area under the peak. The ability to determine transition temperatures and enthalpies makes DSC a valuable tool in producing phase diagrams for various chemical systems.

2.5.4 Structure determination

The crystallographic structure of nano-PCMs can be determined by either X-ray diffraction (XRD) or electron diffraction (ED). X-ray crystallography is a method of determining the arrangement of atoms within a crystal, in which a beam of X-rays interacts with a crystal and diffracts into many specific directions. Crystalline materials such as salts, metals, minerals, semiconductors, as well as various inorganic, organic and biological molecules can be characterized by X-ray crystallography. The method also revealed the structure and functioning of many biological molecules, including vitamins, drugs, proteins and nucleic acids such as DNA. Crystals are regular arrays of atoms, and X-rays can be considered waves of electromagnetic radiation. Atoms scatter X-ray waves, primarily through the atoms' electrons. An X-ray striking an electron produces secondary spherical waves emanating from the electron. This phenomenon is known as elastic scattering, and the electron is known as the scatterer. A regular array of scatterers produces a regular array of spherical waves. Although these waves cancel one another out in most directions through destructive interference, they add constructively in a few specific directions, which is determined by Bragg's law:

$$n\lambda = 2d\sin\theta \tag{4}$$

where d is the spacing between diffracting planes, θ is the incident angle, n is any integer, and λ is the wavelength of the beam. These spherical waves will be in sync only in directions where their path-length difference equals an integer multiple of the wavelength, producing a reflection spot in the diffraction pattern. X-rays are used to produce the diffraction pattern because their wavelength λ is typically the same order of magnitude (1-100 Ångströms) as the spacing d between planes in the crystal. To produce significant diffraction, the spacing between the scatterers and the wavelength of the impinging wave should be similar in size.

The reason for microstructure characterization is that the crystal structure during the phase transition process is very important for heat transfer parameter selection as well as studying the efficiency of the phase transformation. The known crystal structure also provides necessary information on selecting encapsulation technique in order to remove/reduce the supercooling of nano-PCM.

2.5.5 Size distribution of nanoparticles investigation

The size distribution of nanoparticles is measured using dynamics light scattering (DLS), also known as photon correlation spectroscopy or quasi-elastic light scattering, which can be used to determine the size distribution profile of small particles or polymers in liquid suspensions. When a beam of incident light hits small particles the light scatters in all directions (Rayleigh scattering) as long as the particles are smaller compared to the wavelength of the laser beam (below 250 nm). A monochromatic and coherent laser light source will result in a time-dependent fluctuation in the scattering intensity. These fluctuations are due to the fact that the small molecules in solutions are undergoing Brownian motion and so the distance between the scatterers in the solution is constantly changing with time. This scattered light then undergoes either constructive or destructive interference by the surrounding particles and within this intensity fluctuation, resulting in local inhomogeneities of the refractive index. This in turn results in fluctuations of intensity of the scattered light. The line width of the light scattered spectrum Γ (defined as the half-width at half-maximum) is proportional to the diffusion coefficient of the particles D:

$$\Gamma = Dq^2 \tag{5}$$

where the wave vector, $q = (4\pi n/\lambda)/\sin(\theta/2)$, n is the refractive index of the solvent, θ and λ are the scattering angle and the wavelength of the laser beam, respectively. The line width Γ can be obtained by fitting the original data of DLS measurement, then the diffusion coefficient D is calculated according to the above equation. Then mean diameter of the nanoparticles can be obtained by using Stokes-Einstein equation:

$$d = \frac{k_B T}{3\pi\mu D} \tag{6}$$

where K_B is Boltzmann's constant, T is the temperature, and μ is the shear viscosity of the solvent. Information about the light-scattering spectrum can be obtained from the autocorrelation function of the light-scattering intensity $G(\tau) = \varepsilon \cdot \exp(-\Gamma \cdot \tau)$, where ε is a constant, τ is the delay time.

2.5.6 Dielectric property measurement

Many cooling systems need high electrical insulating coolant. Therefore, it is very important the keep the property of dielectric coolant especially for direct immerse cooling. A dielectric is an electrical insulator that can be polarized by an applied electric field. When a dielectric is placed in an electric field, electric charges do not flow through the material as in a conductor, but only slightly shift from their average equilibrium positions causing dielectric polarization. Commercially manufactured capacitors typically use a solid dielectric material with high permittivity as the intervening medium between the stored positive and negative charges. This material is often referred to the "capacitor dielectric". The most obvious advantage to using such a dielectric material is that it allows a greater charge to be stored at a given voltage. For example, the capacitance of a parallel-plate capacitor constructed of two parallel plates both of area A separated by a distance d is approximately equal to the following:

$$C = \varepsilon_r \varepsilon_0 \frac{A}{d} \tag{7}$$

where C is the capacitance; A is the area of overlap of the two plates; ε_r is the relative dielectric constant of the material between the plates (for a vacuum, $\varepsilon_r = 1$); ε_0 is the delectric constant ($\varepsilon_0 \approx 8.854\times10^{-12}$ F·m^{-1}); and d is the separation between the plates. The relative dielectric constant of a liquid is obtained from ratios of capacitances of liquid coolant to that of air at different frequency (considering that the dielectric constant of air is equal to ε_0.

2.5.7 Viscosity measurement

In general, in any flow, the shear stress between layers that have different velocities arises from viscosity ultimately opposes any applied force. The relationship between the shear stress and the velocity gradient can be obtained by considering two plates closely spaced at a distance of y, and separated by a homogeneous substance. Assuming that the plates are very large, with a large area A, such that edge effects may be ignored, and that the lower plate is fixed, let a shear force τ be applied to the upper plate. If this force causes the substance between the plates to undergo shear flow at velocity u, the shear stress between layers is proportional to the velocity gradient in the direction perpendicular to the layers:

$$\tau = \mu \frac{\partial u}{\partial y} \tag{8}$$

The higher viscosity of a heat transfer fluid, the higher shear force is needed to flow the coolant through the channels according to the above equation. Therefore, viscosity is an important parameter that affects the performance of colloid suspension as coolant.

2.5.8 Molecular weight measurement of polymer

Gel permeation chromatography (GPC) was developed by J.C. Moore of the Dow

Chemical Company in 1964. GPC is often used to determine the relative molecular weight and distributions of polymer samples. When characterizing polymers, it is important to consider the poly-dispersity index (PDI) as well the molecular weight. Polymers can be characterized by a variety of definitions for molecular weight including the number average molecular weight (M_n), the weight average molecular weight (M_w) (see molar mass distribution), the size average molecular weight (M_z), or the viscosity molecular weight (M_v). GPC allows for the determination of PDI as well as M_v and based on other data, the M_n, M_w, and M_z can be determined. What GPC measures is actually the molecular volume and shape function as defined by the intrinsic viscosity. The data can be used to determine molecular weights within ± 5% accuracy. Polystyrene standards with PDI of less than 1.2 are usually used to calibrate the accuracy.

GPC is conducted in chromatography columns. Samples are dissolved in an appropriate solvent. The sample is injected onto a column after filtering the solution and let the multicomponents separate. Usually, multiple detectors are used to gain additional information about polymer samples.

2.6 Summary

This chapter summarized the importance of thermal management, current cooling technique, and heat transfer methods, current applications of phase change materials for thermal energy storage, heat transfer, bio-detection, solid-state storage, and thermal insulating. It also reviewed the metallic and polymeric core-shell nanoparticles synthesis strategies. Both chemical and physical methods can be used to synthesis nanoparticles depending on their chemical or physical properties and applications.

Nanoemusification method has been widely used as low-cost, high yield and green process by the strong shear forces between different solvent layers. This technique is suitable for both metal and polymer nanoparticles by choosing appropriate solvent, temperature and stirring rates, sometime sonication is used to assist forming liquid emulsions. The most popular method of metal encapsulation is Stöber method where TEOS is used as precursor to derive silica shell, while it also exist some other methods using the cheap water glass as precursor for deriving silica shell. In this study, both of the two methods are used to study the heat transfer properties of metal nanoparticles for high temperature cooling system. Oil-in-water miniemulsion method is used to prepare polymer phase change nanoparticles for studying low temperature heat transfer application.

It also reviewed materials characterization technique, including morphology study, structure analysis, composition determination, melting point measurement, dielectric property, viscosity and molecular weight measurement.

CHAPTER 3 SYNTHESIS AND CHARACTERIZATION

3.1 Introduction

The thermal property of solid nanoparticles has exhibited a variety of applications especially on thermal energy storage and heat transfer. Solid materials exhibit rich composition dependent solid-liquid and solid-solid phase transitions at certain temperatures. During phase transition, solids absorb heat without temperature rise according to Gibbs phase rule. If the dimension of solid is small enough that transition time can be negligible, a sharp heat absorbing peak appear during a linear thermal scan, where absorbed heat is compensated by adding extra energy to maintain constant temperature rise. Compared with other solids (organic materials, ceramics and salts), metal and alloy have large volumetric latent heat of fusion, and can be designed according to established phase diagrams, or computational thermodynamic software. The use of phase change nanoparticles could enable heat capacity enhancement and heat transfer ability by using their phase change behaviors. However, different heat resource requires different heat remove ability. Even though there are over a hundred elements on the earth, few of them can be used for energy storage and heat transfer applications, because most of the electronic devices work below 200ºC, and only a small number of metals in the periodic table can be used to produce nanoparticles due to availability and safety issues, however, many compounds, hydrate salts, polymers have relevant low melting points and have widely used. But there still little researches done on nanoscale phase change nanoparticles synthesis.

In this chapter, we will discuss the thermodynamic design and colloidal synthesis of metallic phase change nanoparticles (metals and alloys), encapsulation technique, and their typical thermophysical properties including phase change behavior, in-situ melting, and crystallography. The melting point of nano-PCMs can be monitored by design an appropriate composition using thermodynamics rules. For a given number of metals that can form binary eutectic alloys among any two of them, the numbers of binary alloy, ternary alloy and so on can be derived graphically from the Pascal's triangle. The total number of pure metals and eutectic alloys will be

$$\sum_{i=1}^{n} C_n^i = 2^n - 1 \tag{9}$$

where n is the total number of metals, and i is the number of metals in one nanoparticle. We have identified 10 different metals that can generate binary eutectic alloys among any two of them from the periodic table: aluminum, bismuth, cadmium, copper, gadillium, indium, lead, magnesium, palladium, and silver. Since each pair of metals form at least one binary eutectic alloy, these metals form 10 types of metal nanoparticles, 45 type of binary alloy nanoparticles, 120 types of ternary eutectic alloy nanoparticles, 210 types of quaternary eutectic alloy nanoparticles, and so on. The total number of metals and eutectic alloys is 1,023. On the other hand, solid-solid phase change also has endothermic or exothermic behavior when transformed from one phase to another.

3.2 Experiments

3.2.1 Synthesis of bare metallic nanoparticles

The synthesis method can be classified in three categories: chemical reduction, thermal decomposition, and nanoemulsion. For single component system, all of the above methods can be used for phase change nanoparticles synthesis. For high components system, the precursors of different components may not be able to decompose and form nanocrystals simultaneously and uniformly even at very high ambient temperature or not able to being reduced at the same time due to different electromotive force (EMF) of metals. The phase separation may lead to physical property change of the obtained nanoparticles. Therefore, thermal decomposition method or chemical reaction methods may have a limitation on the high component alloy nanoparticles synthesis. Nanoemulsion methods is a physical synthesis method that used for making nanoparticles, the alloys are mixed with high viscous solvent and heated above the melting point of the alloys, nanoparticles will be obtained under the vigorous stir.

3.2.1.1 Thermal decomposition method

This method can be applied for synthesis of both metallic and semiconductor nanoparticles, where an organometallic precursor is decomposed to generate metal atoms that nucleate and grow into monodispersed colloids. Bismuth is taken as a typical example to demonstrate this concept. Bismuth acetate is dispersed into ethylene glycol solution at ~200ºC under a nitrogen atmosphere with a magnetic stirring rate of 800 rpm. Polyvinylpyrrolidone (PVP 55000) was used as protective agents to stabilize the nanoparticles form aggregating. Typically, the amount of bismuth acetate varies from 0.25 to 1 mmol, which was added into 20 mL ethylene glycol together with 0.2 g PVP under the protection of nitrogen. After heating for 20 minutes at this temperature, the solution is quenched into a 0ºC ethanol (200 ml) under the protection of nitrogen.

This method can also be applied to high component nanoparticles, such as lead-bismuth, lead-tin-bismuth alloy. Typically, one precursor or mixtures of precursors at stoichiometric ratios are dissolved in ethylene glycol and stirred to form homogenous mixture, into which PVP is added as protective agent. For example, in order to make an alloy of Pb and Bi at 1:1 molar ratio, 0.75 mmol bismuth acetate and 0.75 mmol lead acetate are added into 20 ml ethylene glycol with 0.2 g PVP. The temperature of the mixture is increased to 200°C while stirring to decompose precursors in dry nitrogen. After reacting for 20 minutes, the reaction is quenched by pouring the hot mixture into 200 ml ethanol that is pre-cooled to 0°C. The nanoparticles are then separated by centrifuging at 4000 rpm for 10 min, and washing with ethanol (90%). Such washing and centrifuging processes are repeated for three times. $SnPb_{42}Bi_8$ nanoparticle as a typical composition was obtained by thermal decomposition of their acetate or acetylacetonate precursors in octyl ether solution under a nitrogen atmosphere. Octanoic acid and Bis-2-ethylhexylamine were used as the protective agents to prevent the nanoparticles form aggregating. Typically, 0.150 g of $Sn(acac)_4$, 0.015 g of $Bi(acac)_3$, 0.090 g of $Pb(acac)_4$, 0.144 g Octanoic acid (0.100mmol) and 0.242 g of Bis-2-ethylhexylamine (0.100mmol) were dissolved in 5.00 mL of octyl ether and refluxed under a nitrogen atmosphere for 10 min~1 h, the solution will turn into a dark brown color upon the formation of Sn-Pb-Bi alloy nanoparticles. Then 20 mL of ethanol was added to precipitate the nanoparticles. The amount of the reactants, the amount of protective agents, and the reaction time were systematically changed in the experiment to gain control over the sizes of the alloy nanoparticles. However, the initial molar ratio of $Sn(acac)_4$, $Bi(acac)_3$ and $Pb(acac)_4$ was fixed to 50:42:8, and the volume of octyl ether was fixed to 5 mL in all our experiments.

3.2.1.2 Chemical reduction method

In case of chemical reduction method, the precursors can be the organometallic acetylacetonate salts of appropriate metals, such as bismuth acetate, lead acetate, tin acetate, and lead acetate (obtained from Aldrich at chemical grade and used without purifications) or chloride salts of the corresponding metals like silver chloride, tin chloride, indium chloride, bismuth chloride, etc. The standard electromotive potentials of selected reactions are shown in Table 5.[199-201] The more negative of the electromotive force, it is more difficult to reduce the ions. Based on a thermodynamics augment from the perspective of EMF theory, readily available reducing hydrides such as lithium aluminum hydride ($LiAlH_4$), lithrium borohydide ($LiBH_4$) and $NaBH_4$ are commonly used and should be able to reduce most of metal precursors. For example, the EMF calculations for three theoretical electrochemical reactions are:[202]

$$3LiAlH_4 + In^{3+} \rightarrow In + 3Li^+ + 3AlH_3 + 1.5H_2 \qquad E^0 = +0.61 \text{ V}$$

$$3LiBH_4 + 9H_2O + In^{3+} \rightarrow In + 3Li^+ + 3B(OH)_3 + 10.5H_2 \qquad E^0 = +1.41 \text{ V}$$

For $NaBH_4$, the EMF is +1.64 V,[203] and from Table 4, the half reaction on indium reduction is -0.34 V, for H_2O it is -0.82 V, therefore, we can calculate the EMF for similar reaction using $NaBH_4$ as follows:

$$3NaBH_4 + 9H_2O + In^{3+} \rightarrow In + 3Na^+ + 3B(OH)_3 + 10.5H_2 \qquad E^0 = +0.83 \text{ V}$$

Therefore, it is quite easy to make the reduction happened. Further more, most of the metals we used for low melting point phase change nanoparticles applications have more positive EMF, therefore, it is feasible to reduce them using $NaBH_4$.

The synthesis procedure is simple and takes short time. Firstly, metal precursors are dissolved in proper solvents like water, diethylene glycol, methanol, isobutylamine or diethylenetriamine at stoichiometric ratios designed by the CALPHAD method. $NaBH_4$ is used as high chemical potential reductants to derive the alloy nanoparticles under the protection of suitable surfactant i.e. polyvinylpyrrolidone (PVP), oleylamine, and inert gas. The reactions usually takes 10 to 30 minutes to finish when the solutions turns dark. The obtained nanoparticles are washed by ethanol for several times and sealed under the protection of argon.

Table 5. Standard electromotive force.

Half reaction	E^0(V)
$Li^+ + e^- \leftrightarrow Li(s)$	−3.0401
$Mg^{2+} + 2e^- \leftrightarrow Mg(s)$	−2.372
$Al^{3+} + 3e^- \leftrightarrow Al(s)$	−1.66
$Zn^{2+} + 2e^- \leftrightarrow Zn(g)$	−0.7628
$Zn^{2+} + 2e^- \leftrightarrow Zn(s)$	−0.7618
$Cd^{2+} + 2e^- \leftrightarrow Cd(s)$	−0.40
$In^{3+} + 3e^- \leftrightarrow In(s)$	−0.34
$Sn^{2+} + 2e^- \leftrightarrow Sn(s)$	−0.13
$Pb^{2+} + 2e^- \leftrightarrow Pb(s)$	−0.13
$2H^+ + 2e^- \leftrightarrow H_2(g)$	**0.0000**
$Sn^{4+} + 2e^- \leftrightarrow Sn^{2+}$	+0.15
$Cu^{2+} + e^- \leftrightarrow Cu^+$	+0.159
$Bi^{3+} + 3e^- \leftrightarrow Bi(s)$	+0.308
$Cu^{2+} + 2e^- \leftrightarrow Cu(s)$	+0.340
$Cu^+ + e^- \leftrightarrow Cu(s)$	+0.520
$Ag^+ + e^- \leftrightarrow Ag(s)$	+0.7996
$Pd^{2+} + 2e^- \leftrightarrow Pd(s)$	+0.915
$Au^{3+} + 3e^- \leftrightarrow Au(s)$	+1.52
$Pb^{4+} + 2e^- \leftrightarrow Pb^{2+}$	+1.69
$Au^+ + e^- \leftrightarrow Au(s)$	+1.83

3.2.1.3 Nanoemulsion method

Nanoemulsion method is a physical method of synthesis nanoparticles by heating the bulk metal alloys above their melting points under strong shear force and the protection of surfactants. Most of the low melting point alloys nanoparticles can be obtained by selecting appropriate solvent, temperature, stirring rate/sonication power and surfactant. In the case of indium that has a melting point of 156°C, emulsification is carried out by boiling certain amount of indium powder (-325 mesh) in poly-α-olefin (PAO) or silicone oil at 200°C for 12 hours with magnetic stirring under the protection of nitrogen gas, sonication can be used to assist the uniformity of obtained nanoparticles. The diameters of indium nanoparticles obtained from nanoemulsification method depend on boiling time and size of starting materials (powder), and decrease from 165 to 85 nm as time increases from 2 to 48 hrs (Figure 11). The relationship between nanoparticle size and reaction time can be fitted to Taylor's formula:[204]

$$r_p = W_e \cdot \sigma / (\mu_c \cdot \gamma) \tag{10}$$

where r_p is the nanoparticle radius, W_e is Weber number, σ is the interfacial tension between nanoparticles and PAO, γ is the shear rate, and μ_c is the viscosity of PAO.

Nanoemulsion method can also be used to synthesis alloy nanoparticles, the eutectic alloys like $Sn_{63}Pb_{37}$, $Bi_{54}In_{28}Sn_{17}$, and $Bi_{50}In_{19}Sn_{11}Pb_{20}$ are sintered first at stoichiometric ratios above the eutectic points in vacuum. The as made alloys are dispersed into the high viscous oil like PAO or silicone oil. The bulk alloy can be broken into nanoparticles for a certain period.

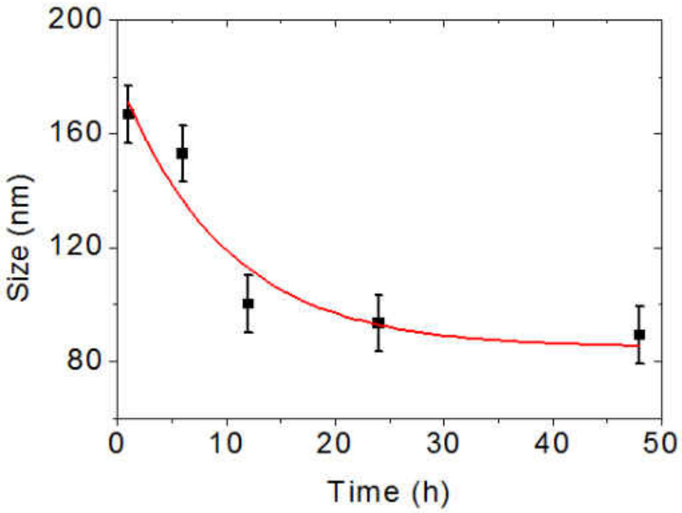

Figure 11. Boiling time dependent nanoparticle diameter.

3.2.2 Encapsulation of metallic nanoparticles

The precursor used to encapsulate PCM nanoparticles is tetraethoxysilane (TEOS) obtained from Aldrich. Sol-gel method is used to form thin silica shell around PCM nanoparticles. After re-suspending 50 mg nanoparticles into 50 ml of ethanol, 2 ml of NH_4OH at the concentration of 28%, and 0.2 ml of TEOS are added drop-wisely into the solution. The mixture is then sonicated at 70°C for 1.5 hours to decompose TEOS and make silica shells around nanoparticles. After reaction is complete, the mixture is centrifuged to remove the top clear water and washed by ethanol. The washing and centrifuging process are repeated for three times to ensure the complete removal of residual TEOS. The thickness of silica shell can be controlled from 10 to 80 nm by changing the ratio of metal nanoparticles and the TEOS precursor.

3.2.3 Synthesis of polymer encapsulated wax nanoparticles

A one-pot oil-in-water method is used to make polystyrene encapsulated paraffin wax (28 or 56ºC) nanoparticles. 10.0 g of wax, 0.2 g of azobisisobutyronitrile and 1.2 g of oleylamine are dissolved in 10.0 g of styrene by sonication for 30 min. The mixture is poured into 100 ml water 0.5 g of Triton X-100 in a 250 ml three-neck flask. The mixture is sonicated for 30 minutes to form a stable emulsion. The flask is purged by nitrogen for 30 min, followed by heating at 70ºC for 6 hrs at 400 rpm to complete polymerization.

3.3 Results and Discussions

3.3.1 Metallic nanoparticles

Four basic elements (bismuth, indium, tin, lead) were selected and calculated using Pandat thermodynamic data base in order to design single component, binary, ternary, quaternary and quinary alloys. For single component system, when we are considering the solid-liquid and liquid-solid phase change, the phase equilibrium happened when the Gibbs free energies of solid and liquid are equal at equal temperature and vapor pressure. The energy it needs to melt depends on how much entropy is increased during the phase transition, or thermodynamically estimate by Clausius-Clapeyron equation: $dP/dT=\Delta H/T\Delta V$, where P is the vapor pressure, ΔH is the latent heat of fusion, T is melting point at one 1 atm, ΔV is volume change during the solid to liquid transformation. Usually, materials will stay at a single unless the surrounding environment has been changed i.e. temperature, or pressure. By choose a suitable T and P, solid, liquid and vapor can coexist at the same time. Figure 12A shows a typical phase diagram of single component material. Most of metals are solid at room temperature and 1 atm. Bismuth is used as an example of single component phase change materials. The Gibbs free energy of solid and liquid bismuth equals at 271.5ºC at 1 atm, where solid phase begins to transform to liquid phase at this temperature and will not increase until all of the solid disappears. Its nanoparticles are synthesized from thermal decomposition method. Figure 12B is a TEM image of bismuth nanoparticles which have an average diameter of 200 nm. DSC curves in Figure 12C shows that the melting peak of as synthesized bismuth nanoparticles is about 270ºC, and the freezing peak is at 160ºC. The large supercooling is due to the homogeneous nucleation of bismuth nanoparticles. The melting point is similar as the theoretical value.

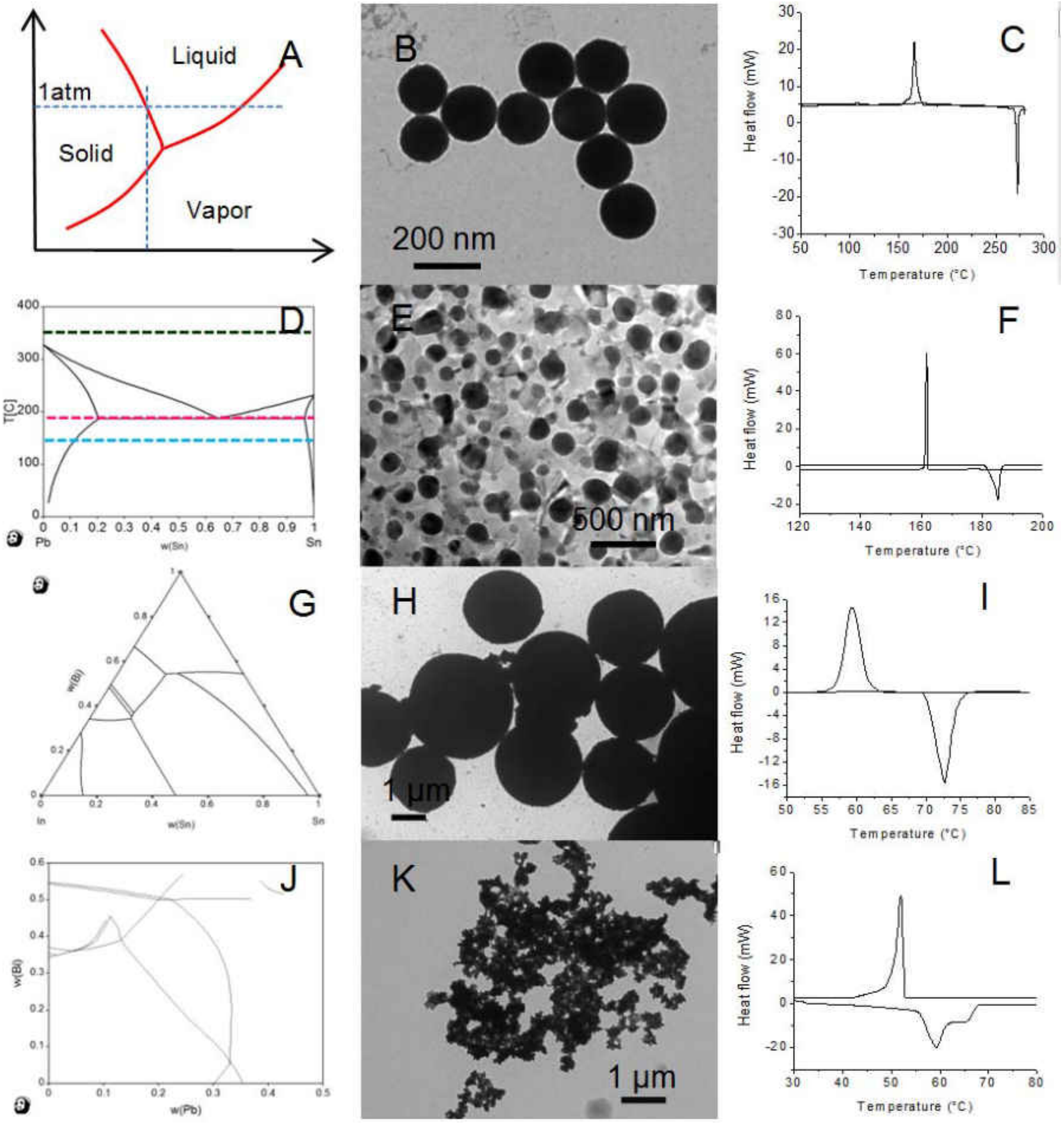

Figure 12. Phase diagrams, TEM images, DSC curves of Bi, Sn-Pb, Sn-Bi-In, Sn-Pb-Bi-In, respectively (from top to down).

Calculation of phase diagram method (CALPHAD) enables the extrapolation of multi-component phase diagram, which is used to derive the compositions of binary, ternary and other high order eutectic alloys. The calculations performed are based on models for the Gibbs energy function of every phase in the system. The Gibbs energy at thermodynamic equilibrium is minimum for a given temperature, pressure and composition, when the phases are in equilibrium. Gibbs derived the well known equilibrium condition that the chemical potential μ_n^{φ} of each component *n* is the same in all phases *φ*. The chemical potentials are related to the Gibbs energy by the well known equation:

$$G = \sum_{i=1}^{n} \mu_i x_i \tag{11}$$

The description of the Gibbs energy of a system requires assignment of thermodynamic functions for each phase at an equilibrium state to minimize the Gibbs energy. The temperature dependence of the Gibbs energy of a pure substance is usually expressed as power series of *T*

$$G^{\varphi} = a + bT + cT\ln(T) + dT^2 + eT^3 + fT^{-1} + gT^7 + hT^{-9} \tag{12}$$

where the values of the parameters *a*,…, *h* are taken from the SGTE compilation by Dinsdale.

The driving force of a phase change is defined as the negative of smallest value of the difference between the Gibbs energy of a phase and the equilibrium tangent plane at the same composition. For a binary phase diagram, the stable phases of the two components will coexist at a minimum energy level, where a tangent line of all minimum Gibbs energy curves. Whenever two components were selected, the software will use the database to calculate the Gibbs free energy of all possible phases at different temperature and composition at 1 atm. The phase transition of Sn-Pb alloy is drawn as boundaries of the phases, which shown in Figure 12D. The Gibbs free energies of possible phases of liquid, face-centered-cubic (FCC) and body-centered-cubic (BCC) at 150, 183 and 350ºC are calculated using the software. At 150ºC, the stable phases are for the FCC and BCT, the liquid phase will not exist at this temperature; while at 183ºC, a tangent line connects the minimum of three phases, which indicates a eutectic isothermal; at 350ºC, the only stable phases is liquid. A eutectic binary alloy behaves as a pure elemental, where the melting or solidification occurs congruently at eutectic phase transformation temperature. A congruent solidification is characterized by isothermal freezing of a liquid to form a solid of the same composition. In contrast, if the alloy is at a non-eutectic composition, the phase transformation process is incongruent. During the congruent melting, the solid and liquid phases coexist at a constant temperature, while during the incongruent phase transformation process solid and liquid of different composition coexist over a range of temperatures, which is very important for thermal barcode system. For one thing, the system needs the melting signals obtained from DSC machine, the more numbers of phase change materials, the more objects can be labeled. However, the temperature scanning range limitation of DSC requires the melting peaks as narrow as possible, and the non-eutectic composition with incongruent melting behavior is definitely not preferable for thermal barcodes system due to the large melting range, wherein reduce the multiplicity when encoding. On the other hand, the limit number of binary eutectic combinations also limits the multiplicity. Nevertheless, ternary and high components eutectic alloys are in phase change manner analogous to that of binary alloys, complicated only by the possible appearance of an additional solid phase upon cooling. Figure 12E is the TEM image of tin-lead nanoparticles obtained from nanoemulsion method, and the average size is about 150 nm. DSC curve in Figure 12F shows that tin-lead nanoparticles melt at 185ºC and freezes at 161ºC. The melting point is close to the calculated value of 183ºC.

Ternary and quinary alloys are also designed according to the thermodynamics rules similar as binary alloys. $Bi_{54}In_{28}Sn_{17}$, and $Bi_{50}In_{19}Sn_{11}Pb_{20}$ have been synthesized through nanoemulsion method, Figure 12G shows the liquid projection of $Bi_{54}In_{28}Sn_{17}$ alloy, the liquidus lines meet at two eutectic compositions, TEM image in Figure 12H shows that the average diameter of obtained ternary nanoparticles is ~3 μm, DSC curve in Figure 12I confirms the theoretical phase transition temperature is about 72.5ºC. Figure 12J, 12K, 12L show the liquid projection, TEM image and DSC curve of $Bi_{50}In_{19}Sn_{11}Pb_{20}$ alloy nanoparticles, the melting point is also same as designed value.

We take bismuth nanoparticles obtained from thermal decomposition method as an example to study the encapsulation result. The formation of silica shell does not change the shape of nanoparticle cores at low temperature. Figure 13 shows the EDS elemental mapping results from the silica shell (composed of Si and O) and bismuth core, respectively, in corresponding to the TEM image given on the left. It is demonstrated that the produced silica-encapsulated bismuth nanoparticles are quite uniform in the shell thickness, core size and geometry, which are highly desirable for PCM nanoparticles to play thermal management roles with a consistent capability.

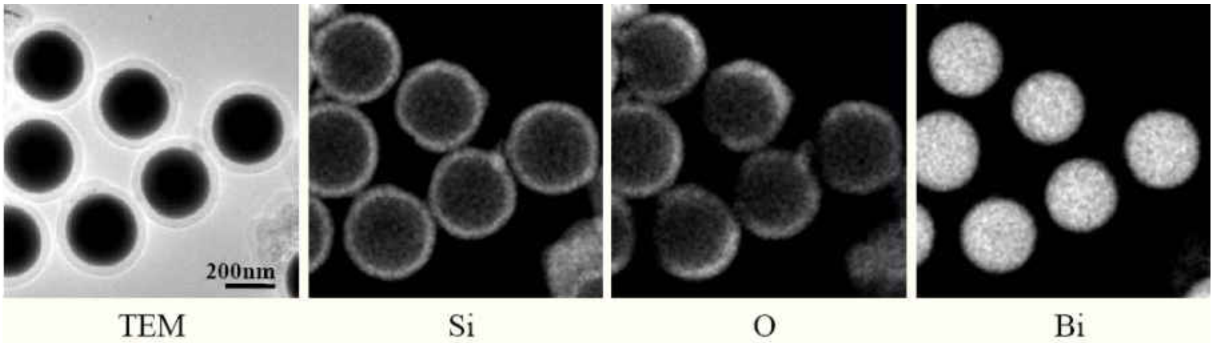

Figure 13. EDX element mapping of silica encapsulated bismuth nanoparticles.

EDX spectrum confirms the composition of encapsulated nanoparticles has bismuth and silica composition (Figure 14), where bismuth peak is generated due to the large interaction volume of high energy electrons.

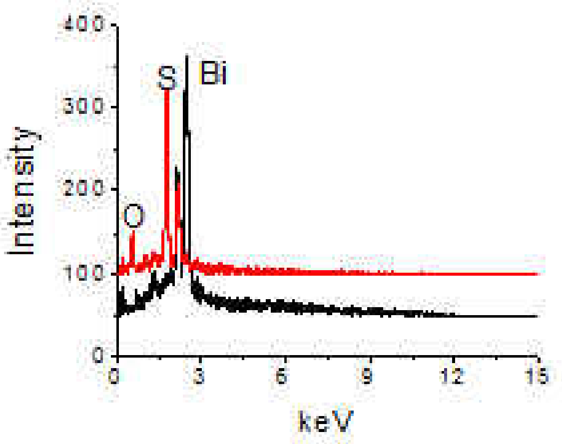

Figure 14. EDX spectrum confirms the composition of encapsulated nanoparticles has bismuth and silica composition.

High resolution TEM image shows the amorphous silica shell, and the crystalline structure of nanoparticles core (Figure 15). The hexagonal symmetric diffraction pattern indicates the rombohedral single crystalline nature.

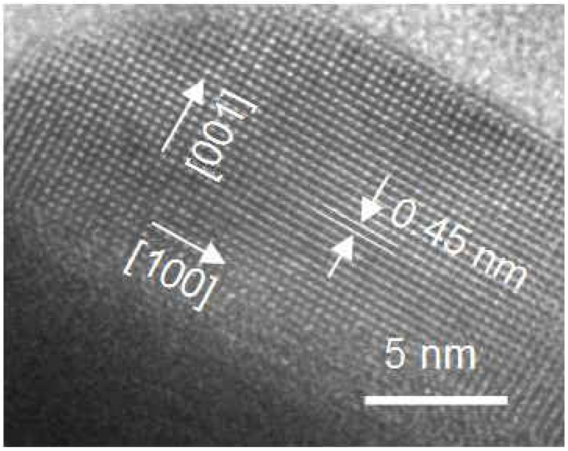

Figure 15. High resolution TEM image shows the amorphous silica shell, and the crystalline structure of nanoparticles core.

In the XRD pattern (Figure 16) all peaks can be indexed to a rhombohedra structure of bismuth structure with a of 0.455 nm and c of 1.186 nm (JCPDS No. 05-0519, $R\overline{3}m$). No obvious peaks at 10.5°, 28.5° and 56.3° that match the crystal planes of bismuth (100), (012), and (024) are found on the XRD pattern of encapsulated bismuth nanoparticles, meaning bismuth nanoparticles are protected by surfactant at high temperature. In comparison the oxidation peaks of Bi_2O_3 are observed from the XRD pattern of bismuth nanoparticles synthesized without silica shells.

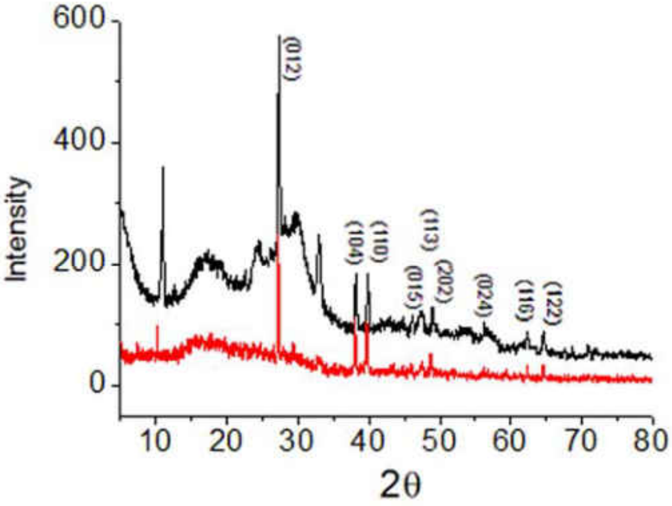

Figure 16. XRD spectra bare and encapsulated bismuth nanoparticles.

3.3.2 Polymer encapsulated wax nanoparticles

Polymer encapsulated wax nanoparticles are successfully synthesized by a one-step oil-in-water method, the wax can be covered a wide melting range from 10-90ºC. The average size of nanoparticles using this recipe is about 100-150 nm, which is shown in Figure 17 measured by DLS.

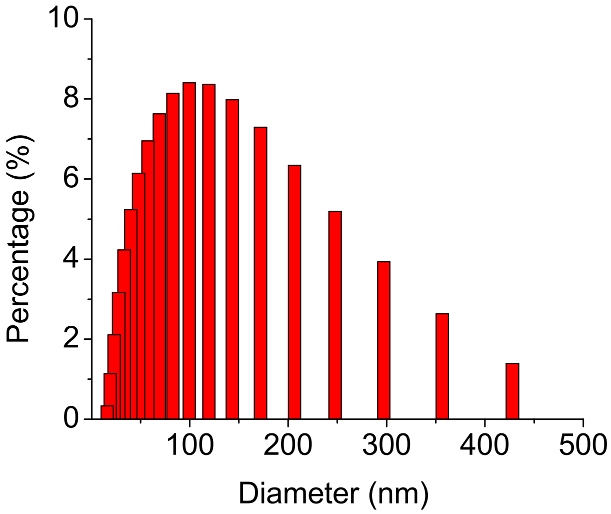

Figure 17. Size distribution of polymer encapsulated wax nanoparticles measured by DLS.

The encapsulated nanoparticles have good core-shell structure, which is shown in Figure 18. The low and high resolution TEM images show that the interfaces is clear between polymer and wax, the shell and the core are about 20 and 120 nm.

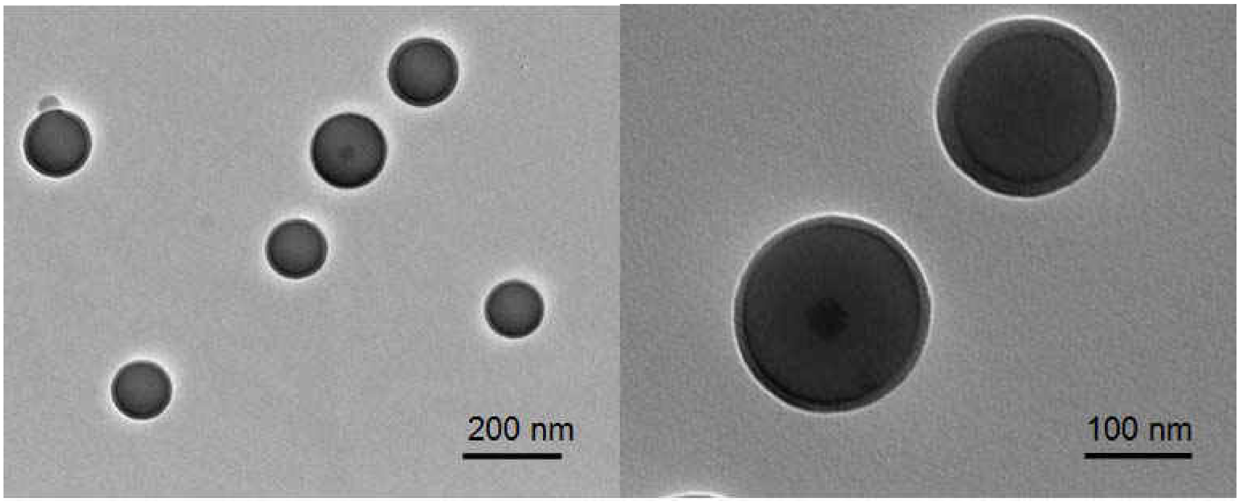

Figure 18. Low (left) and high (right) TEM images of polymer encapsulated wax.

The melting behavior is shown in Figure 19. The melting point is related to the heating speeds, the faster the heating speed, the higher the melting point as well as peak width. From Figure 19 we can find out that when the heating speed increases from 1 to 40ºC/min, the melting point increases from 46 to 54ºC, which is plotted in the right figure.

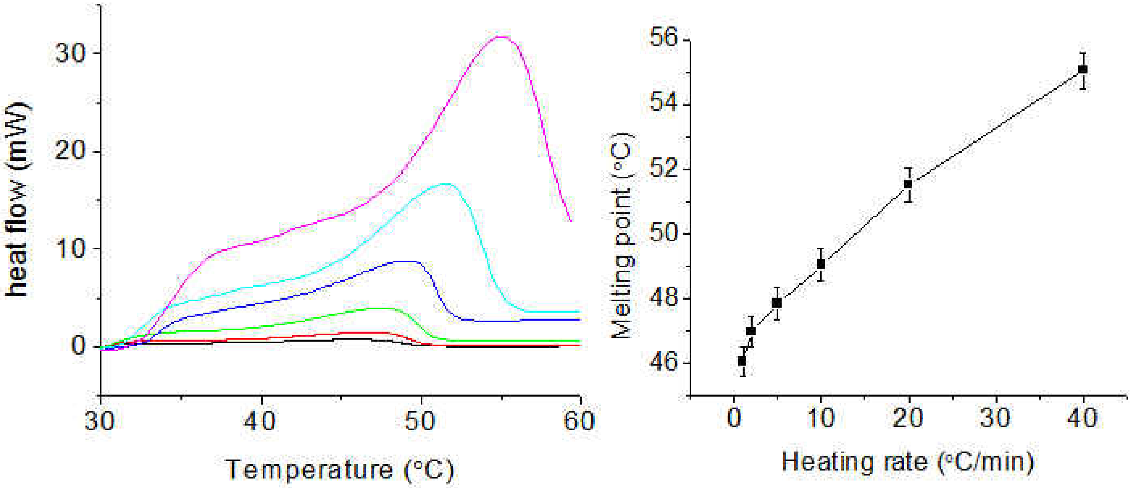

Figure 19. Melting temperature of polymer encapsulated wax at different heat rates.

3.4 Kinetics of Nucleation

Nucleation is the extremely localized budding of a distinct thermodynamic phase. Studying the nucleation process of nanoscale crystalline is very important for understanding nanoparticles synthesis technique. Nucleation can be classified as homogeneous and heterogeneous nucleation. Nucleation without preferential nucleation sites is homogeneous, which occurs spontaneously and randomly, but it requires a certain degree of supercooling which depends on the nucleation barrier. [205]

Nucleation occurs spontaneously if and only if the associated change in free energy for the system is negative. Likewise, a system reaches equilibrium when the associated change in free energy for the system is zero, and no spontaneous process will occur if the change in free energy is positive. The creation of a nucleus implies the formation of new interface at the boundaries of the new phase. Energy is required to form this interface, which is based on the surface energy of each phase. If a hypothetical nucleus is too small, the energy released by forming the volume is not enough to create the interface and nucleation can not proceed. As the phase transformation becomes more and more favorable, the formation of give volume of nucleus enough energy to form an increasingly large surface, allowing progressively smaller nuclei to grow. In classical nucleation theory, the free energy needed to form spherical nuclei is:[206]

$$\Delta G = -\frac{4}{3}\pi r^3 G_v + 4\pi r^2 \sigma \tag{13}$$

where G_v is the volume energy in J/cm^3, σ is surface energy. It costs free energy to add molecules to this cluster until reaches the critical radius $r^* = 2\sigma/G_v$. Addition of new molecules to the clusters that are larger than this critical radius is no longer limited by nucleation, but maybe by diffusion. The free energy needed to form this critical radius can be calculated by plugging the critical radius in equation 13, where $\Delta G^* = 16\pi\, \sigma^3/3G_v^2$, which occurs at the maximum ΔG where $dG/dr = 0$. The term G_v is related to the equilibrium temperature, enthalpy of fusion (ΔH_v), and the degree of supercooling (ΔT) as follows:

$$\Delta G^* = \frac{16\pi\sigma^3 T_m^2}{3\Delta H^2 \Delta T^2} \tag{14}$$

while for heterogeneous nucleation, the critical energy $\Delta G^*_{het} = \Delta G^* f(\theta)$, where $f(\theta)$ is related to the wettability of the liquid drops of the materials, where it is usually less than 1, which means the critical heterogeneous nucleation could be lower than homogeneous nucleation of the same liquid phase. The Gibbs free energy versus radius curves for heterogeneous nucleation and homogeneous nucleation is shown in Figure 20.

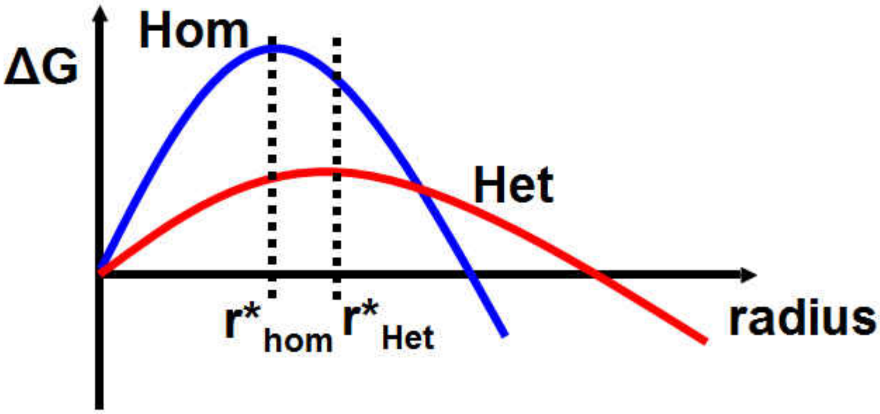

Figure 20. Nucleation energy versus radius.

The nucleation rate, *I*, depends on the average number of critical clusters, *n** and the diffusion of molecules to the cluster, *β*. $I = n^* \beta$,where the average population of critical nuclei is $n^* = N\exp(-\Delta G^* / k_B T)$, where ΔG^* is critical free energy, *N* is the number of potential nucleation sites per unit volume, k_B is the Boltzmann constant. The number of clusters of a certain size formed is as function of the total number of atoms in the system, free energy to create a cluster, and temperature. The number of clusters is proportional to the increasing of temperature. The rate of addition of one extra atom to the critical nucleus as estimated by the Volmer-Weber theory is $B = A\exp(-(Q + \Delta G^*) / k_B T)$, where *A* is related to the shape factor and the vibration frequency of the particles; *Q* is the activation energy for atom to migrate. This term gives us the diffusion of the atoms to the site of nucleation. However, a problem with the Volmer Weber theory is that it ignores formation of particles of $r > r^*$ and assumes that size distribution is maintained. The rate of nucleation is:

$$I(T) = A\exp(\frac{-Q}{kT})\exp(\frac{-16\pi\gamma_{sl}^{3}}{3\Delta H_{s}^{2}}\cdot\frac{1}{kT}\cdot\frac{T_{m}^{2}}{\Delta T^{2}}\cdot f(\theta)) \tag{15}$$

where γ is the surface energy, ΔH_s is the enthalpy, T_m is the melting point. θ is the contact angle. From this equation, at very low temperatures, diffusion rate is low, but as temperature increases, the rate increases. At temperatures significantly below melting temperature, fluctuation of molecules is very low and they are in a low energy state and do not have enough energy to move around and nucleate, where nucleation rate is dominated by diffusion. However, as temperature increases, molecular fluctuations increase and molecules can not stay in the nucleus, resulting in a decrease in rate of nucleation.

The bare and encapsulated bismuth nanoparticles show reversible phase changes between solid and liquid phases as the temperature increases or decreases. Figure 21A shows a DSC curve of 200 nm bismuth nanoparticles, where the melting and solidifying peaks are at 271.5 and 167.2ºC, respectively. The width at half peak height is about 2ºC, and the melting temperature of nanoparticles is close to the bulk melting value of bismuth (271.5 °C). The enthalpy of bismuth nanoparticles is calculated from the DSC measurement, where the peak area under endothermic peak is equal to the total heat absorbed by nanoparticles filled in the sample pan. The latent heats of nanoparticles are derived from

$$\Delta H_{m} = \frac{\Delta J\cdot\Delta T}{2mV_{T}} \tag{16}$$

where ΔH_m is the latent heat of nanoparticle material, ΔJ is the heat flux increase during melting, ΔT is the width of melting peak, m is the mass of nanoparticles, V_T is the temperature ramp rate. To do DSC measurement, 5 mg bismuth nanoparticles or silica encapsulated nanoparticles are heated at ramp rate of 2 °C/min. Assume the endothermic peak starts from 265°C and ends at 275°C, the heat flow between the lowest and temperatures is 24.5 mW, from which the latent heat of bismuth nanoparticles is derived as 30.63 J/g. The measured latent heat is lower than the published value of bulk bismuth (54.07 J/g). Such reduction in latent heat could be induced by the weakened bond of nanoparticles. In addition, the solidifying curve shows a large super-cooling, which is because of the homogeneous nucleation in the absence of nucleation sites, which is well captured by the classical nucleation theory. The freezing or liquid-to-solid transformation relies on homogeneous or heterogeneous nucleation. The melting temperature of the bismuth nanoparticles is found to be below the bulk value, indicating that $\gamma_{SM} > \gamma_{SL} + \gamma_{LM}$ (or $\gamma_{LM} < \gamma_{SM} + \gamma_{SL}$), where γ is the interfacial energy and the subscripts S, L, and M represent the solid phase, the liquid phase and the base matrix (Ethylene Glycol). In this situation, the liquid nanoparticles would not "pre-solidify" at the interfaces with the base liquid due to $\gamma_{LM} < \gamma_{SM} + \gamma_{SL}$. In other words, homogeneous nucleation would be the preferred type of nucleation mechanism for the bismuth nanoparticles. It is known that homogeneous nucleation has a greater nucleation barrier than heterogeneous nucleation, which significantly lowers the nanoparticles melting time. Therefore, the super-cooling might be mitigated by either pre-existed nucleus or reducing the temperature ramp rate in DSC. Figure 21B shows that the dependence of super-cooling on temperature ramp rate, where supper-cooling decreases from 100 to 90°C as the ramp rate decreases from 20 to 0.5 °C /min.

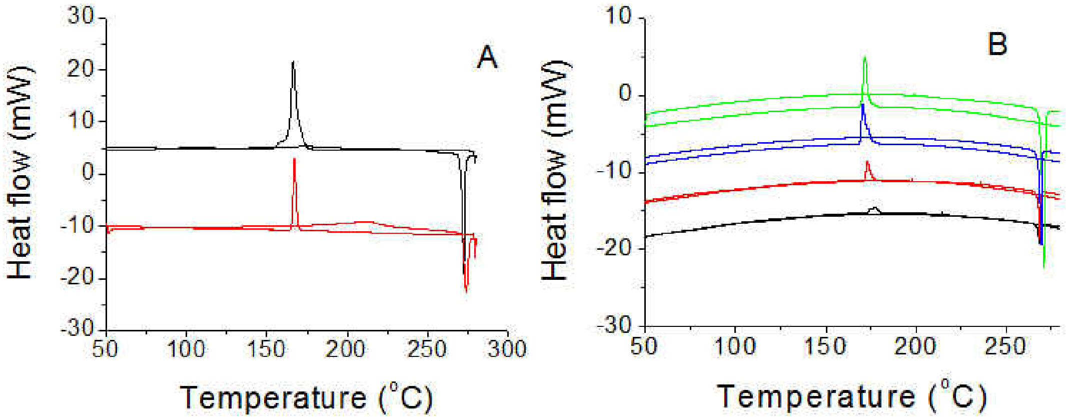

Figure 21. DSC curves of bare (top) and encapsulated (bottom) bismuth nanoparticles (A); dependence of supercooling on temperature ramp rates from 20 to 0.5°C /min (top to bottom) (B).

3.5 Summary

This chapter introduced a variety of synthetic techniques of nano-PCMs, which including thermal decomposition, chemical reduction and nanoemulsion methods. It also compared the advantages, disadvantages and limitations of each method. Single components phase change nanoparticles may not be able to fulfill the requirement of large temperature range cooling system, therefore, multicomponent eutectic alloys nanoparticles have also been designed and synthesized to extend the temperature range. Encapsulation of metallic and polymeric phase change nanoparticles have also been introduced in this section. Examples of typical silica and polymer encapsulated phase change nanoparticles have shown the novelty of those techniques. The thermodynamics and kinetics of phase change behavior also have been discussed.

CHAPTER 4 ENHANCEMENT ON HEAT TRANSFER

4.1 Introduction

As the fast development of electronics, electrical, and automatic industries, the generated heat is continually increasing due to trends toward faster speeds and smaller volumes for microelectronic devices, higher power output for engines and brighter beams for optical devices. The higher temperature increases, the faster failure will happen on those devices. Though all three modes of heat transfer (conduction, convection and radiation) can be used for cooling, the utilization of heat transfer fluids by taking the advantage of the large heat flux of convection is one of the most common and effective ways. HTFs have been found in many industrials and civil applications, for instance, automotive, aerospace, air-conditioning and electronic cooling, etc. However, the low thermal conductivity and limited heat capacity of the heat transfer fluids are limiting factor in the design of the cooling systems. The increasing power but decreasing size of the equipments calls for innovative cooling technologies and now the thermal management has become one of the top technical challenges and a primary concern of component design. A conventional method is to increase the flow rate, however, has reached a limit. With the increasing demand for machines and devices to operate efficiently, the seeking for new HTFs with higher thermal conductivity and more effective cooling capacity is an emergency now. The research and development work have been carried out to improve the heat transport properties of conventional heat transfer fluids.

If the flow rate of heat transfer liquid is constant, the heat transfer ability will be dependent on the thermal conductivity and heat capacity of liquid.[5] The practice of adding nanoparticles into liquid has been studied with hope that the thermal conductivity can be enhanced dramatically. But, recent experiments show no anomalous enhancements in the thermal conductivity when nanoparticles such as copper, and alumina are added into fluid.[56, 207] On the other hand, the heat transfer efficiency depends on the heat capacity of the liquid, providing an alternate for the enhancement of heat transfer ability of liquid.[208] However, the heat capacity of pure liquid is often small, because the specific heat of liquid is not a sensitive function of temperature, and the temperature difference between hot source and cold source is low.

Nanostructured materials have created numerous opportunities to dramatically change traditional industrial areas.[209-210] A large variety of nanoparticles with unique physical characteristics including optical, magnetic, electronic, chemical and mechanical ones have been used either alone or as functional additives to improve the performance of materials.[211-219] The structures, composition and surface properties, as well as the assembly of nanoparticles can be tuned with high level of precision to allow bottom-up construction of novel materials.[220-224] The solid-liquid phase change materials (PCMs) are very important to thermal energy storage and heat transfer applications due to their narrow melting range and large latent heat of fusion. PCMs offer a superior storage density compared to sensible heat storage materials when used in small temperature intervals around the melting temperature T_m, which is illustrated in Figure 22.

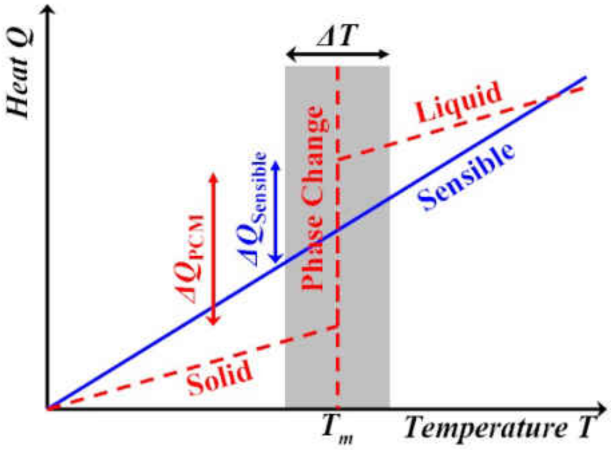

Figure 22. Solid-liquid phase change behavior.

A material with a phase change property does not change its temperature during the phase change but stores a large amount of energy. Only after the phase change is completed, the temperature continues to rise or fall. Due to this intrinsic buffer effect, large latent heat of fusion, precise melting temperature, good dispersion ability in liquid, and short melting time would allow their applications in high flux heat storage and transfer after dispersing in an appropriate liquid. Owing to their small sizes and large surface to volume ratios, nanoparticles have been added into solid or liquid media to form homogeneous mixture with intimate contacts.[225] On the other hand, an area with great importance is heat transfer, in which a liquid (i.e., coolant) is used to transfer thermal energy from a hot source to a cold source.[226] Indium nanoparticles have been added into a single phase liquid to enhance its heat adsorbing ability.[89] But, the colloid suspension of bare indium nanoparticles has only limited uses in heat transfer due to several reasons: the nanoparticles have fixed melting point that cannot satisfy multiple cooling needs at different temperature; molten nanoparticles will aggregate and precipitate out of fluid during multiple melting-crystallizing processes; the metallic nanoparticles reduce dielectric property of liquid, which limits its applications such as the direct cooling of electronic devices, even if direct contact cooling is desired due to its minimized contact thermal resistance.

A general strategy has been developed to enhance the heat transfer properties of liquids, where phase change materials (i.e., metal and paraffin wax) that have appropriate thermal properties are down-sized to be nanoparticles, encapsulated inside non-melting shells (i.e., silica and polymer), and then added into liquids (i.e., poly-α-olefin and water) to enhance the heat capacities of according liquids for high and low temperature applications, respectively. Upon the solid-liquid phase changes, the nano-PCMs absorb thermal energy from hot source and become liquid; non-melting shells prevent the leakage or agglomeration of molten cores; and the molten cores solidify at cold source to release thermal energy (Figure 23).

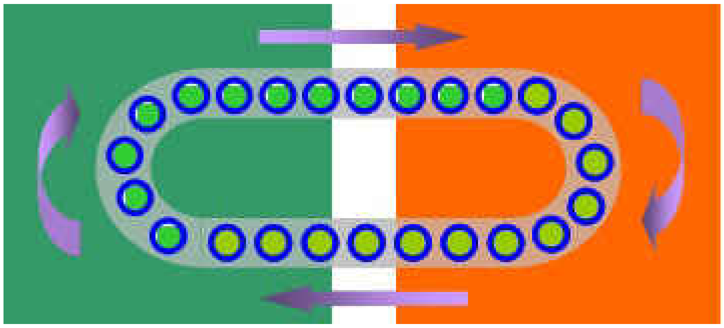

Figure 23. Heat transfer enhancement by using encapsulated phase change nanoparticles.

4.2 Experiments

4.2.1 Synthesis Approach

4.2.1.1 Synthesis of silica encapsulated indium nanoparticles

All chemicals used in this experiment are obtained from Aldrich without purification. Direct emulsification of appropriate precursors is used to prepare metallic nano-PCMs. In the case of indium that has melting point of 156°C, emulsification is carried out by boiling certain amount of indium powder (-325 mesh) in poly-α-olefin (PAO) at 200°C with magnetic stirring under protection of nitrogen, an ultrasound sonication could also be used to assist the uniformity and particle size reduction. The nanoparticles are then subtracted from PAO by centrifuging at 4000 rpm for 10 min, and washed with ethanol (90%). Such washing and centrifuging processes are repeated for three times.

The precursor used to encapsulate nano-PCMs is tetraethoxysilane (TEOS). Sol-gel method is used to form thin silica shell around nano-PCMs. After redispersing 50 mg nanoparticles into 50 ml of ethanol, 2 ml of NH_4OH at the concentration of 28%, and 0.2 ml of TEOS are added drop-wisely into the solution. The mixture is then sonicated by a Brason 2510 sonicator at 70°C for 1.5 hours to decompose TEOS and make silica shells formed around nanoparticles (Figure 24). After finishing encapsulation the mixture is centrifuged to remove the top clear liquid and washed by ethanol. The washing and centrifuging process are repeated for three times to ensure the complete removal of residual TEOS. There are many surfaces that can be directly coated with silica because of the significant chemical affinity of these materials, like clay minerals, hematite, zirconia and titania,[227] however, many other surfaces can only be coated with the help of stabilizers, surfactants, silane coupling agents, or a fast precipitation from a water glass solution, and most of these coating methods are multi-step processes. For the encapsulation of bismuth using silica, bismuth is likely to be a positive charge, while silica is preferable to be negative charge, plus the high surface energy of new generated small silica particles; it is much easy for silica particles to attach on the surface of bismuth nanoparticles. Sol-gel method is used to encapsulate nanoparticles with silica after removing nanoparticles from PAO by centrifuging.[104] Tetraethyl-orthosilicate (TEOS) is added in an ethanol suspension of indium nanoparticle, followed by drop-wisely adding ammonia hydroxide at 60ºC. After reacting for 90 min, encapsulated nanoparticles are washed by ethanol for several times and re-dispersed in PAO at certain ratio.

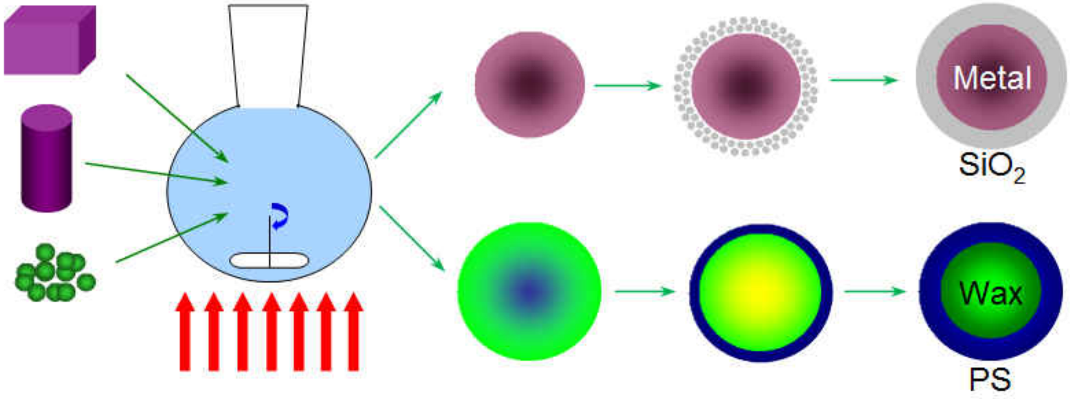

Figure 24. Colloidal synthesis of encapsulated phase-change nanoparticles.

4.2.1.2 Synthesis polystyrene encapsulated paraffin wax nanoparticles

A one-pot nanoemulsion method is used to make polymer encapsulated paraffin wax nanoparticles.[228-229] 10.0 g of octadecane with melting point of 28ºC, 1.0 g of acrylate acid and 0.1 g of dodecylmercaptan are dissolved in 10.0 g of styrene by sonication for 10 min. The mixture is poured into 30.0 g of aqueous solution that contains 0.2 g of sodium dodecylsulfate and 0.2 g of Triton X-100 in a 250 ml three-neck flask. The mixture is sonicated for 10 minutes to form a stable emulsion. The flask is purged by nitrogen for 30 min, followed by heating at 70ºC for 12 hrs at 200 rpm to complete polymerization. The schematic procedure is also shown in Figure 24.

This is a typical oil-in-water miniemulsion process, where wax and styrene are non-polar materials which are miscible with each other and become well-dispersed, stable liquid droplets when heated at an appropriate temperature under the protections of surfactants like Triton X-100 and sodium dodecylsulfate. The size of the droplets can be controlled by high shear forces applied either by ultrasound or mechanical stir, or even both. The size of the emulsions depends on the ultrasound power, stirring speeds, and amount of stabilizers. The stabilizers/surfactants should have good solubility in the disperse phase (mixture of styrene monomer and wax), but at the meantime, it should also show a lower solubility in the continuous phase (water).

The polymerization process is usually started with an initiator like dodecylmercaptan or 2,2′-Azobis(2-methylpropionitrile), which can break the double bonds of styrene monomer and let the polymerization propagate at suitable conditions. Polystyrene is more hydrophilic than styrene monomer, therefore, the polymerized polymer is tend to form at the interface of water and the liquid droplets, which contains a diffusion process in the liquid droplets. The diffusion coefficient depends on the viscosity of liquid droplets and reaction temperature. Usually it takes 6 to 12 h to finish the whole process (99% is polymerized).

4.2.2 Characterizations

The chemical, thermal and physical properties of nano-PCMs and colloidal suspensions are very important information for the deep understanding of mechanisms behind the heat capacity enhancement, where those properties are going to fully evaluate the performance of the heat transfer fluids as well as their potential applications in both civil and military industries. The as made encapsulated nano-PCMs and heat transfer properties of colloidal suspensions have been characterized using a variety of techniques. The characterization of nano-PCMs includes microstructure characterization, composition investigation, latent heat and heat capacity measurement, structure analysis and size distribution and mobility investigation. The characterization of nano-PCMs suspension includes dielectric properties and viscosity measurements, heat transfer behavior evaluation.

4.2.2.1 Physical properties analysis

In this study, a JEOL 1011 TEM (100 kV) and a TECNAI F30 TEM (200kV) were used to study the core-shell nano-PCMs for imaging, SAED, and in-situ phase change experiment. In order to prepare sample for TEM imaging, an ethanol drop containing nanoparticles is dropped on a copper TEM grid that coated with carbon formar film. The composition of polystyrene encapsulated wax nanoparticles is determined by a Perkin Elmer Spectrum 100 Series FTIR with a scan range of 650-4500 cm^{-1} on a reflection mode. Few drops of polystyrene encapsulated wax nanoparticles in water solution is spread on a silicon substrate and dried at room temperature for testing. A PerkinElmer DSC7 is used to measure the thermal physical properties of nano-PCMs. A sample of about 10 mg is hermetically sealed into an aluminum pan and placed inside the DSC chamber under continuously purged nitrogen gas. Dynamic scans are performed on the samples at the heating rate of 10ºC/min from room temperature to a set temperature and cooling down to the initial temperature. X-ray diffraction analysis (XRD) is carried out on a Rigaku 2500 diffract meter using Cu Kα radiation (40.0 kV and 30.0 mA) at a step width of 2.0 º/min. To collect XRD curves, powders of nanoparticles are glued on a double side tape and fixed on XRD holder.

Size distribution of encapsulated phase change nanoparticles have been investigated by adding a small amount of nanoparticles into 1.5 ml water in a plastic cuvette. A PD 2000 DLS instrument with a laser light source having a laser wavelength of 685 nm and power of 30 mW was used for the measurement at 20ºC. The scattering angle is 90º.

The capacitances of fluids with and without nanoparticles are determined by a LCR meter (Instek LCR-819), where L, C, and R stand for inductance, capacitance and resistance, respectively. A self-built LCR probe with two parallel electrodes with surface area of 1 cm^2 and gap of 1 mm is immersed in liquid.

The viscosity of colloid suspensions were measured using two methods. Firstly, the number of viscosity was obtained by measuring times they take to flow through a capillary, which can be called capillary method. Assuming the suspensions are Newtonian without kinetic energy terms, the flow time is proportional to the viscosity as:[230]

$$\eta = \frac{\pi r_c^4 \Delta P}{8 V_f L} t = A\rho t \tag{17}$$

where r_c and L are the radius and length of the capillary, V_f is the volume of liquid that flows through the capillary, and ΔP is pressure difference. If gravity is the driving force for the liquid flow, ΔP is equal to ρgh where ρ is the solution density, and A is a constant. Secondly, the viscosity is measured by a low-range Brookfield rotational viscometer, where the measuring range is from 15 to 2,000,000 cP. The viscosity of PAO is about 9.8 cP, therefore, we have designed a spindle that has a larger surface area for the measurement. Because the linear relationship between the surface area and shear force, the true value can be obtained by simply multiply a factor related to the original spindle.

4.2.2.2 Heat transfer evaluation

The heat transfer properties of colloid suspensions are measured on a self-built heat loop, which consists of microchannel heat exchanger, gear pump, valve, flow meter and heat exchanger (Figure 25). The nano-PCMs suspension is pumped from the fluid reservoir using a diaphragm pump. The valve is used to adjust the flow rate in the loop. The flow rate is measured by two rotameters with scale of 1,262 and 2,524 ml/min. Two mixing sections are used to disturb fluid so that temperature can be measured the temperature at the inlet and outlet of the heat exchanger. The heat exchanger is used to cool working fluid after it left the test section. Two thin film resistors soldered at the bottom of microchannel heat exchanger are used as heaters. The power to the resistors is supplied by a DC power supply that is adjustable to change the amount of heat generated by the heater. A pair of thermocouple is attached at the backside of the thin-film resistor to measure wall temperature. The power to the heater is multiplied by the voltage applied on the heater and current that passes through it.

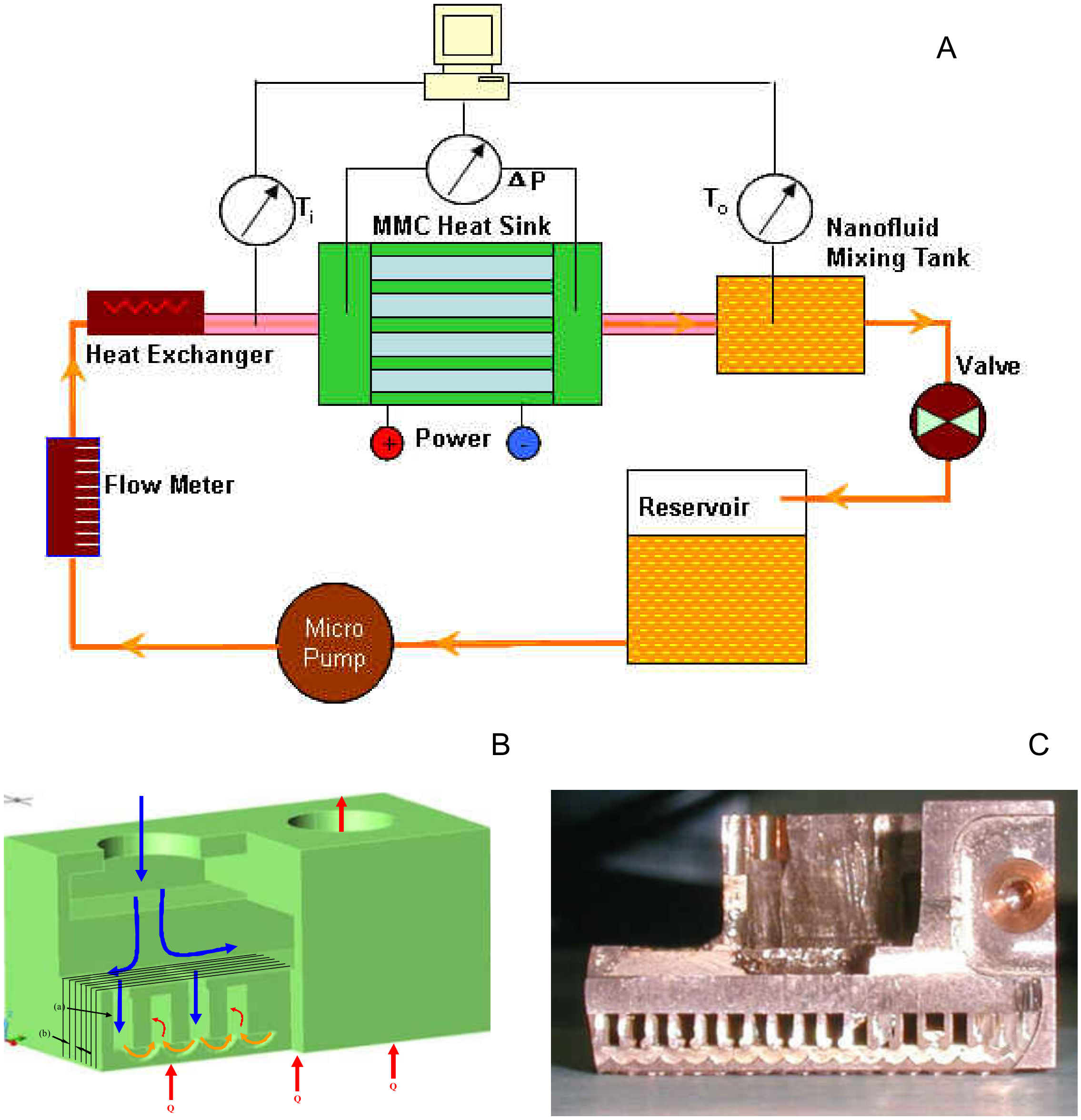

Figure 25. The heat loop test setup (A) and structure of microchannels (B) and real image of microchannels (C).

4.3 High Temperature Enhancement

4.3.1 Encapsulated indium nanoparticles

The surface morphologies were studied by SEM and TEM. Figure 26A shows a SEM image of silica encapsulated indium nanoparticles. The silica shells are smooth which showing that nucleation of silica is initiated from surfaces of indium nanoparticles. Figure 26B is a bright field TEM image of silica encapsulated indium nanoparticles obtained from the JEOL 1011 TEM. Indium and silica shell have different absorptions to the electrons, therefore, the image shows different contrast of silica shell and indium core. The three-in-one core-shell structure confirms the indium has been encapsulated by silica shell.

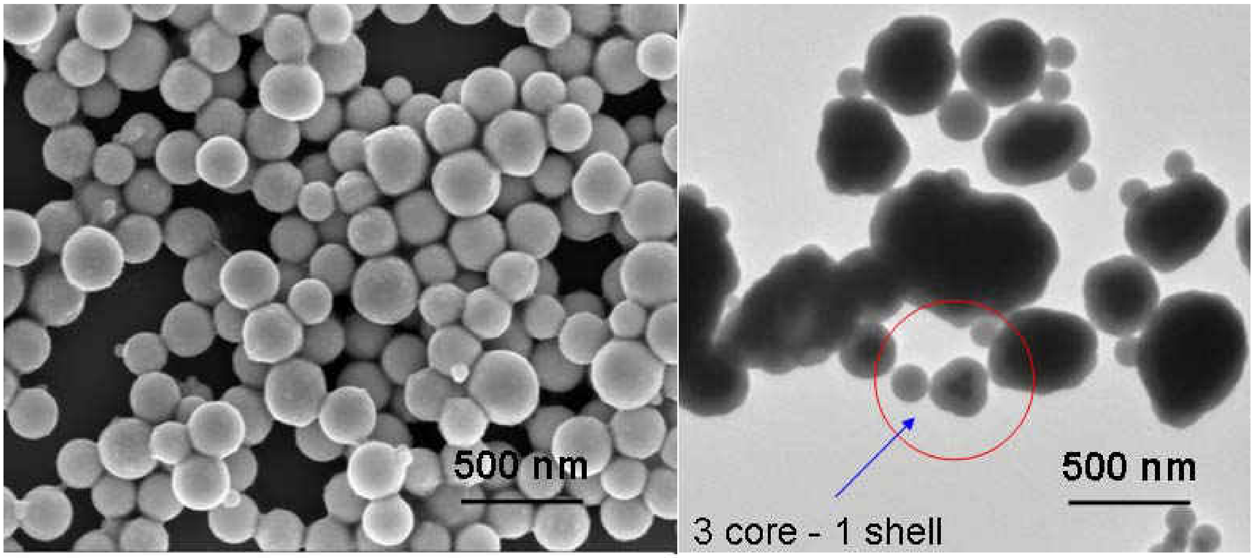

Figure 26. SEM (A) and TEM (B) images of silica encapsulated indium nanoparticles.

The size distribution of silica encapsulated indium nanoparticles measured by DLS in Figure 27 shows the average diameter is 200 nm with majority of nanoparticles in the range of 100-300 nm.

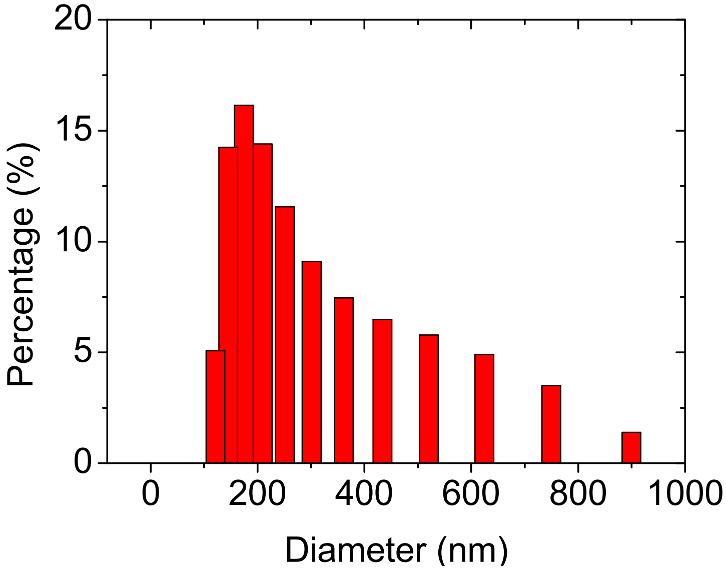

Figure 27. Size distribution of silica encapsulated indium nanoparticles.

XRD spectra are collected by sticking indium powder and nanoparticles onto a sample holder, and scanned from 20 to 80º at speeds of 2º/min. The results show that indium power and nanoparticles have tetragonal structures with three strong peaks at 33, 37 and 40º for the diffraction of (011), (002) and (110) planes, respectively (Figure 28), where small oxidized indium peaks can be found at 31, 36, 52 and 61º after boiling for more than 24 hours.

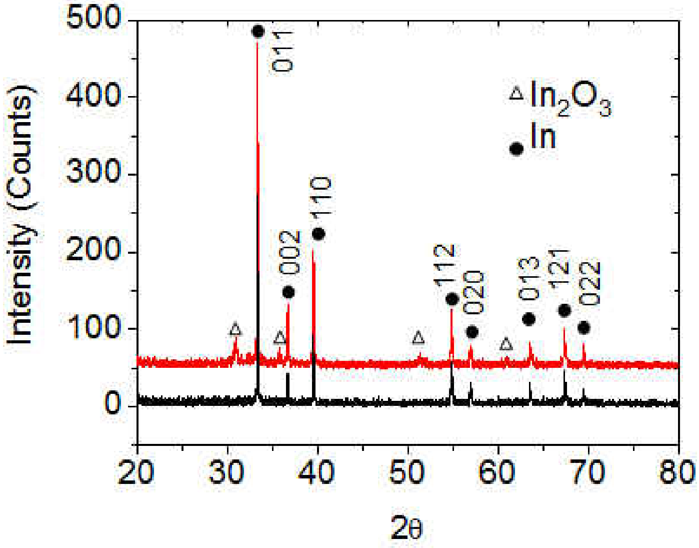

Figure 28. XRD spectrum indium powders (black) and nanoparticles (red).

The melting temperature and latent heat of fusion of encapsulated nano-PCMs have been studied at heating rate of 2ºC/min on DSC by adding certain amount of nanoparticles in an aluminum pan. Figure 29 shows DSC curves of pure indium nanoparticles and silica encapsulated indium nanoparticles, where the melting and freezing temperatures are at 155.3 and 135ºC, respectively. The enthalpy of fusion is derived as 19.6 J/g from the area of melting peak of silica encapsulated indium nanoparticles, which is lower than that of pure indium value (28.5 J/g). The difference is due to presence of silica, which does not melt unless ambient temperature is over 1600ºC. The mass ratio of indium inside encapsulated nanoparticles is determined to be 68.8% from the ratio those enthalpies

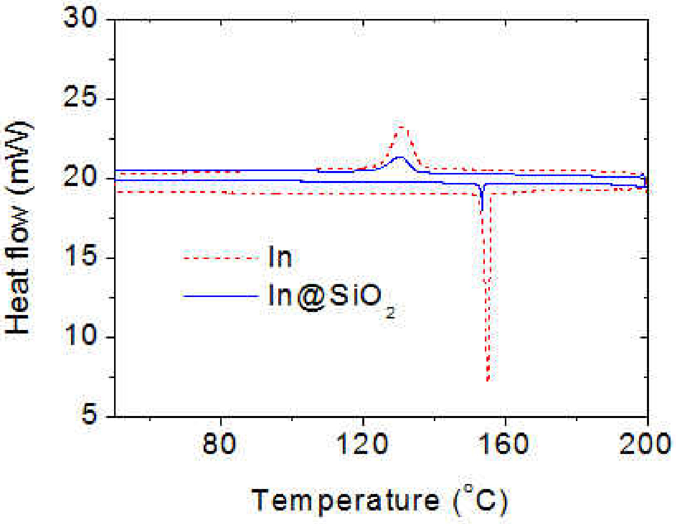

Figure 29. DSC curves of pure indium nanoparticles (dash) and silica encapsulated indium nanoparticles (solid).

4.3.2 Heat transfer behavior of encapsulated indium nanoparticles

The heat transfer behaviors of encapsulated nano-PCMs colloids are studied on the heat transfer loop (Figure 30), where the major part is a $2 \times 1 \times 1$ cm^3 heat exchanger that has 8,000 microchannels with dimensions of $25\times100\times500$ μm^3 (width × height × length). A 500 ml PAO with pure indium nanoparticles or PAO with silica encapsulated indium nanoparticles is pumped between a hot source and a cold source. The pressure drop at the inlet and outlet of microchannel is monitored to ensure continuous flow of nano-PCMs suspensions. The heat transfer coefficient has been defined as:

$$h_1 = Q_{fluid} / A_{base} \Delta T_m \tag{18}$$

where A_{base} is the surface area of microchannel heat exchanger, ΔT_m is the temperature difference between the inlet and outlet of the heat exchanger (which will be calibrate using log mean temperature difference), and Q_{fluid} is the heat absorbed by the fluid which is defined as:

$$Q_{fluid} = mC_P(T_{fluid,O} - T_{fluid,i}) \tag{19}$$

Log mean temperature difference is defined as

$$\Delta T_m = \frac{(T_w - T_i) - (T_w - T_0)}{\ln[(T_w - T_i)/(T_w - T_0)]} \tag{20}$$

which is also used to indicate the heat transfer behavior, where T_w is the temperature of copper between resistors and microchannel heat exchanger. Figure 19A shows the log mean temperature difference as the function of inlet temperature. The log mean temperature difference is nearly constant as the inlet temperature increases from 130 to 145ºC, but the routes for pure PAO, PAO containing 30% pure indium nanoparticles and PAO containing 9% silica encapsulated indium nanoparticles are different, where pure PAO has no peak, but both the latter two fluids have a peaks, and the peak area is proportional to the mass ratio of phase change nanoparticles, indicating the melting of indium between 145 to 158ºC. Figure 30B shows the heat transfer coefficient as the function of inlet temperature by using equation 18. The maximal heat transfer coefficient of PAO with 30% indium nanoparticles is 60% higher than that of PAO. In the case of PAO containing 9% silica encapsulated indium nanoparticles, the maximal heat transfer coefficient is 26% higher than that of PAO at 152ºC.

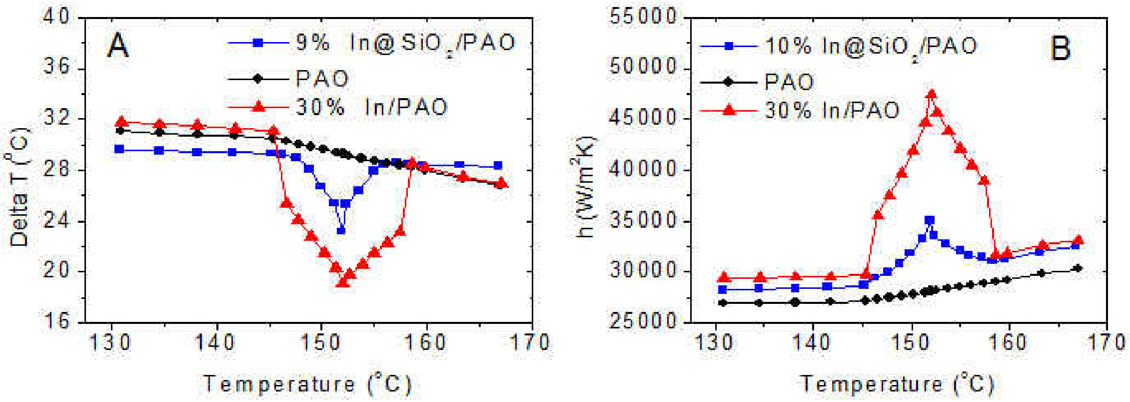

Figure 30. Log mean temperature difference (A) and heat transfer coefficient (B) of silica encapsulated indium nanoparticles as function of temperature.

The heat capacity of PAO with indium nanoparticles is less than that of PAO when temperature is below 140°C due to the lower heat capacity of indium; the temperature difference reaches minimum at 152ºC due to the melting of indium nanoparticles. The same trend is observed in the case of PAO with silica encapsulated indium nanoparticles. The heat capacity of 30% In/PAO nano-PCMs colloid is 2.6 times higher than pure PAO, which has been confirmed by the large specific heat of PAO with indium nanoparticles at 150ºC (Figure 31).

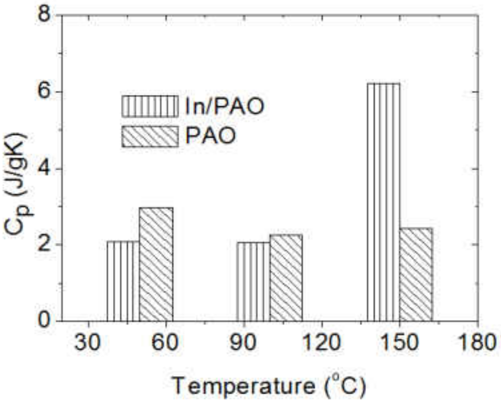

Figure 31. Heat capacity of indium nanoparticles as function of temperature.

In order to exploit the latent heat of fusion, nano-PCMs have to melt and recrystallize during the heat loop, thus flow rate and melting time will be important parameters. Figure 32 shows the heat transfer coefficient as a function of flow rates of PAO, PAO with 30% indium nanoparticles, and PAO with 9% encapsulated indium nanoparticles. At the same flow rate, PAO containing 30% nanoparticles has higher heat transfer coefficient than PAO itself or PAO containing 9% nanoparticles, but the maximum flow rates of PAO containing both bare and encapsulated nanoparticles are much lower than pure PAO, which is probably due to the higher viscosity and clogging of microchannels.

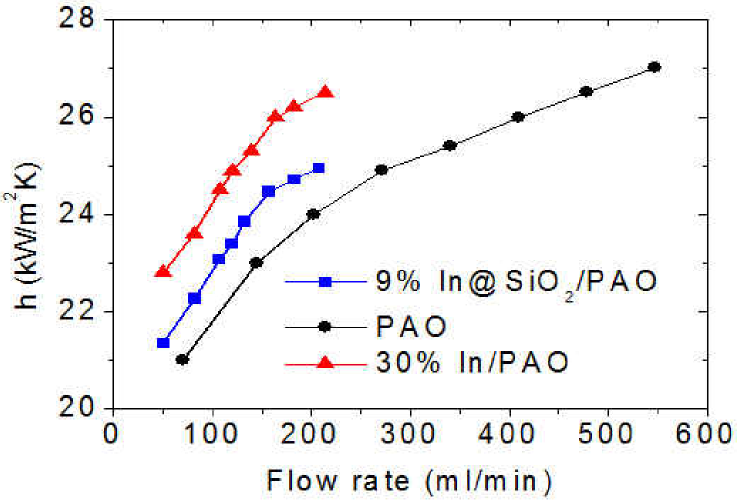

Figure 32. Heat transfer coefficient as function of flow rate.

4.4 Low Temperature Enhancement

4.4.1 Encapsulated paraffin wax nanoparticles

The morphology and composition of polystyrene encapsulated paraffin nanoparticles have been characterized. SEM image shows the average diameter of nanoparticles is about 200 nm (Figure 33A), which has been confirmed by the DLS measured size distribution of polystyrene encapsulated nanoparticles in Figure 34, where the measured diameters varies from 100 nm to 300 nm. TEM image (Figure 33B) shows the diameter of PCM cores and the polymer shell are 150 and 25 nm, respectively.

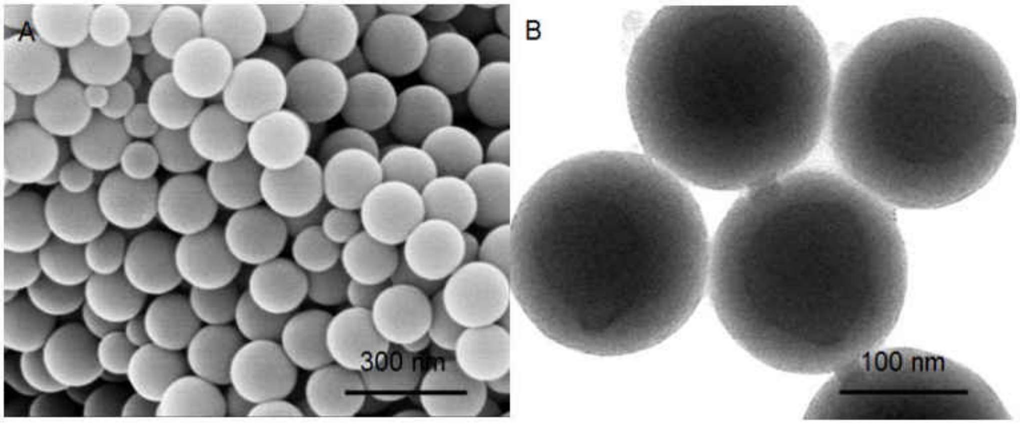

Figure 33. SEM (A) and TEM (B) images of polystyrene encapsulated paraffin nanoparticles.

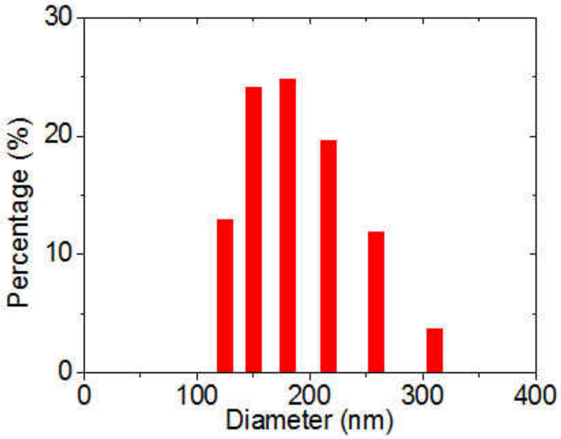

Figure 34. Size distribution of polystyrene encapsulated paraffin nanoparticles.

FTIR spectra confirm the formation of polystyrene encapsulated paraffin nanoparticles (Figure 35). The two absorption peaks at 2916 and 2848 cm^{-1} are the characteristic peaks of the aliphatic C-H stretching vibration, the absorption peaks at 1464 cm^{-1} is assigned to the C-H bending vibration, and the peak at 721 cm^{-1} is associated with the in-plane rocking vibration of the CH_2 group. From spectrum (2), it can be seen that there are six more peaks, the absorption peaks at 3060 and 3026 cm^{-1} are associated with the aromatic C-H stretching vibration, the absorption peak at 2923 cm^{-1} is associated with aliphatic C-H stretching vibration, the absorption peaks at 1601 and 1490 cm^{-1} are associated with benzene ring C=C stretching vibration, and the absorption peaks at 756 and 700 cm^{-1} are benzene ring deformation vibration. These peaks are assigned to polystyrene. The characteristic peaks of paraffin wax could be observed in the FT-IR spectrum of the polystyrene encapsulated paraffin nanoparticles. It is noted that the peaks of aliphatic C-H stretching vibration red shifts from 2916 and 2848 cm^{-1} to 2924 and 2853 cm^{-1} respectively, as a result of the interaction between paraffin core and polymer shell.

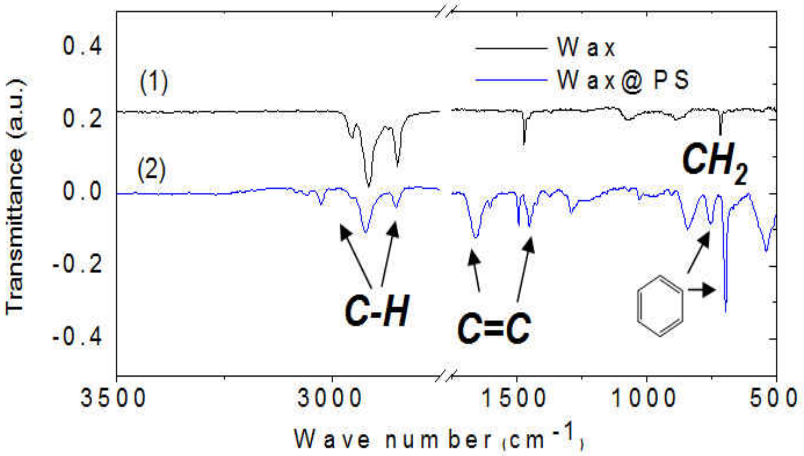

Figure 35. FTIR spectra of pure paraffin (curve 1) and polystyrene encapsulated paraffin nanoparticles (curve 2).

Figure 36 is DSC curves of paraffin and polystyrene encapsulated paraffin nanoparticles showing the phase change behavior, where the melting and solidifying peaks of paraffin are 27.8 and 19.2°C, respectively, close to those of encapsulated paraffin nanoparticles (27.1, and 19.6°C), respectively. The slight peak shifts may be due to the interaction of paraffin with polymer. The enthalpy of phase change of paraffin is calculated from the melting peak as 232.3 J/g. The enthalpy measured from encapsulated paraffin is determined to be 110.05 J/g, indicating the mass ratio of paraffin is ~47.4 wt%, which is close to the designed value (50% by mass).

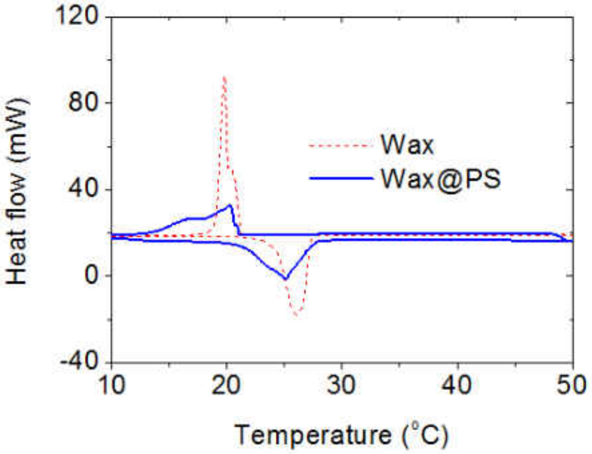

Figure 36. DSC curves of paraffin (dash) and polystyrene encapsulated paraffin nanoparticles (solid).

4.4.2 Heat transfer enhancement of polymer encapsulated wax nanoparticles

The heat transfer properties of encapsulated paraffin nanoparticles have been tested in the same way as PAO containing indium nanoparticles. Figure 37A shows the log mean temperature difference as function of inlet temperature for encapsulated paraffin nanoparticles, where the temperature difference reaches minimum at 24.2ºC due to the melting of paraffin nanoparticles. The maximal heat transfer coefficient of water with 10% encapsulated paraffin wax is 75% higher than that of water alone (Figure 37B).

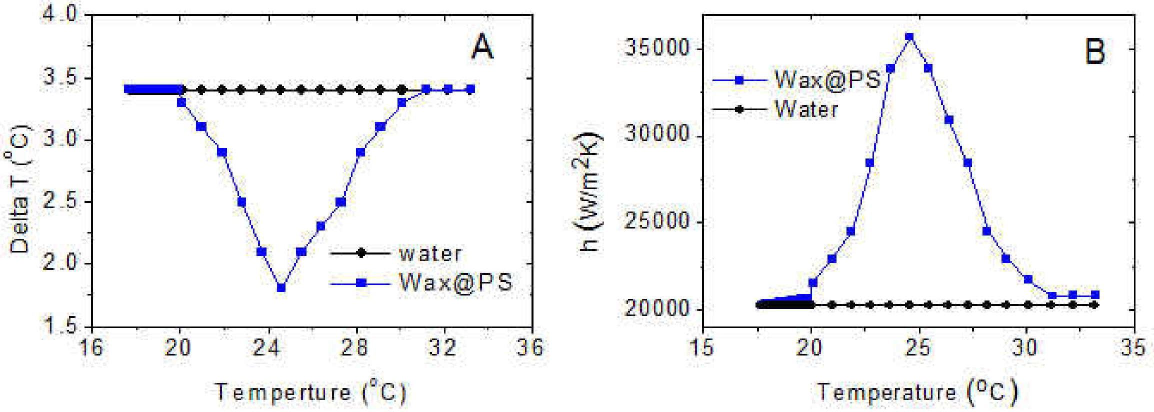

Figure 37. Log mean temperature difference (A) and heat transfer coefficient (B) of polystyrene encapsulated paraffin nanoparticle as function of temperature.

4.5 Stability Investigation

4.5.1 Stability of morphology and physical behavior

The stability of encapsulated nanoparticles is studied both on morphologies and physical properties, where the encapsulated nano-PCMs are stable after ~100 melting-freezing cycles. TEM images of silica encapsulated indium nanoparticles and polystyrene encapsulated paraffin wax nanoparticles after the loop test are shown in Figure 38A and 38B, respectively, where the core and shell structures of encapsulated nanoparticles are preserved.

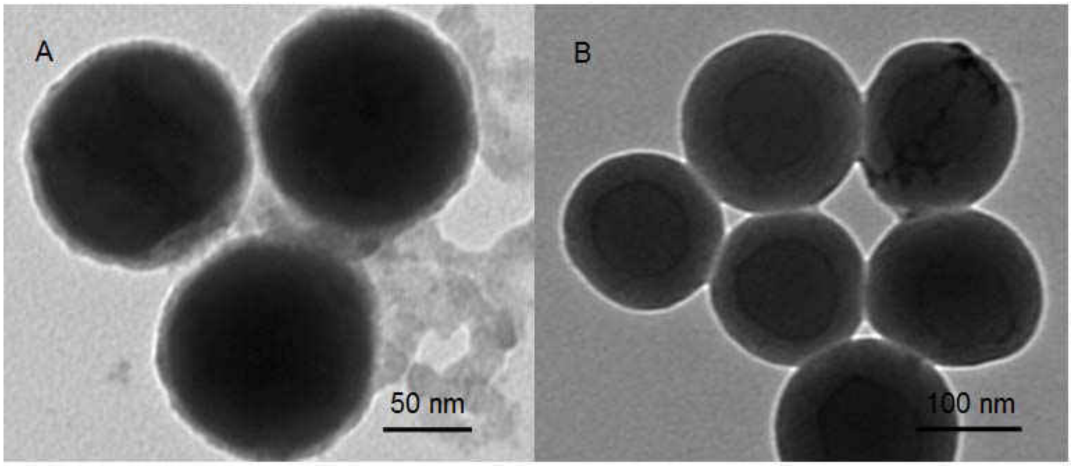

Figure 38. TEM images of silica encapsulated indium nanoparticles (A) and polystyrene encapsulated paraffin nanoparticles (B) after the loop tests.

The silica shells prevent leakages and coalescences of molten materials, and ensure the stability of colloidal suspension.[231] We have observed the thermal stability of silica shells around nanoparticles using in-situ TEM coupled with a heating stage. Figure 39A and 39B indicate the TEM images collected at room temperature and at 250°C, respectively. Although there is no remarkable difference in the topography images, the changes in diffraction patterns from bright spots to diffusive cloud confirm the solid-liquid phase changes of encapsulated nanoparticles (Figure 39C and 39D).

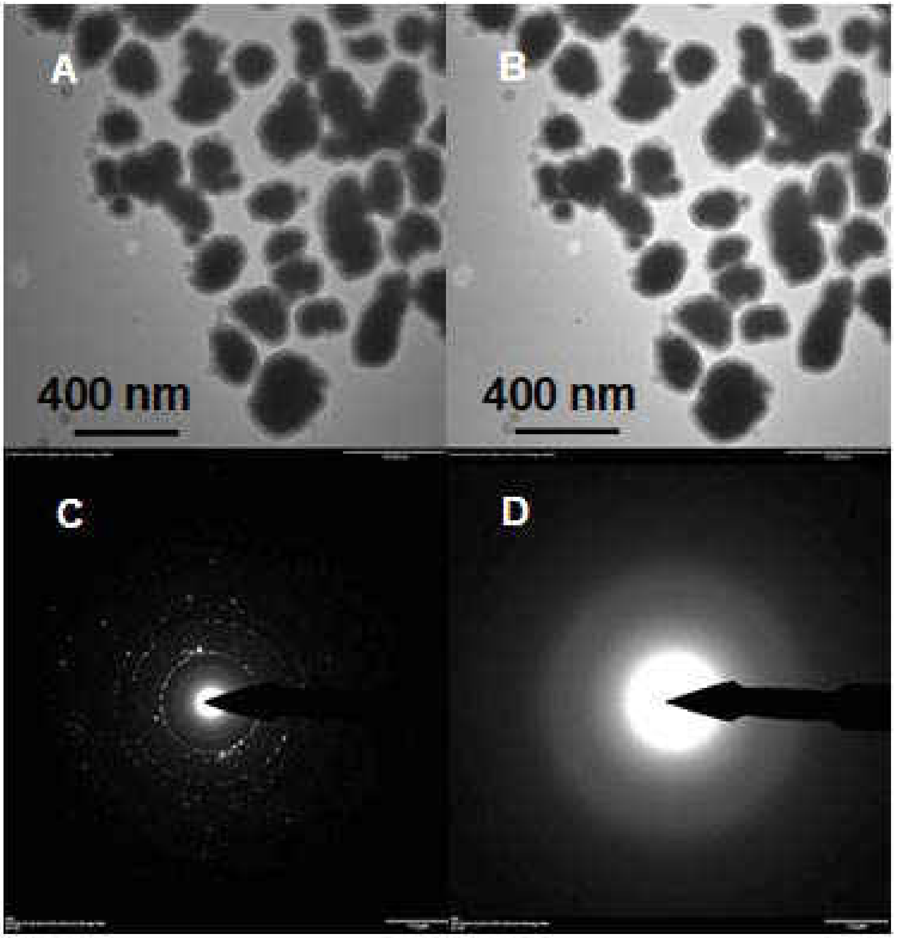

Figure 39. TEM images of silica encapsulated indium nanoparticles before (A) and after (B) heating to 250°C; Electron diffraction pattern of silica encapsulated indium nanoparticles before (C) and after (D) heating to 250°C.

The silica shell breaks as temperature increases to 650ºC (Figure 40A), where the damage to shells can be induced by pressure difference inside (metal vapor) and outside the shell (vacuum). In comparison, un-encapsulated nanoparticles start to aggregate by forming bridging structures between adjacent nanoparticles at 300ºC (Figure 40B). Thus, as long as the temperature is less than 200ºC, silica shells protect cores from leakage for a long time, and the thermal behaviors can be repeatable for many times.

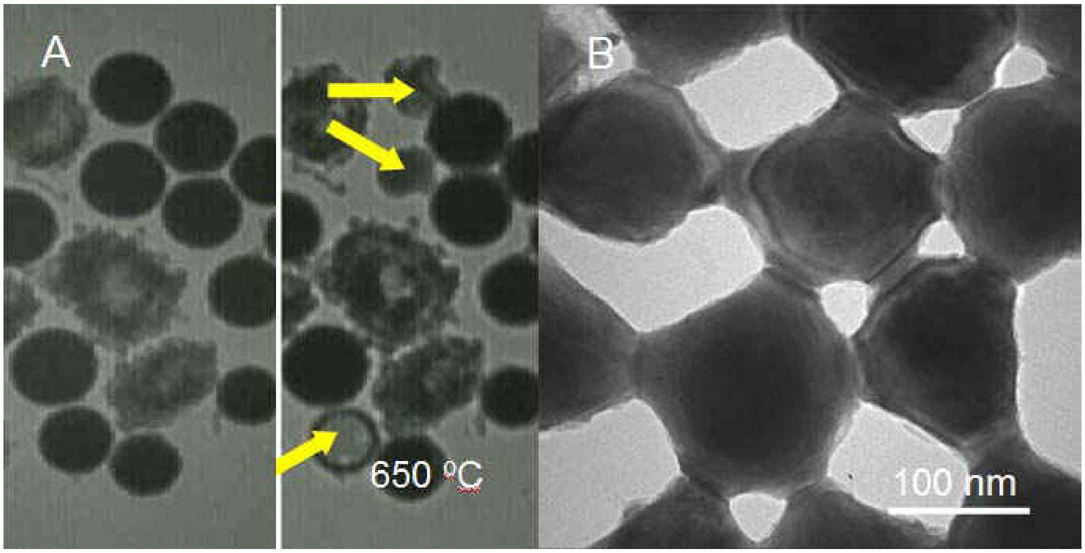

Figure 40. TEM images of encapsulated indium nanoparticles before (left) and after (right) heating to 650ºC, where silica shell breaks as temperature above 600ºC (A). Bare phase change nanoparticles aggregate by bridging between adjacent nanoparticles at 300ºC (B).

4.5.2 Precipitation of nanoparticles in fluids

In absence of Brownian motion, for a small spherical particle (low Reynolds number), the drag on the particle is given by:

$$F = 3\pi\mu v D \tag{21}$$

$$F = mg \tag{22}$$

$$m = \frac{1}{6}\pi\rho D^3 \tag{23}$$

$$\mu = 0.1628T^{-1.0868} = 0.006276\,(20^{\circ}\mathrm{C}) \tag{24}$$

Combining (21) - (24):

$$\begin{aligned} v &= \frac{mg}{3\pi\mu D} = \frac{\rho D^2 g}{18\mu} = \frac{7.31g/cm^3 D^2 9.8m/s^2}{0.112968Ns/cm^2} \\ &= \frac{7.31\times10^{-3}\times10^{6}(Kg/m^3)\cdot D^2 9.8(m/s^2)}{0.112968\times10^{4}Kg\cdot(m/s^2)\cdot s/m^2} = 63.4144D^2 m/s \end{aligned} \tag{25}$$

where μ is the dynamic viscosity=0.1628T-1.0868 (Pa·S),[232] v is the relative velocity between the particle and the surrounding liquid, D is the diameter of the particle, m is the mass of particle, g is gravity acceleration ($9.8m/s^2$), ρ = density of particles = $7.31g/cm^3$. From Figure 41 we can find out that when the diameter of the nanoparticle is 100 nm, the precipitation velocity is 6.34×10^{-13} m/s, which indicating it takes 17615 hours (733 days) to precipitate 1 μm. While, when the diameter of the nanoparticle is 10 μm, the precipitation velocity is 6.34×10^{-9} m/s, which indicating it takes 1.8 hours to precipitate 1 μm. The smaller the phase change nanoparticles, the more stable the nano-PCM suspensions. The theoretical calculation seems to be favorable, but the real situation may also depend on the particle-particle interaction and particle-fluid interaction, and the precipitation time may vary a lot. We will continue to study the two interactions afterwards so as to prove the stability of nano-PCM suspensions.

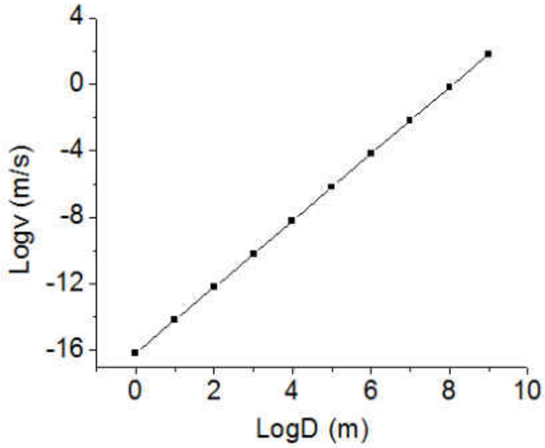

Figure 41. Log velocity of precipitation speed as function of log velocity of diameter of phase change nanoparticles.

4.6 Dielectric Properties of Colloidal Suspension

Depending on whether nanoparticles are conductive or not, adding nanoparticles into liquids will decrease or enhance dielectric properties of liquids. We have measured the capacitances of PAO, indium nanoparticles in PAO, silica encapsulated indium nanoparticles suspended in PAO in the range of 12 Hz to 100 kHz. Figure 42 shows that indium nanoparticles decrease the dielectric constant of PAO, but silica encapsulated indium nanoparticles enhance the dielectric constants of PAO. The dielectric constants of PAO containing silica encapsulated indium nanoparticles reach the maximum at ~100 kHz; while that of PAO containing indium nanoparticles increases from 12 to 100 Hz and keeps constant to 100 kHz.

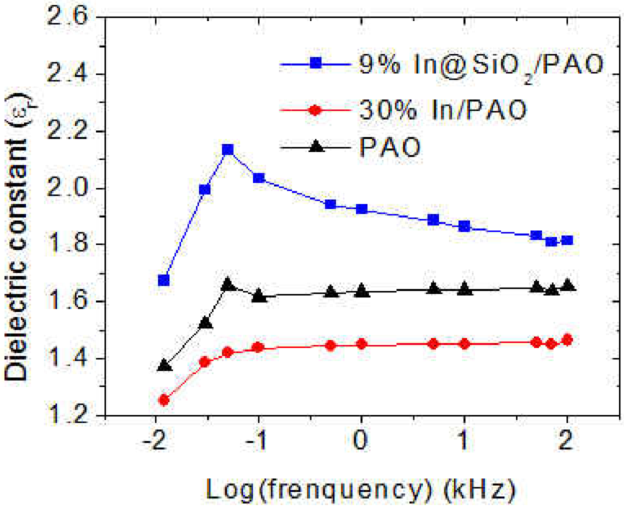

Figure 42. Dielectric constants as function of frequencies of PAO (triangle), PAO with 30% indium nanoparticles (circle) and PAO with 9% silica encapsulated indium nanoparticles (square).

The concentration dependent dielectric constants of PAO containing indium, and silica encapsulated indium nanoparticles are measured at frequency of 1 kHz as shown in Figure 43, where increasing indium content leads to a decrease of dielectric constant of PAO from 1.65 to 1.35, but increasing the content of silica encapsulated indium nanoparticles leads to an increase of dielectric constants from 1.58 to 2.17. The dielectric properties of conductive particles in a non-conductive matrix depend on percolation of charges via random chains formed by conductive particles. The percolation threshold for indium nanoparticle is at 10% of mass concentration, which is close to that for spherical conducting particles in an insulating liquid matrix (15%). The increase of dielectric constant after adding silica encapsulated nanoparticles can be contributed to the high dielectric constant of silica (4.5).

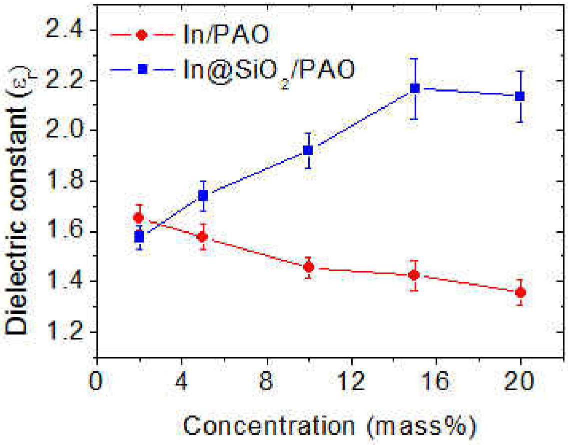

Figure 43. Dielectric constants at 1 kHz as function of the concentrations of indium (circle) and silica encapsulated indium (square) nanoparticles in PAO.

Similarly, adding polymer encapsulated paraffin nanoparticles into water enhances the dielectric constant of water (Figure 44A), and a linear relation exists between nanoparticle concentration and measured dielectric constant (Figure 44B).

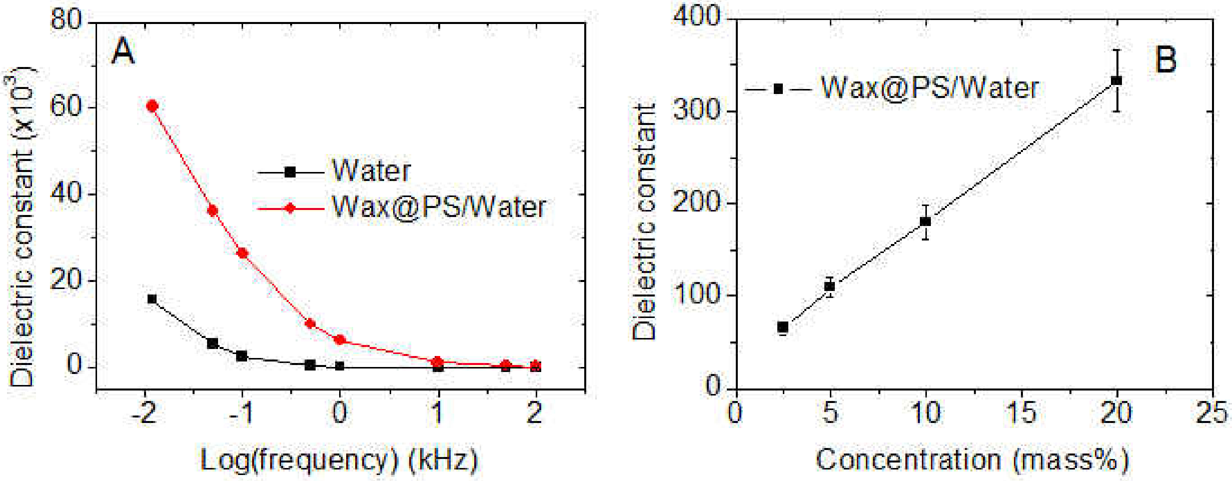

Figure 44. Dielectric constant of polystyrene encapsulated paraffin in water as function of frequency (A); and concentration dependent dielectric constants of polystyrene encapsulated paraffin nanoparticles (B).

4.7 Viscosity Investigation

The viscosities of PAO, PAO with indium nanoparticles, and PAO with silica encapsulated indium nanoparticles are studied by the self-made capillary viscometer. All of the viscosities of those fluids decrease as temperature increases from 3 to 45ºC (Figure 45A). PAO with indium nanoparticles has higher viscosity than those of pure PAO and PAO with silica encapsulated indium nanoparticles. The viscosity of PAO with silica encapsulated indium nanoparticles at 45ºC (9.49 cP) is close to that of PAO (4.68 cP). The viscosity of water-based polymer encapsulated paraffin has been measured using the same method (Figure 45B), where the viscosity of water decreases from 1.52 to 0.58 cP as temperature increases from 3 to 45ºC, and the viscosity of encapsulated paraffin decreases from 1.99 to 0.65 cP in the same temperature range. The viscosity of colloid suspension at 3ºC is 30.5% higher than water, but the difference decreases to 10.7% at 45ºC.

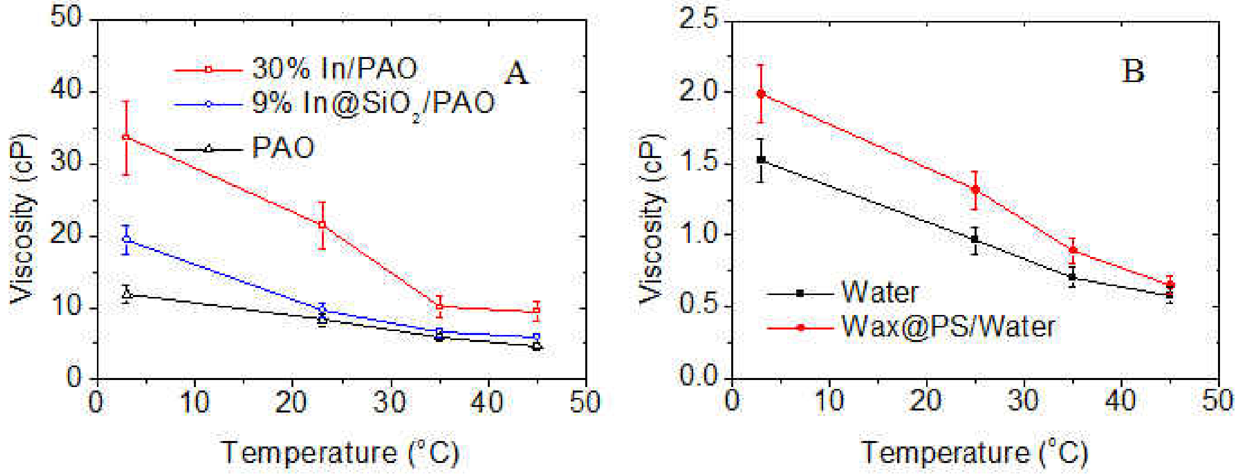

Figure 45. Viscosities of PAO (triangle), PAO with 30% indium nanoparticle (square), and PAO with 9% silica encapsulated indium nanoparticles (circle) from 3 to 45ºC (A); viscosities of water and polystyrene encapsulated paraffin wax in water from 3 to 45ºC (B).

4.8 Melting Time Simulation

Heat absorption of particles is determined by characteristics of heat conduction within particles, which in turn depends upon the particle size and material properties. Heat transfer from the fluid to the particles is controlled by the difference between fluid temperature and the surface temperature of the particles. The surface temperature determines heat transfer within the particles. Consider a solid particle at phase change temperature T_m. Neglecting the sensible heat capacity, the heat absorbed at the interface must be conducted through the liquid to the solid and is described by:[233]

$$\ddot{q} = \frac{4\pi k_l (T_s - T_m)}{1/r - 1/r_P} \tag{26}$$

where T_s and T_m are the surface temperature and the melting point of nanoparticles, respectively; r_p is the radius of the nanoparticles before melting, and k_l is the thermal conductivity of nanoparticles. In addition, neglecting the sensible heat capacity, the heat absorbed at the interface must be conducted through the liquid to the solids, which means

$$\ddot{q} = \dot{m} Q_L = (\rho_l \cdot 4\pi r^2 \cdot dr) Q_l \tag{27}$$

where ρ_l is the density of nanoparticles, and Q_l is the latent heat of fusion of the nanoparticles. Combining equation (26) and (27), and integrating gives:

$$\frac{4\pi k_l (T_s - T_m)}{(\frac{1}{r} - \frac{1}{r_p})} = \rho_l Q_l 4\pi r^2 \left(-\frac{dr}{d\tau} \right) \tag{28}$$

where τ is the melting time when the solid radius is r. The melting time is dependent on size and temperature difference between the surface temperature of the nanoparticle and the melting temperature of the nanoparticle material:

$$\frac{(T_s - T_m)\cdot\tau}{\left(\frac{\rho_l Q_l}{k_l}\right)} = r_p^2\left[\frac{1}{3}\left(\frac{r}{r_p}\right)^3 - \frac{1}{2}\left(\frac{r}{r_p}\right)^2 + \frac{1}{6}\right] \tag{29}$$

In the case of silica encapsulated nanoparticles, silica shell has a lower thermal conductivity (1.3 W/m·K) than that of metallic material, equation (29) is modified to include the contribution the silica shell:

$$\frac{(T_s - T_m)}{R_{In} + R_{SiO_2}} = 4\pi\rho_{In}Q_{In}r^2\left(-\frac{dr}{d\tau}\right) \tag{30}$$

$$R_{In} = \frac{1}{4\pi k_{In}}\left(\frac{1}{r} - \frac{1}{r_{In}}\right), R_{SiO_2} = \frac{1}{4\pi k_{SiO_2}}\left(\frac{1}{r_{In}} - \frac{1}{r_{SiO_2}}\right)$$

Integrating equation (29) gives

$$\tau\cdot(T_s - T_m) = \rho_{In}Q_{In}\left[\frac{1}{3}\left(\frac{1}{k_{In}r_{In}} + \frac{1}{k_{SiO_2}r_{SiO_2}} - \frac{1}{k_{SiO_2}r_{In}}\right)r^3 - \frac{1}{2}\cdot\frac{r^2}{k_{In}} + \frac{1}{6}\cdot\frac{{r_{In}}^2}{k_{In}} - \frac{1}{3}\cdot\frac{{r_{In}}^3}{k_{SiO_2}r_{SiO_2}} + \frac{{r_{In}}^2}{3k_{SiO_2}}\right] \tag{31}$$

where k_{In} and k_{SiO2} are 81.8 and 1.3 W/m·K, respectively, r_{In} and r_{SiO2} are 100 and 120 nm, respectively, Q_{In} is 28.52 J/g, ρ_{In} is 7.3 g/cm^3. Replace all symbols with numbers and let r equal to 0 nm, the equation (31) can be rewritten as

$$\tau(T_s - T_m) = 0.92\times10^{-7}\ \mathrm{s\cdot K} \tag{32}$$

Figure 46 shows the melting time as the function of temperature difference between surface temperature and melting temperature. The melting time τ is 0.92 μs when T_s-T_m= 0.1 K, which is two times than that of bare indium nanoparticles (0.44 μs from equation 21). At the flow rate of 210 ml/min, the resident time of nanoparticles inside a 500 μm long heat source is 2 ms. Therefore, there is still enough time at the flow rate of 210 ml/min (2 ms) for indium nanoparticles to melt even if the shell thickness is 1,000 nm (melting time 4.83 μs). In case of polymer encapsulated paraffin nanoparticles, both k_{Wax} and k_{shell} are taken as 0.15 W/m·K, r_{Wax} and r_{shell} are 100 and 120 nm, respectively, Q_{Wax} is 232 J/g, and ρ_{Wax} is 0.7 g/cm^3. The melting equation can be written as:

$$\tau(T_s - T_m) = 2.56 \times 10^{-6} \ \ \mathrm{s{\cdot}K} \tag{33}$$

The melting time of polymer encapsulated paraffin is 25.6 μs when T_s-T_m= 0.1 K. Therefore, there is enough resident time at a flow rate of 210 ml/min (2 ms) for paraffin nanoparticles to melt.

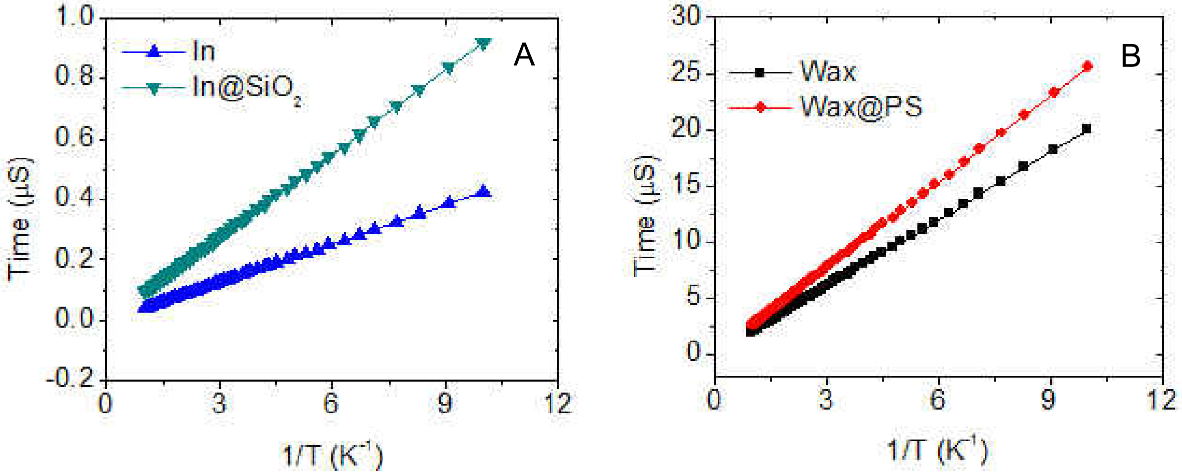

Figure 46. Melting times of 200 nm indium nanoparticles (A) and paraffin nanoparticles (B) with and without 20 nm shell.

4.9 Summary

This chapter investigates the heat transfer behavior of nano-PCMs suspensions. Adding such nano-PCMs into single phase fluid enhances the heat transfer properties of base fluids. The heat transfer coefficients of PAO and water increased for 28% and 75% by adding 9% and 10% mass ratio of encapsulated indium and wax. The dielectric properties of the base fluid have been preserved or enhanced for by the high dielectric shell. The fast melting of encapsulated nanoparticles allows complete utilization of latent heats of phase changes. The colloid suspension of encapsulated nanoparticles with its high heat transfer property can be used as novel coolants for direct immersion cooling of both low and high temperature devices. The core-shell structure is preserved after the heat loop test, the robust core-shell structure could be used many cycles for the heat transfer applications.

CHAPTER 5 CONTROLLING SUPERCOOLING

5.1 Introduction

Nano-PCMs have been used as heat transfer additives in single phase liquid to enhance heat capacity for heat transfer applications. The dielectric property of liquid is persevered by encapsulating nanoparticles with highly dielectric and high-melting point silica derived from TEOS.[83] One challenge is that the liquid to solid phase change occurs mainly through homogeneous nucleation with large degree of super-cooling,[89] which leads to limited enhancement of heat transfer performance, because the effective specific heat of fluid containing nano-PCMs is defined as $C_{\mathrm{eff}} = C_0 + H/\Delta T$, where H is the latent heat of fusion of nanoparticles, and ΔT is degree of super-cooling as shown in Figure 47. Instead of taking temperature difference between two maximums, ΔT is defined as the difference between the highest temperature in melting peak and the lowest temperature in solidifying peak. The super-cooling of microsized particles of phase change materials can be reduced by adding nucleating agent to reduce nucleation barrier,[101, 234-236] or controlling working conditions such as degree of overheating and cooling rates.[237-238] However there is no effective way to reduce super-cooling of metallic nanoparticles, which cannot be doped readily with non-molten impurities due to small size and lack of material with matching structure. Although previous studies have shown interface may play an important role in super-cooling of nanoparticles embedded in solid matrix,[239] it remains challenging of controlling interface property of shell to reduce supercooling of discrete phase change nanoparticles, which will be suspended in liquid for heat transfer. This section discussed a method to reduce supercooling of molten indium nanoparticles by encapsulating in high melting point semi-crystalline silica, which facilitates heterogeneous nucleation and prevents molten cores from leakage and agglomeration.

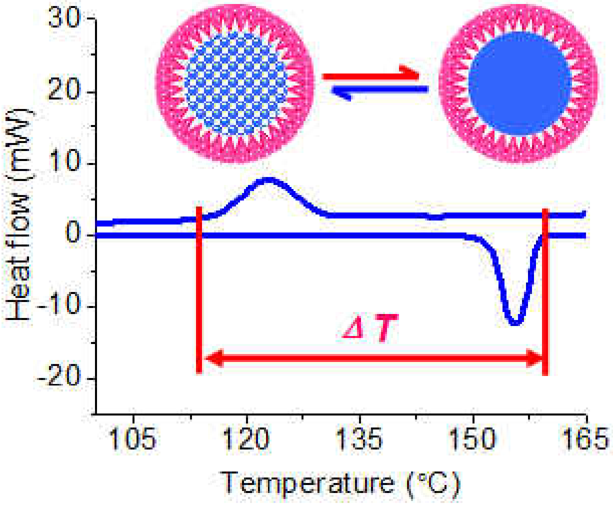

Figure 47. Supercooling of encapsulated phase change nanoparticles.

5.2 Experiments

Indium powders are directly boiled in PAO to make indium nanoparticles at 200°C. After removing nanoparticles from PAO by centrifuging and re-dispersing in ethanol or water, sol-gel or hydrolysis method is used to encapsulate nanoparticles in silica shells. Two types of silica precursors have been used for encapsulation. (1) TEOS is added in an ethanol suspension of indium nanoparticles, followed by drop-wise addition of ammonium hydroxide at 60°C under sonication. After reacting for 90 min, nanoparticles with silica shells are washed by ethanol and dried at 110°C. (2) A diluted solution of sodium silicate in water is added into nanoparticle suspension under sonication, followed by drop-wise addition of hydrochloric acid until pH reach 9 at 60°C. After reacting for 60 min, encapsulated nanoparticles are centrifuged at 5000 rpm to separate the encapsulated indium nanoparticles from liquid phase. The precipitations are washed by ethanol and dried at 110°C. Figure 48A is a TEM bright field image (accelerating voltage 100 kV) of indium nanoparticles encapsulated in TEOS-derived silica, where core diameters and shell thickness are 200 and 100 nm, respectively. Figure 48B is a TEM image of indium nanoparticles encapsulated in silica derived from sodium silicate (water glass), where core diameter and shell thickness are 200 and 50 nm, respectively.

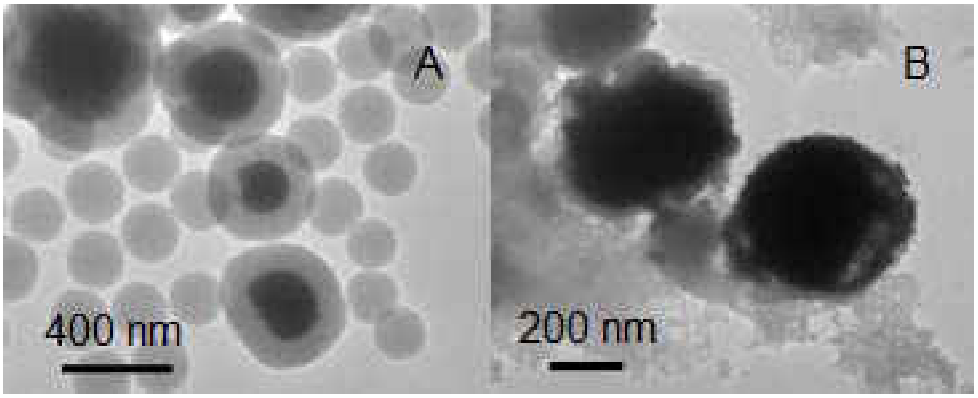

Figure 48. TEM images of indium nanoparticles encapsulated in silica derived from TEOS (A), and sodium silicate (B).

The water glass derived silica shell has a much high roughness than TEOS derived silica both on the inner and outer surface. The quantitative roughness of silica films derived from TEOS and sodium silicate are derived from AFM. Figure 49A and 49B insets show AFM images of silica films prepared by dipping a silicon substrate into the bickers of those two precursor solutions in ethanol and water, respectively. The preparation processes are the same as encapsulation of indium nanoparticles. The as prepared silica films are measured by a contact mode AFM with a scanning frequency of 1.0 Hz and scanning angle of 45º, the scanning range is 40 × 40 μm. The measured RMS (root-mean-square) roughness of silica from sodium silicate (127.4 nm) is larger than that from TEOS (22.4 nm), which can be directly observed from the morphologies of the obtained images.

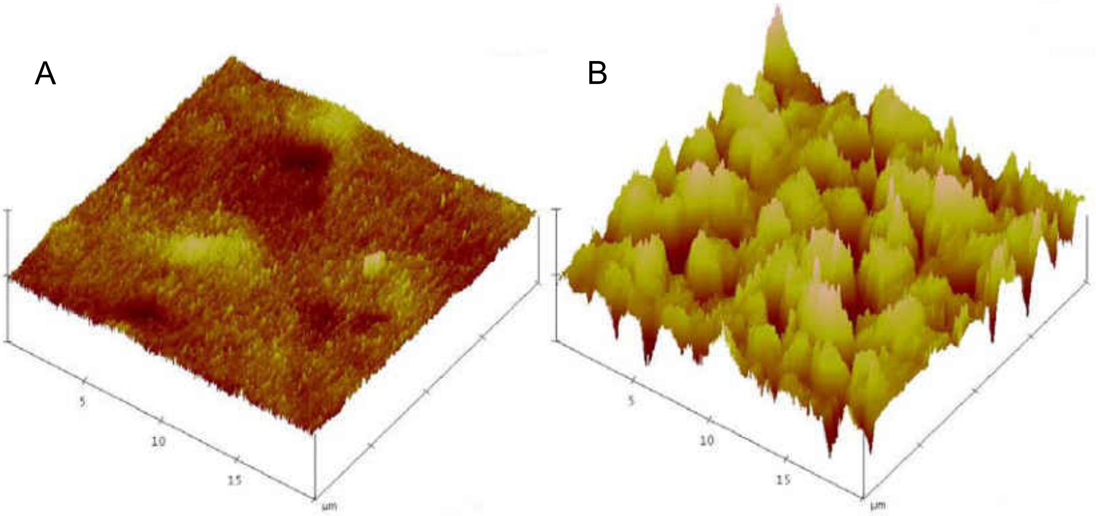

Figure 49. AFM images (40×40 μm^2 scanning range) of silica films obtained from TEOS (A) and sodium silicate (B).

AFM images indicate that silica derived from sodium silicate is rougher than that from TEOS, which is also confirmed by the facts that porosity measurement of those silica encapsulated nanoparticles and bare silica nanoparticles derived from the two precursors by nitrogen adsorption experiment. The relative system pressure (P/P_0) increases from 0.006 to 1 and decreases to the initial state, a computer controlled scale measuring the weight changes of the sample. The result shows that the porosity of silica encapsulated indium derived from sodium silicate (35 cm^3/g) is larger that of silica from TEOS (~3.5 cm^3/g) (Figure 50A); and porosity of pure silica powders from sodium silicate (350 cm^3/g, black square) is larger that of silica from TEOS (~35 cm^3/g, red dot) (Figure 50B).

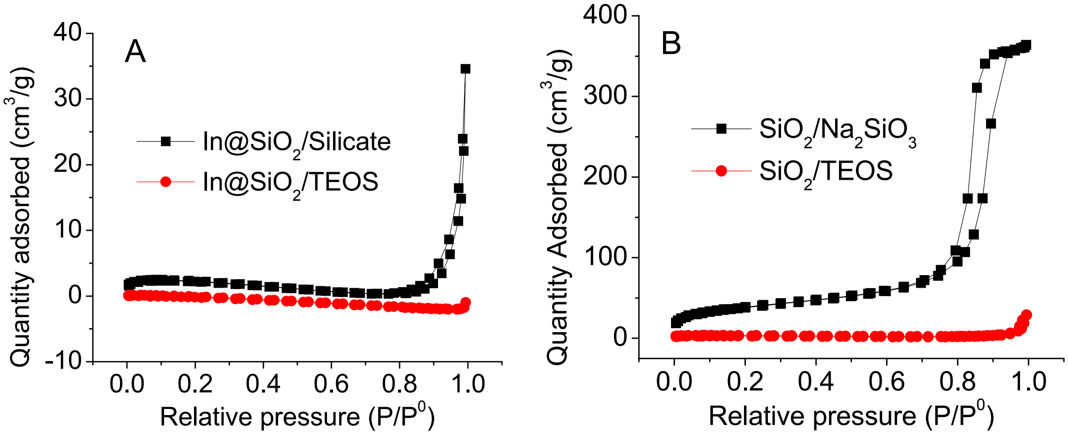

Figure 50. Nitrogen adsorptions of indium nanoparticles coated in TEOS derived silica (circle) and sodium silicate derived silica (square) (A); and according adsorptions on TEOS derived silica (circle) and sodium silicate derived silica (square) (B).

XRD analysis has been used to determine structures of silica formed around indium nanoparticles at a scanning speed of 2º/min and 2θ angle from 10 to 50º. Figure 51 shows that silica derived from TEOS is amorphous with a hump at 15-30°; and silica derived from sodium silicate has semi-crystallized structure with strong and sharp diffraction peaks at 32.3, 40.9 and 44.5º. The crystal structure of silica from sodium silicate is determined to be cristobalite by comparing its diffraction pattern with those in JADE database. Although its tetrahedral structure is stable at high temperature, a tetragonal form of cristobalite (Pearson symbol tP12) is stable at ambient pressure at temperature below 250°C. The existence of cristobalite phase at lower temperature is due to large activation energy related to phase transition from cristobalite to quartz, which needs to break and reform silica framework.

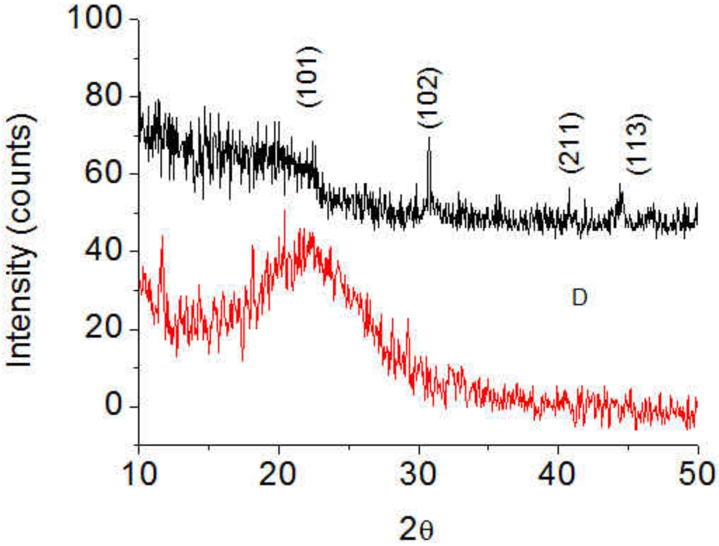

Figure 51. XRD spectra of silica derived from TEOS (red), and from sodium silicate (black).

5.3 Results and Discussions

DSC is used to measure thermal physical properties of uncoated nanoparticles, nanoparticles coated in TEOS-derived silica, and nanoparticles coated in sodium silicate derived silica. Figure 52 shows DSC curves collected at ramp rate of 10ºC/min, where all indium materials melt at 155.2ºC, but freeze are different temperature: raw powders and nanoparticles in TEOS-derived silica freeze at 131.2 and 123.6ºC, respectively; nanoparticles coated in sodium silicate derived silica freeze at 148.6ºC, and bulk indium freezes at 150.4ºC.

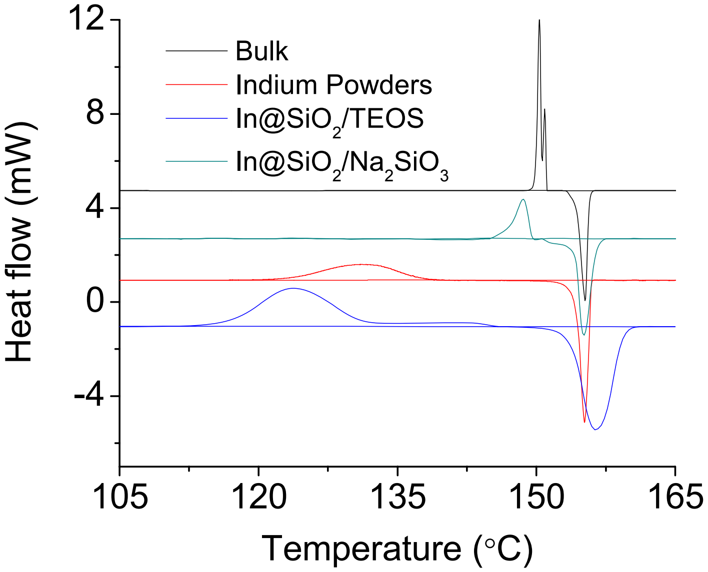

Figure 52. DSC curves of bulk indium (black), raw indium powders (red), indium nanoparticles in silica derived from TEOS (blue), and from sodium silicate (green).

The solidification of molten indium can occur through either homogeneous or heterogeneous nucleation depending whether there are nucleating sites. In the absence of gravity contribution, the critical Gibbs free energy of nucleation of molten indium (ΔG*) is given by

$$\Delta G^* = \frac{16\pi\gamma_{SL}^3 T_m^2}{3\Delta H^2 \Delta T^2} f(\theta) \tag{34}$$

where

$$f(\theta) = \frac{1}{4}(2+\cos\theta)(1-\cos\theta)^2 \tag{35}$$

$$\cos\theta = \frac{\gamma_{SL} - \gamma_{SM}}{\gamma_{SL}} \tag{36}$$

θ is the contact angle of molten indium on solid, ΔH is the latent heat of fusion of indium, γ_{SL} is the interfacial energy between solid and liquid interface. Assuming that interface between indium and silica is planar, the interfacial energy (γ_{SM}) can be derived from[240]

$$\gamma_{SM} = \gamma_S + \gamma_M - 2\sqrt{\gamma_S \gamma_M} = (\sqrt{\gamma_S} - \sqrt{\gamma_M})^2 \tag{37}$$

where γ_S and γ_M are surface energies of molten indium, and silica, respectively. Table 6 lists interfacial energies between molten indium and silica of different crystal face, where values of indium-cristobalite are smaller than those of indium-quartz. The contact angles and critical free energies of molten indium on different crystal faces of silica have been derived and shown in Table 6.[241-242] In the case of TEOS derived silica that is treated as a mixture of quartz with random orientation of crystal faces, molten indium does not wet and nucleation is homogeneous. In the case of silica derived from sodium silicate, molten indium has shown smaller contact angle, and energy barrier for nucleation is reduced, so as to reduce the supercooling effect.

Table 6. Interfacial energy between indium and silica surfaces.

Indium		Cristobalite			Quartz				
		(100)	(111)	(110)	(101)	(111)	(100)	(110)	(001)
γ_{AB} (J/m^2)	(001)	0.99928	0.63004	0.90591	0.94303	1.23057	1.13304	1.27002	1.29976
	(110)	0.90227	0.55352	0.81366	0.84886	1.12265	1.02958	1.16034	1.18877
	(100)	0.86508	0.52448	0.77836	0.8128	1.08112	0.98983	1.11811	1.14602
θ (°)	(001)	180	107	149	159	180	180	180	180
	(110)	128	89	117	121	180	147	180	180
	(100)	117	83	108	112	145	132	152	159
ΔG^* (10^{-15}J)	(001)	9.2	6.5	9.1	9.2	9.2	78.9	19.8	58.9
	(110)	12.5	6.8	11.3	11.8	13.9	57.06	13.4	42.6
	(100)	13.5	6.8	11.9	12.6	16.1	47.5	11.3	37.2

Supercooling is related to thermal history of sample such as overheating during melting process. In order to study effect of overheating, thermal scans are carried out on indium nanoparticles coated inside silica derived from TEOS and sodium silicate. Figure 53A are DSC curves collected when silica encapsulated indium nanoparticles derived from TEOS are heated at 20°C/min to the highest temperature and cooled down, where the highest temperatures are 170, 180, 190, 200 and 250°C with overheating of 14, 24, 34, 44 and 94°C, respectively; the relation between supercooling and overheating for both nanoparticles silica encapsulated indium nanoparticles derived from TEOS and sodium silicate are shown in Figure 53B. In the case of TEOS derived silica, supercooling increases from 33.7 to 37.4°C when overheating increases from 14 to 44°C, and remain the same when overheating increases to 94°C (red dot). In the case of sodium silicate derive silica, the overheating has no affection to the supercooling (Black square). The degree of supercooling (ΔT^-) depends on that of overheating (ΔT^+) as $\Delta T^-/\Delta T^+ = tg\theta$, where θ is contact angle of molten nanoparticle on silica. This is due to existence of small crystals over melting temperature which reduces supercooling of molten nanoparticles by facilitating nucleation. If nanoparticles are overheated to a large extent, the number of crystals decreases significantly, and homogeneous nucleation occurs during freezing due to lack of nucleating sites. From supercooling-overheating relations, the contact angles of molten indium nanoparticles on TEOS derived silica and sodium silicate derived silica are determined to be 6.8° and 0°, respectively. These values are much smaller than those (i.e., 145° and 83° on In(100) and SiO_2(111) interfaces) derived from Table 6, though the trends are the same (i.e., indium on sodium silicate derived silica has smaller contact angle). One possible reason for the large difference is that the data shown in Table 6 are derived from molten metal drops on single crystal surfaces, while those of nanoparticles are measured from nanoparticles with surrounding shells. The second possibility is that capillary interaction induced by stacking of small crystals (roughness) might have large effect on solidification.

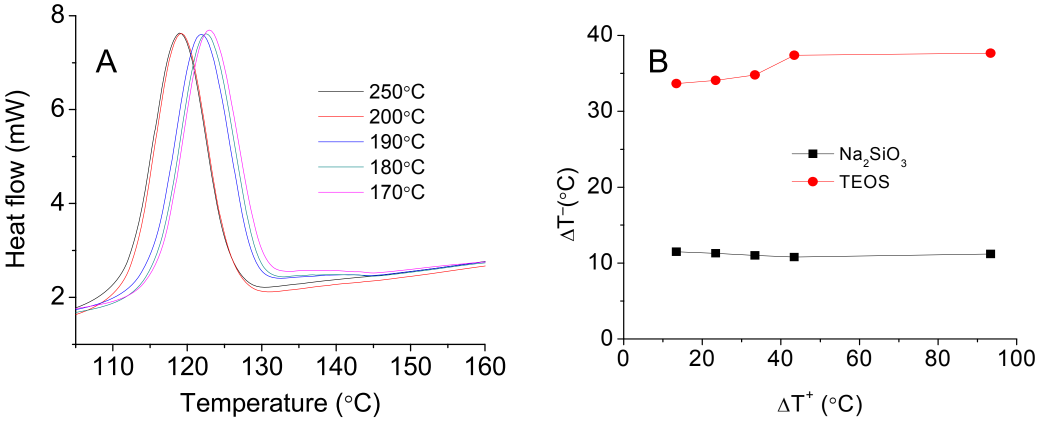

Figure 53. DSC curves of indium nanoparticles in silica derived from TEOS at different over-heating (A); overheating dependent supercooling for indium nanoparticles in silica derived from TEOS (red), and from sodium silicate (black) (B).

The heating and cooling rates affect supercooling of nanoparticles. In one experiment, encapsulated indium nanoparticles are heated to 165°C (10°C overheating) at rate of 20°C/min, and cooled at various rates; in another set, nanoparticles are heated at various rate and cool down at 20°C/min. Supercooling of nanoparticles in TEOS derived silica at 1, 5, 10, 20, and 40°C/min are 32, 33, 34, 36, and 41°C (Figure 54), respectively; those of nanoparticles in sodium silicate derived silica at 1, 5, 10, 20, and 40°C/min are 3.9, 6.1, 8.3, 10.2, and 14°C (not shown).

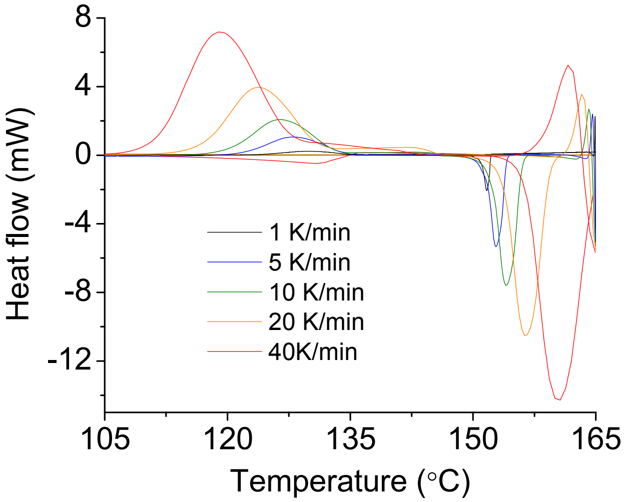

Figure 54. Supercooling as functions of heat and cooling rates of indium nanoparticles in TEOS derived silica.

The heating (cooling) rate dependent supercooling is shown in Figure 55, where slopes of supercooling versus heating (cooling) rate for both types of nanoparticles are almost linear, meaning thermal inertia of measurement chamber is a common origin, and the effective thermal inertia of chamber is determined to be 0.22 J/°C.

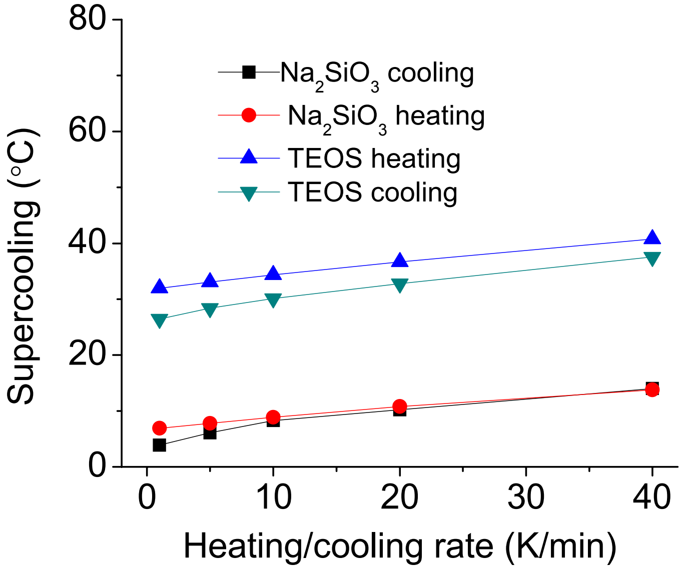

Figure 55. Supercooling as functions of heating and cooling rates for nanoparticles inside silica derived from TEOS (up triangle for heating and down triangle for cooling), and from sodium silicate (square for heating, and circle for cooling).

The degree of supercooling (ΔT) is normally defined as temperature difference between melting peak and cooling peak, but, when heat transfer efficiency in a loop is concerned, the degree of supercooling should be the difference between terminal temperatures of melting and cooling curves, where peak widths should be taken into considered. In DSC curve, peak width depends on heat transfer from heater to sample, thermal conductivity of atmosphere, and temperature ramp rate, and can be described by Gray's model based on energy conservation and Newton's law. The melting peak shape for a small amount of sample consists of two half-peaks, where the first has straight line slope and the second shows an exponential decay.[243] The width of melting peak can be derived as:

$$w = \frac{1}{2}\beta \cdot \Delta t = \frac{1}{2}\beta \cdot (t_1 + t_2) = \frac{1}{2}\beta R C_s [(\sqrt{1 + \frac{2\Delta H}{R C_s^2 \beta}} - 1) + \ln(100)] \tag{38}$$

where R is thermal resistance (0.3°C/mW), β is heating rate, Δt is melting time, t_1 and t_2 are rising and decaying times, respectively, ΔH and C_s are the energy required to melt material and the sample heat capacity, respectively. t_2 is defined as the time for heat flow fall below 1% of its maximum value. For 10 mg of silica encapsulated indium nanoparticles with 100 nm radius of indium core and 50 nm thickness of silica shell, ΔH and C_s are 166.2 mJ and 4.3 mJ/°C by taking densities of indium and silica as 7.3 and 2.2 g/cm^{-3}, respectively. Figure 56 shows heating rate dependent peak width of silica encapsulated indium nanoparticles after replacing all symbols with numbers, where peaks are wider when heating rates increase, nanoparticles in silica derived from TEOS and sodium silicate show similar trend, and the lines are simulated results according to equation (3). On the other hand, the cooling rate affects width of solidifying peak. Indium nanoparticles inside silica derived from TEOS and sodium silicate are heated to 165°C (10°C overheating) and cooled down to 50°C at various rates. Figure 56 also shows solidifying peaks are wider at higher cooling rates, and the dependence of peak width on cooling rate follows the similar rule as that of heating peaks. In addition, the widths of solidifying peaks are larger compared to melting peaks at the same heating/cooling rate, which is probably due to difference in thermal resistance at different temperatures, but peak areas at the same heating and cooling rates are the same, which means constant thermal mass of nanoparticles, and good encapsulation of silica shell.

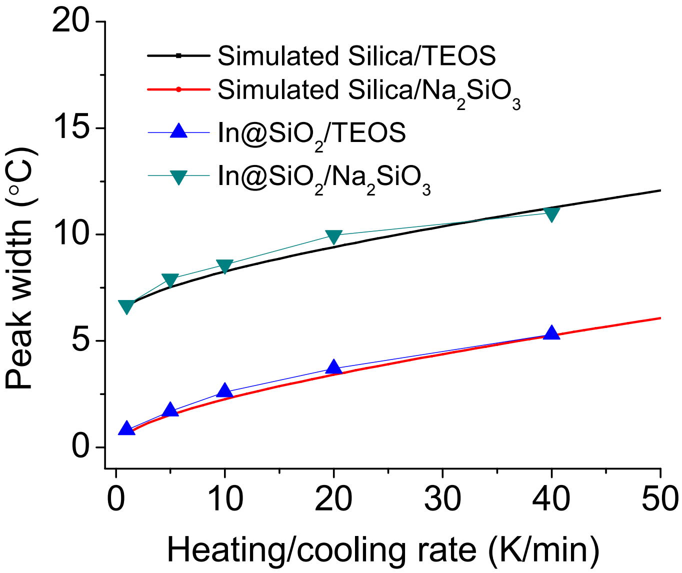

Figure 56. Half peak widths of melting peaks of silica encapsulated indium nanoparticles obtained from TEOS (down triangle) and Na_2SiO_3 (up triangle) as function of heating or cooling rates where solid lines are simulated results.

At last, indium nanoparticles with silica shells derived from sodium silicate are dispersed in PAO to test their heat transfer ability. Figure 57 shows a DSC curve measured at ramp rate of 20 °C/min, and cooling rate of 20°C/min, where the heating-cooling cycles have been repeated between 150 and 165°C for 100 times. The repeatable DSC curves indicate that silica derived from sodium silicate is sufficiently strong to prevent molten nanoparticles from leakage or agglomeration despite their porous structures. The effective specific heat of indium nanoparticles in sodium silicate derived silica shell is 6.8 J/gK by considering supercooling and peak width; in comparison, the effective specific heat of indium nanoparticles encapsulated in TEOS derived silica (3.5 J/gK), and the specific heat of PAO (2.7 J/gK) are much smaller.

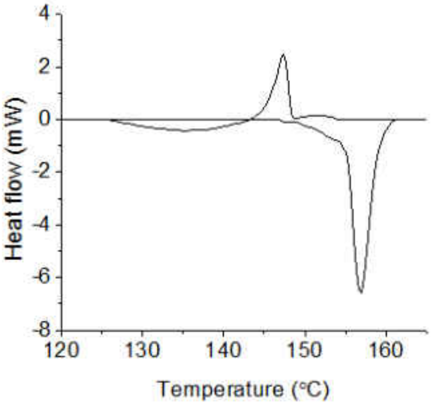

Figure 57. DSC curve of indium nanoparticles coated in silica derived from sodium silicate after 100 times heating-cooling cycles in PAO.

5.4 Summary

In summary, supercooling of indium nanoparticles can be dramatically reduced by heterogeneous nucleation on silica derived from sodium silicate. Both surface roughness and crystal structure of silica can lower threshold of nucleation, and degree of super-cooling. The effects of overheating, heating and cooling rates are understood from heterogeneous nucleation, and thermal inertia of instrument. By reducing super-cooling of indium nanoparticles, the effective heat transfer coefficient of nanoparticle suspension is enhanced.

CHAPTER 6 CONTROLLING THERMAL RUNAWAY

6.1 Introduction

This chapter describes a new way to control temperatures of heterogeneous exothermic reactions such as heterogeneous catalytic reaction and polymerization by using encapsulated nanoparticles of phase change materials as thermally-functional additives. Silica-encapsulated indium nanoparticles and silica encapsulated paraffin nanoparticles are used to absorb heat released in catalytic reaction, and to mitigate gel effect of polymerization, respectively. The local hot spots that are induced by nonhomogenous catalyst packing, reactant concentration fluctuation, and abrupt change of polymerization rate lead to solid to liquid phase change of nanoparticle cores so as to avoid thermal runaway by converting energies from exothermic reations to latent heat of fusion. By quenching local hot spots at initial stage, reaction rates do not rise significantly because the thermal energy produced in reaction is isothermally removed. Nanoparticles of phase change materials will open a new dimension for thermal management of exothermic reactions to quench local hot spots, prevent thermal runaway of reaction, and change product distribution.

The thermal runaway of an exothermic chemical reaction refers to a situation, in which increases in temperature will change reaction condition in such a way that temperature increases further.[244-246] The thermal runaway affects the yield, selectivity and safety of many reactions including heterogeneous catalytic reaction, free radical polymerization, and electrochemical energy conversion, etc. The thermal runaway of heterogeneous catalytic reactions can cause side reactions, catalyst deactivation, and loss in productivity or selectivity, and lead to explosion if released reaction heat cannot be removed quickly.[247-251] A similar effect in polymerization is also called auto-acceleration or gel effect, in which positive feedback will speed up polymerization, and result in heat accumulation due to increased viscosity.[252-253] In the case of electrochemical reaction, thermal runaway is the major cause of battery explosion due to temperature rise. A common feature in these exothermic reaction systems is the existence of hot spots induced by non-uniformities of catalyst packing, reactant concentration, as well as heating and cooling effects.[254-256]

The temperature of heterogeneous reactions is often controlled by proportional-integral-derivative (PID) unit, where temperature around or inside a reactor will be monitored continuously. Once the measured temperature is higher than the designed value, cold air or liquid will be circulated to remove extra heat, or reactant feeding rate will be reduced to limit reaction heat. However, the performance of temperature control depends on the locations and sizes of thermocouples, and heating/cooling units, which cannot be distributed uniformly in reactor or made sufficiently small to detect or quench microsize hot spots. For heterogeneous catalytic reactions, the reactions take place inside micro-pores, where the temperatures are higher than those around reactor. It takes some time for reaction heat transferring to thermocouple from hot spots to activate control units. Such response delay causes temperature increase, and leads to ineffectiveness in temperature control.[257-259] The thermal runaways of polymerizations cannot be controlled readily using PID units as well, because high viscosity products prevent efficient heat transfer from hot spots. A small quantity of inhibitor is often added into reactor at early stage of runaway, or polymerization is carried out in water to absorb the reaction heat.

Single phase substances in either liquid or solid phases have small heat capacity, and cannot take much thermal energy. As a result, significant temperature rises occur even if small amounts of thermal energy are absorbed by solids or liquids. An effective way to enhance the heat capacity of a pure substance is to add materials that undergo phase change at certain temperature where the latent heat of fusion will contribute significantly to the heat capacity of mixture.[83] Dissipating heat into PCM results in a nearly isothermal heat sink during melting and the operating temperature can be adjusted by using different PCMs so that melting does not occur until needed. A variety of PCM materials such as paraffin waxes, inorganic salt hydrates, or metal eutectic alloys have been used to maintain desired temperature and reduce the fluctuation of temperature.[260] However, bulk PCMs are not very useful for many applications such as temperature controls of heterogeneous chemical reactors for several reasons. (1) In order to exploit latent heats of fusion for heat absorbing, PCMs should be sufficiently small so that it melts rapidly. It has been shown that if the radius of PCM is reduced by 10 times, the time required for complete melting reduces by 100 times.[103] (2) To work in a heterogeneous reactor, the PCM should be encapsulated inside a shell with good sealing and stability to prevent leakage or agglomerate. (3) PCM should form homogeneous mixture with reactants or catalysts in order to quench local microsized hot spots.

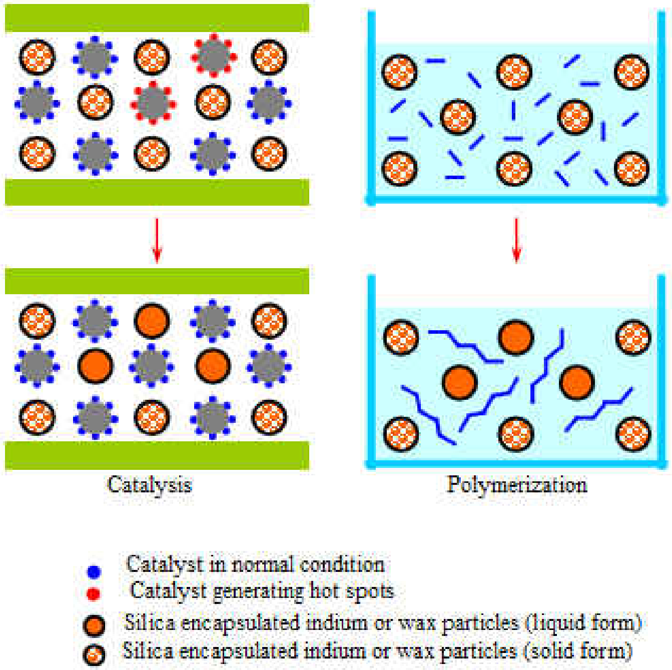

Figure 58. Controlling thermal runaway of heterogeneous catalytic reaction (L) and polymerization (R) using encapsulated nanoparticles of phase change materials.

Instead of using inert solid (sand) to support catalytic species or liquid (water) to reduce gel effect of polymerization reaction, the advent of nanostructured materials provides a new approach for thermal managements of exothermic reactions. This chapter describes the use of a new nanostructured material, encapsulated phase change nanoparticles (nano-PCM), to control the thermal runaway of catalytic reactions and polymerizations, where nano-PCMs can absorb reaction heat, and change phases from solid to liquid. The core materials are metal nanoparticles or paraffin wax nanoparticles, which change phases at suitable temperature. The non-melting shells are made of silica or polymer, and are stable at operating conditions to prevent the leakage or oxidization of core material.[261] Due to their small sizes, inert surfaces, and large heat-absorbing capabilities, nano-PCMs can be mixed homogeneously with solid catalysts or monomers to quench local hot spots before accumulation of heat energy at a large scale, thus breaking the positive feedback loop between the reaction rate and temperature, and postponing onset of thermal runaway by absorbing reaction heat (Figure 61). Nano-PCMs do not increase the size of catalytic reactor, because active species can be supported at shells of nano-PCMs; in addition, polymers can be dissolved in its good solvent, and separated from nano-PCM after polymerization. Two highly exothermic reactions, platinum catalyzed methanol oxidation, and polymerization of methyle methacrylate (MMA), have been used as examples to prove the generality of this approach.[262-263]

6.2 Experimental Procedures

All chemicals are obtained from Aldrich and used as received such as tetraethoxysilane, ethanol, methanol, tetrahydrofuran, and polyethylene-block-polyethylene glycol at molecular weight of 1400. Poly-alpha-olefin with boiling point of 250°C is from Air Force Research Laboratory. Indium, methylmethacrylate (MMA), azoisobutyronitrile (AIBN), toluene and acetic acid are from Alfa Aesar. Polyethylene wax (POLYWAX 1000, melting temperature of 110°C) is provided by Baker Hughes.

6.2.1 Encapsulated indium nanoparticles

Metallic phase change nanoparticles are made by directly boiling metal powders. 1.0 g of indium powders (-100 mesh) are boiling in poly-alpha-olefin (PAO) at ~200°C at a stirring rate of 800 rpm for 12 hrs.[83] After cooling down to room temperature, nanoparticles are separated by centrifugation, washed with ethanol for three times, and dried in nitrogen. Sol-gel method is used to encapsulate nanoparticles with silica after removing nanoparticles by centrifuging and washing by ethanol. The nanoparticles are encapsulated in silica by decomposing tetraethoxysilane (TEOS) at 70°C as below. 0.1 g of nanoparticles is dispersed into ethanol and sonicated for 10 min, 1 ml TEOS is added into the solution and sonicated for 1 hr, which is followed by adding ammonia hydroxide as catalyst for formation of silica. The thickness of silica shell is controlled by changing TEOS concentration, and TEOS versus nanoparticle ratio.

6.2.2 Encapsulated paraffin nanoparticles

Silica encapsulated polyethylene (paraffin wax) nanoparticles are made as following. 1.0 g of polyethylene, 1.0 g of TEOS and 0.25 g polyethylene-block-polyethylene glycol are dissolved in 4 ml of toluene at 100°C. 50 ml of water is added in 250 ml of three-neck flask equipped with mechanic stirrer, and heated to 95°C, and toluene solution is poured into three-neck flask, stir vigorously for 60 min to form white emulsion. 0.4 g of acetic acid solution (10 wt%) is added into above mixture, and cool down to 55°C and stir at 300 rpm for 3 hrs to ensure complete hydrolysis and condensation of TEOS. The product is separated by centrifuging at 8500 rpm for 10 min and wash with water for three times, dry in oven at 60°C for 24 hrs.

6.3 Experimental Design

6.3.1 Catalytic reaction

Supported Pt/SiO_2 catalyst is made by impregnating SiO_2 (200 m^2/g) with an aqueous solution of tetraammineplatinum nitrate at 25°C for 4 hrs. The impregnated support is dried in ambient air at 125°C and heated at 500°C for 4 hrs. The obtained precursor is reduced in H_2/He (10% v/v) mixture at 500°C for 2 hrs. 10 mg of the catalyst is then mixed with 1 g of silica encapsulated indium nanoparticles, and the mixture is loaded into a quartz reactor to form a 1 cm column. A nickel-chromium thermocouple of 1 mm diameter is inserted in the reactor to measure the temperature of catalyst. Before the catalysis experiments, the reactor is heated at 120°C in a flow of helium gas for 0.5 h. A mixture gas of He, O_2, and methanol (87/9/4, p/p/p) at 100 ml/min is switched into the reactor. Two on-line chromatograph systems are used to analyze products: a Porapak Q packed column with thermal conductivity detector for carbon dioxide; a methyl-silicone capillary column with flame ionization detector for organic products.

6.3.2 Polymerization reaction

Methylmethacrylate monomer (MMA) is polymerized under isothermal batch condition in a 10 ml glass bottle at 80ºC. The reaction is initiated by adding 0.1 g of azoisobutyronitrile (AIBN) into 2 ml of MMA monomer. Different amounts of silica encapsulated paraffin nanoparticles have been added to prevent thermal runaway. A thermocouple is inserted into the solution, and the reaction temperature is recorded by using an Agilent (34970A) data acquisition unit. The molecular weight of polymer product is measured by gel permeation chromatography (GPC) in tetrahydrofuran (THF).

6.4 Results and Discussions

6.4.1. Structure and composition of silica encapsulated indium nanoparticles

This direct boiling and sol-gel method can produce nano-PCMs of indium with core diameter of ~150 nm and shell thickness of 10-20 nm as shown in Figure 59A. High resolution TEM image shows crystallized core and amorphous shell (Figure 59B). The composition of nanoparticles has been confirmed by EDX analysis (Figure 59C), where the signals of indium and silicon can be identified clearly. Figure 59D shows size distribution of the encapsulated indium nanoparticles, where the mean diameter of nanoparticles is determined as 150 nm by using dynamic light scattering. The core diameter can be controlled in the range from 10 to 200 nm by changing reaction conditions including reaction time and precursor concentration. The thickness of silica shell has been controlled in a range of 10 and 30 nm by changing molar ratio of nanoparticle and TEOS.

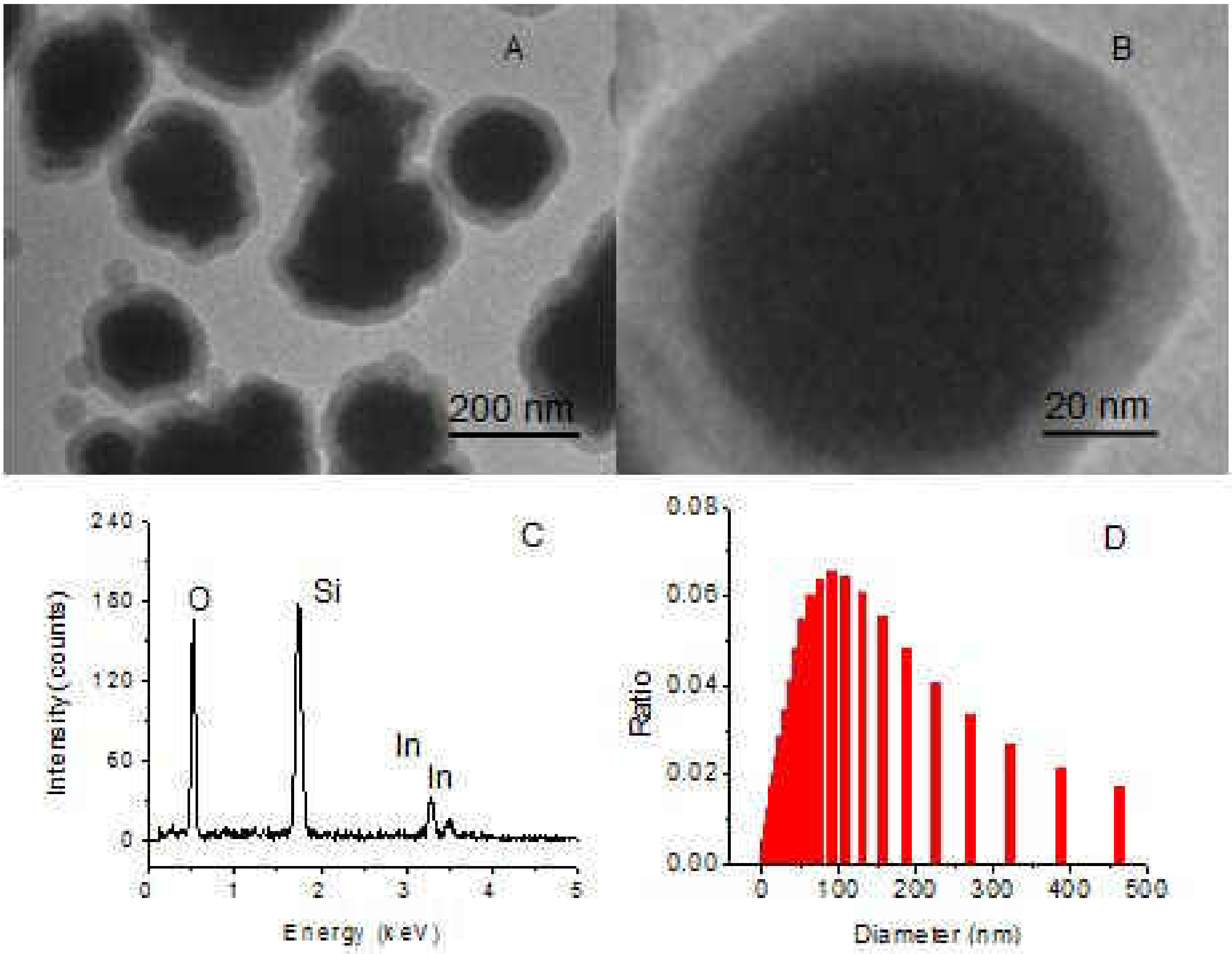

Figure 59. TEM image (A), high-resolution TEM image (B), EDX result (C), and size distribution (D) of the encapsulated indium nanoparticles.

6.4.2. Structure and composition of encapsulated paraffin nanoparticles

Interfacial poly-condensation method has been used to produce silica encapsulated polyethylene nanoparticles. Figure 60A shows a TEM image, where dark polyethylene core and light silica shell can be seen clearly. The core diameter and shell thickness are approximately 1000, and 500 nm, respectively. The mean size of particles derived from DLS is about 2 μm (Figure 60B). Figure 60C shows Fourier transform infrared spectroscopy (FT-IR) spectra of polyethylene and encapsulated polyethylene nanoparticles, where the characteristic peaks of polyethylene can be observed (Figure 60C red). The two absorption peaks at 2916 and 2848 cm^{-1} are characteristic peaks of aliphatic C-H stretching vibration; the peak at 1464 cm^{-1} is assigned to C-H bending vibration; the peak at 721 cm^{-1} is associated with in-plane rocking vibration of CH_2 group. The absorption peaks at 941 and 3430 cm^{-1} are assigned to the stretching of hydroxyl group in Si-OH and residual water and 1111 cm^{-1} is assigned to the asymmetrical stretching of siloxane bond Si-O-Si. The thermal property of nanoparticles has been studied by DSC. Figure 60D shows DSC curves of polyethylene, and silica encapsulated polyethylene nanoparticles. The melting and solidifying points of polyethylene are at 110 and 100 ºC, respectively. The latent heats of fusion of paraffin and silica encapsulated paraffin nanoparticles are derived from DSC to be 200, and 160 J/g, respectively, from which the ratio of PCM in core-shell structure is determined to be approximately 80 wt%.

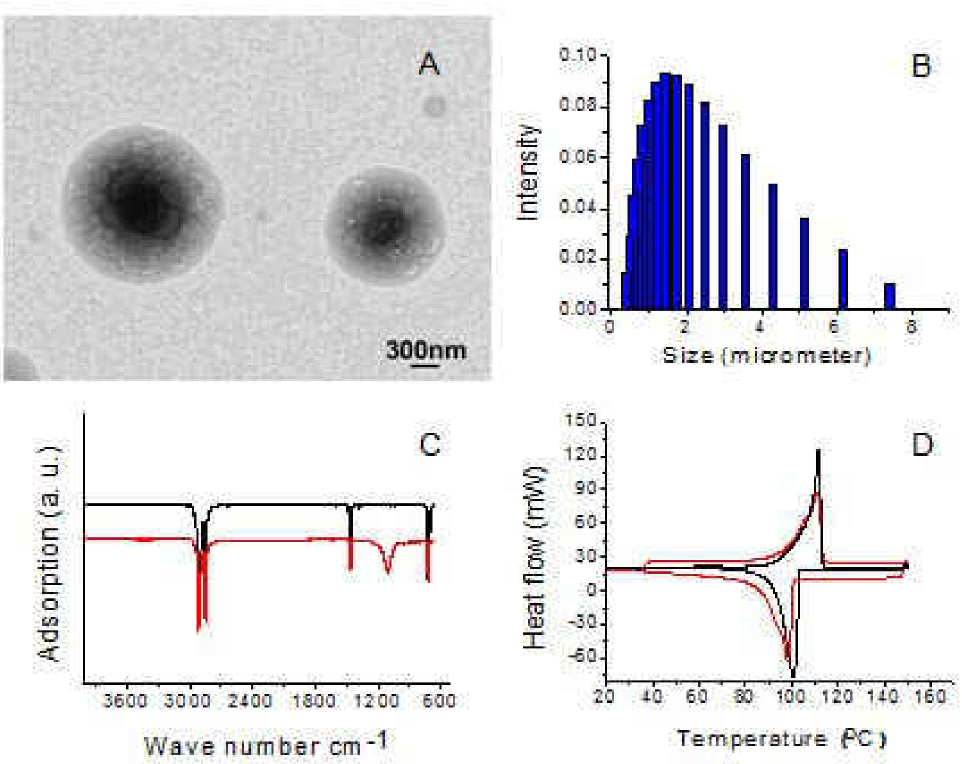

Figure 60. TEM image (A), size distribution (B), FT-IR spectra, and DSC curve (red curve) of silica encapsulated polyethylene wax particles. DSC curve of polyethylene is shown as black curve in (D).

6.4.3. Preventing thermal runaway of catalytic reaction

Encapsulated indium nanoparticles are used to prevent thermal runaway of methanol oxidation on supported platinum catalyst. Figure 61 shows the relation between measured temperature and time after feeding methanol in vapor form, where the temperature control unit is set at 120°C. In the control experiment with 10 mg of catalyst and 1 g silica as dilutor, the measured temperature quickly rises from 120 to 320°C, and remains constant at 320°C due to strong heat liberation of reaction.

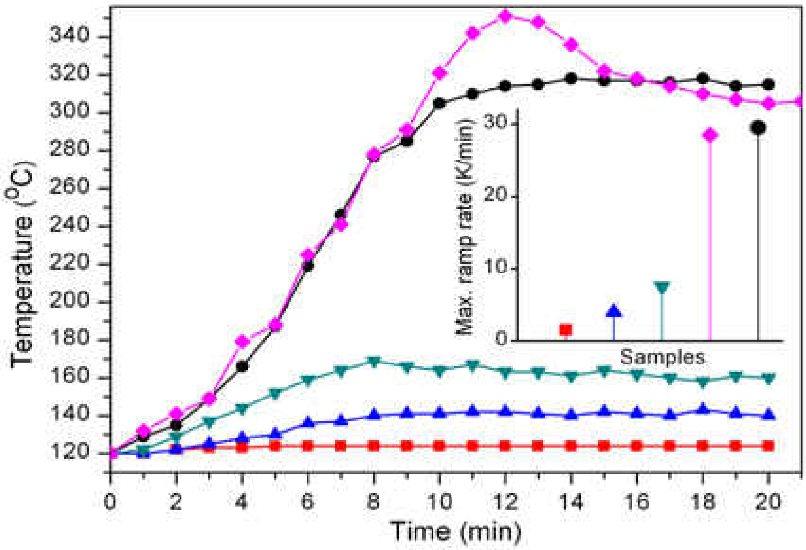

Figure 61. Reaction time dependent temperature at different amount of nano-PCM and Pt/SiO$_2$ catalyst.

** 0 g of nano-PCM and 10 mg of catalyst diluted in 1g of SiO$_2$ (circle) or 1g SiC (diamond); 1 g of nano-PCM and 50 mg of catalyst (down triangle), 1 g of nano-PCM and 30 mg of catalyst (up-triangle), 1 g of nano-PCM and 1 mg of catalyst (square). The ramp rates at different amount of nano-PCM and catalyst (inset).

From the distribution of products as listed in Table 7, CO$_2$ is the main product, suggesting burning of methanol. Instead of using low thermal conductivity silica (1.3 W/m·K) as dilutor in catalyst bed, silicon carbide with high thermal conductivity (~360 W/m·K) to conduct reaction heat has also been used in the control experiment. However, for the strong exothermal reaction of methanol oxidation catalyzed by Pt/SiO$_2$, silicon carbide cannot eliminate thermal runaway, and the highest and steady temperatures reach 351°C and 310°C respectively. When 10 mg of catalyst and 1 g of nano-PCM are packed in the reactor, the reaction temperature is constant at ~120°C, meaning effective control of thermal runaway. Although the conversion is as low as 0.6

% because of the low reaction temperature, the trend of methanol burning at initial stage of reaction is efficiently controlled. The large latent heat of indium (28.52 J/g·K) takes heat from hot spots of reaction. The ramp rate of temperature at the initial stage of runaway is dependent on the relative mass ratio of nano-PCMs to Pt/SiO_2 catalyst as shown in Figure 64 inset. The highest ramp rate (29.5ºC/min) is achieved in the cases when there are no nano-PCMs (silica or silicon carbide as dilutor). The ramp rate decreases as the relative amounts of nano-PCMs increases. In the case of 30 mg catalyst and 1g nano-PCMs, the temperature rises to 140ºC. Increasing the catalyst to 50 mg and keeping PCMs at 1 g leads to a further temperature increases to 165ºC, which is higher than the melting temperature of indium (156ºC), and the temperature of catalyst bed can still be controlled. It implies that local hot spots can melt encapsulated indium nanoparticles due to their high temperature, and the phase change of indium nanoparticles adsorbs reaction heat, quenches local hot spots, and prevents thermal runaway of reaction.

Table 7. Conversion and selectivity of methanol oxidation on Pt/SiO_2 catalyst with different amount of silica encapsulated indium nanoparticles.

Samples *	Steady temp. (ºC)	Conv. (%)	Selectivity (%) *				
			HCHO	MF	CO_2	DMM	DMOH
10mg Pt/SiO_2 1g SiO_2	320	98.2	–	12.1	83.2	4.7	–
10mg Pt/SiO_2 1g SiC	310	99.3	–	11.2	87.7	1.1	–
10mg Pt/SiO_2 1g In@SiO_2	120	0.6	97.3	2.6	–	–	0.1
30mg Pt/SiO_2 1g In@SiO_2	140	5.5	75.2	21.3	3.1	0.2	0.2
50mg Pt/SiO_2 1g In@SiO_2	165	32.5	32.5	52.3	14.8	0.3	0.1

* In@SiO_2 denotes silica encapsulated indium PCMs; MF, DMM and DMOH mean methyl formate, dimethoxy methane and methoxymethanol.

Controlling thermal runaway affects the distribution of the product as shown in Table 7. The conversion of methanol on 10 mg catalyst and 1 g silica is highest (98.2%), but the major product is carbon dioxide. Adding nano-PCM reduces conversion yield, and amount of carbon dioxide. At the same load of nano-PCMs (1 g), the conversion yield increases from 0.6 to 32.5% as catalyst increases from 10 to 50 mg. The selectivity to HCHO decreases from 97.3 to 32.5%; and selectivity to methyl formate increases from 2.6 to 52.3%. Due to suppression of runaway, the selectivity to carbon dioxide in methanol oxidation is reduced, and the selectivity to partial oxidation products increases. The selectivity to methyl formate (MF) increases to 52.3% when the amount of catalyst is 50 mg. In the mild condition, the reaction rate is decreased, but the yield of methyl formate is increased. Therefore, nano-PCMs can be used to control thermal runaway and promote the yield of products of strong exothermic reaction.

6.4.4. Preventing thermal runaway of polymerization

The polymerization of methyl methacrylate (MMA) monomer is a strong exothermic reaction. DSC has been used as isothermal calorimeter to determine adiabatic thermal energy release from polymerization, which starts at 80°C, and reaches maximum at 125ºC as shown in Figure 62 (red curve). The heat-releasing peak corresponds to reaction enthalpy of -1717.8 mJ for 3 mg of MMA. The melting of polyethylene is endothermic with peak temperature of 110.3ºC, and peak area of 202.1 J/g (black curve). When 2.5 mg of silica encapsulated polyethylene nanoparticles containing 2 mg polyethylene is added into 2 mg MMA, the exothermic heat decreases to 460.3 mJ (green curve). Doubling the amount of encapsulated polyethylene nanoparticles to 5 mg while keeping amount of MMA (2 mg) leads to reduction of heat to 94.2 mJ (blue curve). Adding silica encapsulated polyethylene nanoparticles in polymerization leads to reduction of exothermic heat due to suppression of local hot spots. When the measured temperature is between 80 to 105ºC, heat released from the polymerization is less than the fusion enthalpy of polyethylene, and a small endothermic peak appears in green and blue curves. (The polyethylene melts due to hot spots, even if the measured temperature is lower than its melting point). When the measured temperature is increased, the polymerization rate is increased, and the released heat is absorbed by melting polyethylene. The excessive heat gives a small exothermic peak.

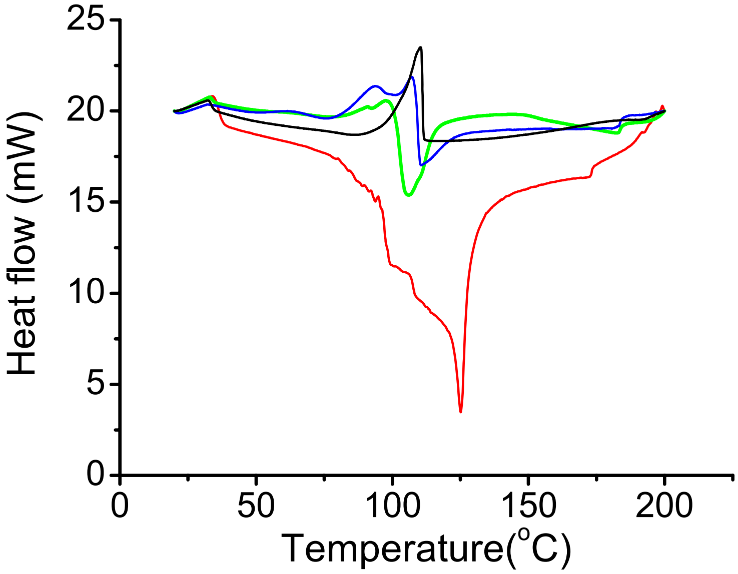

Figure 62. DSC curves of polyethylene (black); adiabatic polymerization of 2 mg MMA (red), 2 mg MMA with 2.5 mg (green) or 5.0 mg (blue) silica encapsulated polyethylene nanoparticles.

In order to further confirm the suppression of thermal runaway of polymerization, encapsulated polyethylene nanoparticles are added into monomer of methylmethacrylate. The temperature is controlled at 80ºC in a water bath, and a thermocouple is inserted into monomer to record reaction temperature. Figure 63 shows the magnitudes of measured temperature as functions of time. In the absence of phase change nanoparticles, when polymerization is initiated, the measured temperature increases to 100ºC, and the temperature increases abruptly to 140ºC after 600 sec, which is presumably because of viscosity increase and thermal runaway. When 0.63 g of silica encapsulated polyethylene nanoparticles is added into monomer, the temperature increases to 120ºC after 700 s. Adding 1.25 g of encapsulated polyethylene nanoparticles leads to smooth reaction, where the highest temperature measured by thermocouple is 110ºC, which is close to the melting point of polyethylene.

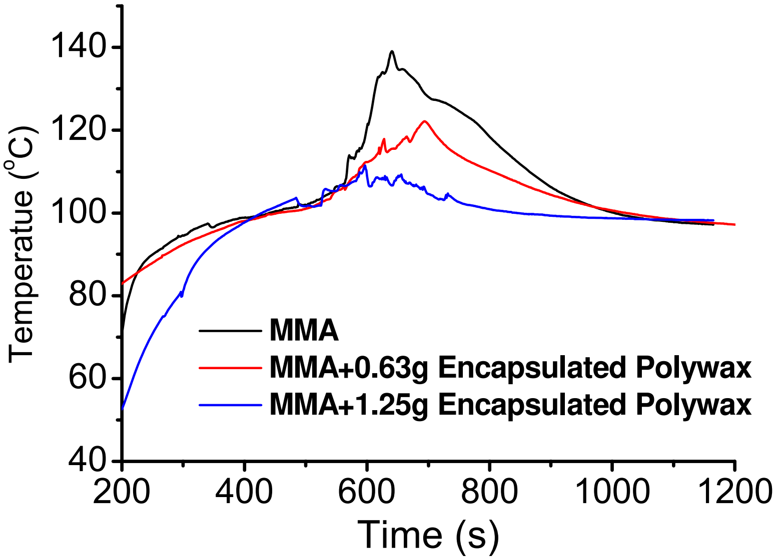

Figure 63. The temperature rises of 1 g MMA (black), 1 g MMA with 0.63 g (red) or 1.25 g (blue) silica encapsulated polyethylene nanoparticles when temperature is maintained at 80ºC.

The molecular weights of generated PMMAs are derived from gel permeation chromatography. The permeation time of PMMA made without silica encapsulated polyethylene nanoparticles is 7.92 min, corresponding to molecular weight of 25,000; the permeation time of PMMA made with encapsulated polyethylene particles is 8.25 min, corresponding to molecular weight 15,800 (Figure 64). This is understandable that polymer made at high polymerization temperature normally has higher molecular weight.

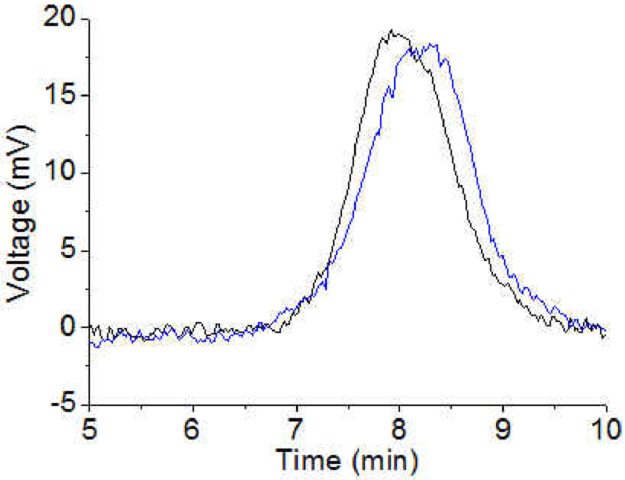

Figure 64. The molecular weights of PMMA with (black) and without (blue) silica encapsulated polyethylene nanoparticles from gel permeation chromatography.

Figure 65A, 65B and 65C show the morphologies of polymer produced in the three-polymerization reactions. In the absence of polyethylene nanoparticles, polymerization is more acute, which generates bubbles in polymethyl methacrylate (PMMA); adding encapsulated polyethylene particles makes polymerization stable.

Figure 65. Morphologies of products from three reactions, where the images from left to right correspond to no nanoparticles (A), 0.63 (B) and 1.25 g (C) nanoparticles, respectively.

6.4.5. Thermophysical characteristics of encapsulated phase change nanoparticles

The effect of nano-PCM on preventing thermal runaway can be derived by comparing heat capacities of silica particles and silica encapsulated indium nanoparticles. The specific heat of silica is 0.7 J/g·K, and the latent heat of indium is 28.52 J/g. If the melting range of indium nanoparticles is taken as 10°C (151 to 161°C), the heat that can be taken by 1 g of indium nanoparticles (ignore contribution of shell) will be four times the heat that can be taken by 1 g of silica in the same temperature range. The heat capacity of 1 g of indium nanoparticles will be ~80 times higher than that of catalyst, meaning temperature rise of catalyst due to hot spots can be effectively lowered to avoid heat accumulation.

In order to exploit the latent heat of fusion, nano-PCMs have to melt rapidly during reaction. The heat absorption of nanoparticles depends on characteristics of heat conduction in nanoparticles, which in turn depends upon particle size and material properties. The heat transfer from environment into particles is determined by the difference between environment temperature and surface temperature of particles and can be numerically calculated using equation (22). The sizes of core and shell of indium nanoparticles here r_{In} and r_{SiO2} are 100 and 120 nm, respectively, Q_{In} is 28.52 J/g, ρ_{In} is 7.3 g/cm^3. Replace all symbols with numbers, and let r equal to 0 nm, the equation (23) is rewritten as:

$$\tau(T_s - T_m) = 0.92\times10^{-7}\ \text{s·K} \tag{39}$$

Figure 66A shows the melting time as the function of temperature difference between surface temperature (hot spot) and melting temperature for indium nanoparticles. The melting time τ is 0.92 μs when T_s-T_m= 0.1 K. In case of silica encapsulated polyethylene nanoparticles, k_{Wax} and

k_{shell} are taken as 0.15 and 1.3 W/m·K, r_{Wax} and r_{shell} are 500 nm and 1 μm, respectively, Q_{Wax} is 232 J/g, and ρ_{Wax} is 0.7 g/cm^3. The melting equation can be written as:

$$\tau(T_s - T_m) = 1.49 \times 10^{-5} \quad \text{s·K} \tag{40}$$

Figure 66B shows the melting time as a function of temperature difference for polyethylene nanoparticles. The melting time of silica encapsulated paraffin is 148.7 μs when T_s-T_m= 0.1 K. Thus, the phase change nanoparticles can response rapidly to local hot spots to remove thermal energy.

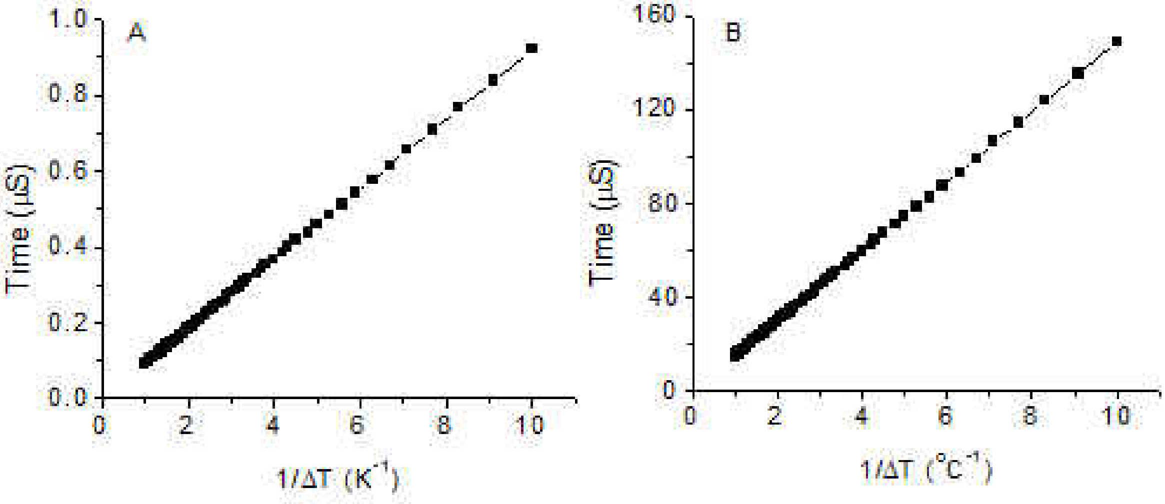

Figure 66. Calculated melting times of 200 nm indium nanoparticles with 40 nm silica shell (A); melting times of 1 μm paraffin nanoparticles with 500 nm silica shell (B).

6.4.6. Kinetics of nano-PCM in prevention of thermal runaway

The contribution of phase change materials to prevent thermal runaway is studied for a general reaction $aA + bB \leftrightarrow cC$, in which heat flow can be expressed as[264]

$$\frac{dH}{dt} = \Delta H \cdot k[A_{0,A} - \frac{a}{c} \cdot \frac{\int_0^t (\frac{dH}{dt} + \frac{dH_{pcm}}{dt})}{\Delta H}]^m \cdot [A_{0,B} - \frac{b}{c} \cdot \frac{\int_0^t (\frac{dH}{dt} + \frac{dH_{pcm}}{dt})}{\Delta H}]^n \tag{41}$$

where dH/dt is the instant heat flow of reaction at a certain time, $\int_0^t dH/dt$ is the corresponding accumulated heat, ΔH is the total heat generation from the reaction, k is the rate constant, $C_{0,A}$ and $C_{0,B}$ are the initial concentrations of reactants, a, b, and c are stoichiometric constants, m, and n are orders of the reaction, and H_{pcm} is the fusion enthalpy of phase change nanoparticles. For methanol oxidation, m is 1 and n is 0, and equation (41) is thus simplified to:

$$\frac{dH}{dt} = \Delta H \cdot k[C_0 - \frac{\int_0^t \frac{dH}{dt} + \frac{dH_{pcm}}{dt}}{\Delta H}] \tag{42}$$

Solving the differential equation (42) yields:

$$\frac{dH}{dt} = \Delta H \cdot k \cdot C_0[1-\exp(-kt)] \tag{43}$$

Integrating equation (43) gives

$$H = \Delta H \cdot C_0[kt + \exp(-kt)] \tag{44}$$

The released heat is absorbed by catalyst, and phase change nanoparticles, if the mass of catalyst (10 mg) is negligible; the heat released from the reaction is absorbed by silica and indium as a discrete function of temperature:

$$H = (m_{SiO_2} C_{P,SiO_2} + m_{In} C_{P,In}) \cdot (T - T_0),\ (T<T_\mathrm{m})$$

$$H = (m_{SiO_2} C_{P,SiO_2} + m_{In} C_{P,In}) \cdot (T_m - T_0) + x \cdot m_{In} \cdot \Delta H_{In},\ (T=T_\mathrm{m},\ 0<x<1)$$

$$H = (m_{SiO_2} C_{P,SiO_2} + m_{In} C_{P,In}) \cdot (T - T_0) + m_{In} \cdot \Delta H_{In},\ (T>T_\mathrm{m}) \tag{45}$$

The complete oxidation process of methanol generates water and carbon dioxide:

$$CH_3OH + \frac{3}{2}O_2 = 2H_2O + CO_2$$

The enthalpy change of the reaction is $\Delta H^* = -676.5$ J/g.[265] Since the amount of methanol that is oxidized is a function of time, the total heat generation from the reaction can be described as $\Delta H = 0.064 \cdot t$ J. Thus, the temperature of the system is written as:

$$T = T_0 + \frac{0.064 \cdot C_0 \cdot t[kt + \exp(-kt)]}{(m_{SiO_2} C_{P,SiO_2} + m_{In} C_{P,In})}, \ (T < T_{\mathrm{m}})$$

$$T = T_0 + \frac{0.064 \cdot C_0 \cdot t[kt + \exp(-kt)] - x \cdot m_{In} \cdot \Delta H_{In}}{(m_{SiO_2} C_{P,SiO_2} + m_{In} C_{P,In})}, \ (T = T_{\mathrm{m}},\ 0 < x < 1)$$

$$T = T_0 + \frac{0.064 \cdot C_0 \cdot t[kt + \exp(-kt)] - m_{In} \cdot \Delta H_{In}}{(m_{SiO_2} C_{P,SiO_2} + m_{In} C_{P,In})}, \ (T > T_{\mathrm{m}}) \qquad (46)$$

where $C_0 = 0.17$, $C_{\mathrm{P,SiO2}} = 0.7$ J/gK, $C_{\mathrm{P,In}} = 0.23$J/gK, $\Delta H_{\mathrm{In}} = 28.58$J/g, $T_0 = 120$ ºC, $T_{\mathrm{m}} = 156.7$ ºC, $m_{\mathrm{SiO2}} = 1$g, $m_{\mathrm{In}} = 1$ g. Inputting these values into equation 36 gives

$$T = T_0 + \frac{0.064 \cdot C_0 \cdot t[kt + \exp(-kt)]}{(m_{SiO_2} C_{P,SiO_2} + m_{In} C_{P,In})} = 120 + 0.012 \cdot t \cdot [10t + \exp(-10t)] \qquad (47)$$

When the temperature reaches the melting point of indium, the temperature will be maintained until all indium melts. Then the temperature will continue to increase as shown in equation 11:

$$T = T_0 + \frac{0.064 \cdot C_0 \cdot t[kt + \exp(-kt)]}{(m_{SiO_2} C_{P,SiO_2} + m_{In} C_{P,In})} = 125.77 + 0.016 \cdot t \cdot [10t + \exp(-10t)] \qquad (48)$$

where $k = A\exp(-E_{act} / RT)$,[266] and k is dependent on temperature and activation energy.[266-268] Figure 67A shows the relation between temperature and time, where the temperature of 1 g of silica increases faster than that of 2 g of silica due to low thermal mass; the temperature of 1 g of silica with 1 g of indium nanoparticles shows a 25 min delay. The length of delay is dependent on the mass of indium nanoparticles and the rate constant of reaction. If the mass of indium nanoparticles is constant, the delay time will decrease as the rate constant increases (Figure 67B). The delay time does not change for *Log*(k) < -4 S^{-1}, but decreases rapidly from 43 to 3 min when

Log(k) increases from -4 to -1 S^{-1}. For *Log*(k) = 1 S^{-1}, the delay lasts 16 sec.

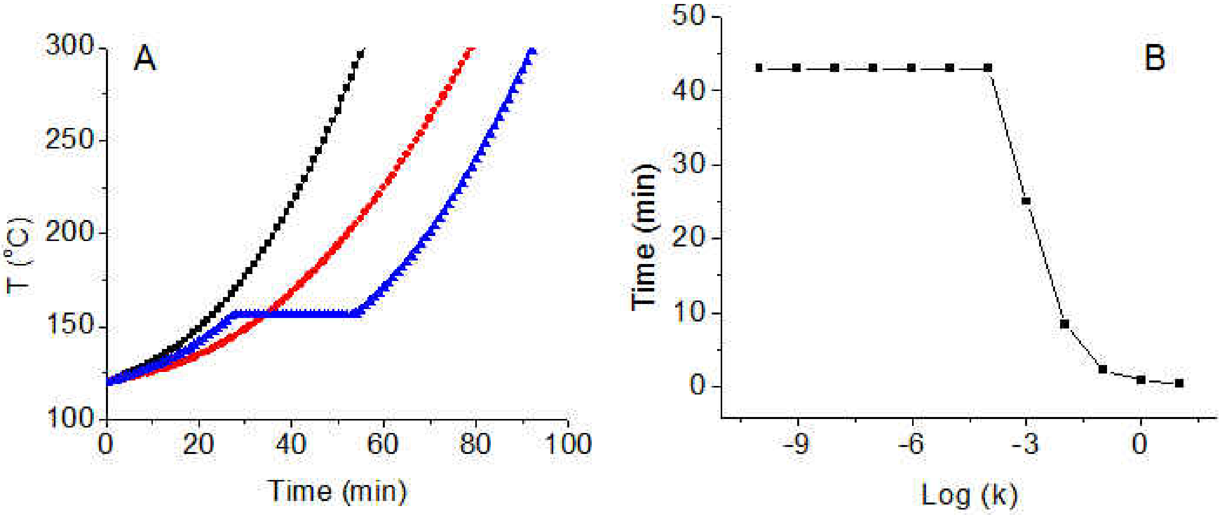

Figure 67. Simulated temperature rises as functions of time when the mass ratio of silica and indium is 1:0 (square), 2:0 (circle), and 1:1 (triangle) (A); melting delay as function of rate constant (B).

The temperature rise delay demonstrated in these experiments efficiently restricts thermal runaway of the catalytic reactions, and can provide one additional application benefit – temperature stabilization of pulsed or interrupted reactions. One broad technological application would be stabilization of electrode temperatures inside rechargeable ionic battery cells. All modern battery technologies incorporate nanostructures surfaces of electrodes to increase ionic exchange areas and achieve a high density of the electrical energy storage. With such technologies, there is an increased risk of the temperature spikes during rapid charging and discharging event, which may lead to the battery thermal runaway with significant degradation of properties, as well as an occasional catastrophic failure by explosion and fire. The discussed here encapsulated PCM nanoparticles can efficiently be applicable for battery electro-chemical reaction temperature runaway mitigation. Particle dielectric shell can provide for a reduced interference with the electrical current flow, while the small size will allow for a rapid response time and reliable response in multiple thermal cycles expected during the battery life.

6.5 Conclusions

Adding encapsulated phase change nanoparticles into exothermic reaction systems such as catalytic and polymerization reactions can effectively quench local hot spots, prevent thermal runaway, and change product distribution. A rational design of nano-heat-sinks with different core materials and shell materials can extend the use of this method to a broad range of exothermic reactions. By using different phase change materials, the operating range of nano-heat-sinks can be changed. In particular, silica encapsulated phase change nanoparticles can be used as new multifunctional catalyst support with thermal management capability, which is critical for multiple chemical processes ranging from high quality polymer manufacturing to battery applications.

CHAPATER 7   CONCLUSIONS AND FUTURE WORKS

7.1 Conclusions

In this study, encapsulated nanoPCM suspensions based on water and PAO are prepared in order to study the heat transfer enhancement by using the phase change properties. Silica encapsulated indium nanoparticles and polymer encapsulated paraffin wax nanoparticles have been made as examples at high yield and low cost for both high temperature and low temperature heat transfer applications. A nanoemulsion (or miniemulsion) method has developed to synthesis those nanoparticles. The thermophysical properties of those nanoPCM suspensions, including melting behavior, heat capacity, viscosity and permittivity have been investigated experimentally.

Indium nanoparticles are synthesized by boiling indium powders in PAO by magnetic stirring at 200ºC, the liquid indium is chopped into nanoparticles under the strong shear force of PAO. The indium nanoparticles are then centrifused and dispersed into ethanol, TEOS is decomposed to derive the shell of silica so as to protect the indium. Polymer encapsulated ax nanoparticles are synthesized using oil-in-water miniemulsion method, polymerization occurs at the interface of wax and water, forming a polymer shell to protect the inside nanoPCM.

Adding such nanoparticles into single phase fluid (i.e., PAO or water) enhances the thermophysical properties (i.e., heat transfer, heat capacity, and dielectric constant) of fluids. The heat transfer coefficients of PAO and water increased for 28% and 75% by adding 9% and 10% mass ratio of encapsulated indium and wax. The dielectric properties of the base fluid have been preserved or enhanced for by the high dielectric shell, and, the measured dielectric constant decreases as the frequency increases.

The fast melting of encapsulated nanoparticles allows complete utilization of latent heats of phase changes. The colloid suspension of encapsulated nanoparticles with its high heat transfer property can be used as novel coolants for direct immersion cooling of both low and high temperature devices. The core-shell structure is preserved after the heat loop test, the robust core-shell structure could be used many cycles for the heat transfer applications.

There are two existing problems that being unsolved so far, one is supercooling of nanoPCM, the other is the increase in viscosity. Supercooling of indium nanoparticles can be dramatically reduced by heterogeneous nucleation on silica derived from sodium silicate. Sodium silicate can decompose into silica through controlling pH value by adding dilute hydrogen chloride aqueous solution. Both surface roughness and semicrystalline structure of silica can lower the threshold of nucleation, and thereof the degree of super-cooling. The effects of overheating, heating and cooling rates are understood from heterogeneous nucleation, and thermal inertia of instrument. Degree of supercooling is proportional to the degree of overheating when the overheating is between 0 and 40ºC higher than the melting point of indium, the effect is not obvious when it is higher than that. The instrumental effects like the speeds of heating and cooling also affect the shapes and peak positions of the DSC curves. The faster the heating/cooling speeds, the larger of the melting/freezing peaks. The melting/freezing peaks can shift as much as 10ºC by controlling the temperature scanning rates from 1 to 40ºC/min on silica encapsulated indium from TEOS. By reducing super-cooling of indium nanoparticles, the effective heat transfer coefficient of nanoparticle suspension can be enhanced for 5-6 times.

The higher viscosities result from adding encapsulated nanoparticles is another obstacle preventing the further applications of nanoPCM in the heat transfer fluid system. The viscosities of nanoPCM suspensions could be many times higher than the pure fluids due to the clustering of nano-PCMs and bad dispersions in the fluids. By surface modification of the silica shell, the viscosities as well as the pressure drops can be greatly reduced by increase the repulsion force between nanoparticles and good dispersions.

Adding encapsulated phase change nanoparticles into exothermic reaction systems such as catalytic and polymerization reactions can effectively quench local hot spots, prevent thermal runaway, and change product distribution. A rational design of nano-heat-sinks with different core and shell materials can extend the use of this method to a broad range of exothermic reactions. By using different phase change materials with different melting temperatures, the operating range of nano-heat-sinks can be changed. Silica-encapsulated indium nanoparticles and silica encapsulated paraffin nanoparticles are used to absorb heat released in catalytic reaction, and to mitigate gel effect of polymerization, respectively. The local hot spots that are induced by nonhomogenous catalyst packing, reactant concentration fluctuation, and abrupt change of polymerization rate lead to solid to liquid phase change of nanoparticle cores so as to avoid thermal runaway by converting energies from exothermic reactions to latent heat of fusion. By quenching local hot spots at initial stage, reaction rates do not raise significantly because the thermal energy produced in reaction is isothermally removed. The silica encapsulated indium nanoparticles have suppressed the temperature of catalytic reactions from 351ºC to 120ºC by controlling the mass ratio of catalyst and phase change nanoparticles; the temperature of polymerization can be controlled from 120ºC to 80ºC by adding certain amount of silica encapsulated wax microparticles. The stable retarding temperature that those nanoparticles can control depends on the latent heats of fusion and the heat released from catalytic reactions and polymerizations. Micro/nanoparticles of phase change materials will open a new dimension for thermal management of exothermic reactions to quench local hot spots, prevent thermal runaway of reaction, and change product distribution.

7.2 Future Works

Current liquid based cooling techniques mainly rely on the thermal conductivity and heat capacity of coolant, but most of them are low on both of these parameters. The lower heat capacity can be improved by adding nano-PCMs into the fluids, while the lower thermal conductivity is still an existing problem. Liquid metal usually have ultra high thermal conductivity that is comparable to pure metals and low viscosity comparable to coolants. By combining the nano-PCMs and liquid metals, both the thermal conductivity and heat capacity problems can be resolved. The only thing is the liquid metals are corrosive to metal channels, which can be solved by using plastic pipes instead of metals pipes.

On the other hand, the heat transfer ability of coolant can also be increased by combining solid-liquid phase change of nano-PCMs and liquid-vapor phase change of coolants like perfluorohexane. By choosing similar solid-liquid phase transition temperature of nano-PCMs and liquid-vapor phase transition temperature of coolants, the heat transfer ability will be greatly enhanced.

Phase change materials are suitable for thermal regulations of temperature fluctuations. Polymer encapsulated wax micro/nano fibers and particles can be prepared either through a simple fiber-drawing nanomanufacturing (FDN) process or using a miniemulsion method. The obtained structures can be either added into concrete or fabricated into fabric cloth as thermal regulators for reducing the temperature fluctuation of inner environment. The thermal regulating properties of polymer encapsulated wax nanoparticles and microfibers on concrete blocks or fabric texiles filling with those materials with phase change materials can reserve a constant temperature for a tunable period by controlling the mass ratio of phase change materials. The large latent heat of paraffin wax makes the wax/polymer core-shell fiber a good candidate for thermal regulating system.

APPENDIX PHYSICAL PROPERTIES

Viscosity of Nano-PCMs Suspensions

The rheological property of nanoparticles suspension had been studied by Einstein since 1906, wherein a Stokes-Einstein was developed to predict the approximation of a liquid with spherical nanoparticles:

$$\mu_{NP} = \mu(1 + 2.5\phi) \tag{49}$$

where μ_{NPS} is the viscosity of nanoparticles suspension and ϕ is the volume fraction of solid dispersed nanoparticles. The equation is valid only when the suspension is dilute, where the interactions between nanoparticles are negligible. With the increasing on nanoparticle concentration, the hydrodynamics interactions and agglomeration of nanoparticles bring about a higher ordered term:

$$\mu_{NPS} = \mu(1 + 2.5\phi + 6.2\phi^2 + ...) \tag{50}$$

This so-called Einstein-Batchelor equation enables the calculation of the non-linear relationship between the relative viscosities versus volume concentrations of nanoparticles up to 10 vol%. Later on, a more accurate correlations which includes the temperature dependence of the viscosity had been developed by White:

$$\ln\frac{\mu_{NPS}}{\mu} = a + b(\frac{T_0}{T}) + c(\frac{T_0}{T})^2) \tag{51}$$

where T is the operating temperature; T_0 is reference temperature; a, b and c are dimensionless coefficients which can be derived by fitting the experimental data. This equation had been proved to have good agreement with the experimental results by Kulkrni, who developed a more robust correlation equation:

$$\ln \mu_{NPS} = a(\frac{1}{T}) - b \tag{52}$$

where $a = 20587\phi^2 + 15857\phi + 1078.3$, $\mathrm{b} = \text{-}107.12\phi^2 + 53.548\phi + 2.8715$.

Density of Nano-PCMs Suspensions

The density of nano-PCMs suspension can be calculated as:

$$\rho_{NPS} = \frac{m_{NPS}}{Vol_{NPS}} = \phi\rho_{NP} + (1-\phi)\rho_f \tag{53}$$

where m_{NPS} and Vol_{NPS} are the mass and volume of nano-PCMs suspension, respectively; ρ_{NPS}, ρ_{NP} and ρ_f are the densities of nano-PCMs suspension, nano-PCM and base fluid, respectively.

PUBLICATIONS

1. Ming Su, Liyuan Ma, **Yan Hong**, Thermo-probes, methods of making thermo-probes, and methods of detection using thermo-probes, 2011, US Patent, 2921021560, USA.
2. **Y. Hong**, Z. Ma, M. Su, Self-healing materials with integrated reporting networks of conductive microwires, *ACS Applied Materials & Interfaces*, 2011, submitted.
3. **Y. Hong**, C. Wang, M. Hossain, R. Qiu, M. Su, Silica microbeads with embedded phase change nanoparticles as ultrahigh capacity thermal barcodes, *Small*, 2011, submitted.
4. **Y. Hong**, S. Ding, Z. Ma, M. Su, Micro/nano nanoparticles and fibers with phase change cores for thermal regulations, *International Journal of Nano and Smart Materials*, 2011, submitted.
5. **Y. Hong**, W. Wu, J. Hu, A. A. Voevodin, M. Zhang, L. Chow, M. Su, Controlling super-cooling of silica encapsulated phase change nanoparticles for enhanced heat transfer application, *Chemical Physics Letters*, 2011, 504, 180.
6. W. Wu, H. Bostanci, Y. R. Lin, L. Chow, S. Ding, **Y. Hong**, M. Su, Jet impingement and spray cooling of nanoencapsulated phase change material slurry, *International Journal of Heat and Mass Transfer*, 2011, in press.
7. W. Wu, H. Bostanci, L. Chow, **Y. Hong**, S. Ding, M. Su, J.P. Kizito, Jet Impingement of Air-particle Suspensions with Nanoencapsulated Phase Change Materials, *International Journal of Heat and Mass Transfer*, 2011, submitted.
8. **Y. Hong**, J. Tao, M. Su, Internet-based remote nano-characterization and lithography using atomic force microscopy, Journal of Nano Education, 2011, in press.

9. **Y. Hong**, W. Wu, S. Ding, J. Hu, A. A. Voevodin, L. Gschwender, Ed. Snyder, L. Chow, M. Su, Enhancing heat capacity of colloidal suspension using nanoscale encapsulated phase-change materials for heat transfer, *ACS Applied Materials & Interfaces,* 2010, 2, 1685.
10. **Y. Hong***, M. Zhang*, S. Ding, J. Hu, Y. Fan, A. A. Voevodin, M. Su, Encapsulated nano-heat-sinks for thermal management of heterogeneous chemical reactions, *Nanoscale*, 2010, 2, 2790. (equal contribution)
11. W. Wu, H. Bostanci, L. Chow, **Y. Hong**, M. Su, Nucleate boiling heat transfer enhancement for water and FC-72 on titanium oxide and silicon oxide surfaces, *International Journal of Heat and Mass Transfer*, 2010, 53, 1773.
12. L. Ma, C. Wang, **Y. Hong**, M. Zhang, M. Su, Thermally-addressed immunosorbent assay for multiple protect detections using phase change nanoparticles, *Analytical Chemistry*, 2010, 82, 1186.
13. **Y. Hong**, Z. Ma, C. Wang, L. Ma, M. Su, 3D Ordered Assemblies of semiconductive micro/nanowires using microscale fibrous building blocks, *ACS Applied Materials & Interfaces*, 2009, 1, 251.
14. **Y. Hong**, M. Su, 3D ordered assemblies of micro/nanowires using fibrous building blocks, ECS Transactions, 2010, 33, 49.
15. **Y. Hong***, Z. Ma*, L. Ma, Y. Ni, S. Zou, M. Su, Curvature-controlled micro/nanostructures created by Diffusion-limited chemical etching of artificially engineered solids, *Langmuir*, 2009, 25, 643. (equal contribution)
16. L. Ma, **Y. Hong**, Z. Ma, C. Kaittanis, J. M. Perez, M. Su, Multiplexed highly sensitive detections of cancer biomarkers in thermal space using encapsulated phase change

nanoparticles. *Applied Physics Letters*, 2009, 95, 043701.

17. Z. Ma, **Y. Hong**, M. Zhang, M. Su, Encoding and decoding nanoscale thermal barcodes for ultrahigh capacity identification systems, *Applied Physics Letters*, 2009, 95, 233101.

REFERENCES

1. Maxwell, C. J., *Electricity and Magnetism*. Oxford : Clarendon Press: 1873.

2. Choi, S. U. S.; eastman, J. A. In *Enhancing thermal conductivity of fluids with nanoparticles*, Int. Mech. Eng. Cong. Exh., San Francisco, CA.

3. Chen, G., Nonlocal and nonequilibrium heat conduction in the vicinity of nanoparticles. *J. Heat Transfer* **1996,** *118*, 539.

4. Chen, G., Nanoscale heat transfer. *Encyclopedia of Nanoscience and Nanotechnology* **2004,** *7*, 429.

5. Shalkevich, N.; Escher, W.; Burgi, T.; Michel, B.; Si-Ahmed, L.; Poulikakos, D., On the thermal conductivity of gold nanoparticle colloids. *Langmuir* **2010,** *26*, 663.

6. Timofeeva, E. V.; Yu, W.; M., F. D.; Singh, D.; Routbort, J. L., Nanofluids for heat transfer: an engineering approach. *Nanoscale Res. Lett.* **2011,** *6*, 182.

7. Wong, K. V.; Castillo, M. J., Heat transfer mechanisms and clustering in nanofluid. *Adv. Mech. Eng.* **2010,** *795478*.

8. Buongiorno, J.; Venerus, D.; Prabhat, N.; et al, A benchmark study on the thermal conductivity of nanofluids. *J. Appl. Phys.* **2009,** *106*.

9. Nan, C. W.; Birringer, R.; Clarke, D. R.; Gleiter, H., Effective thermal conductivity of particulate composites with interfacial thermal resistance. *J. Appl. Phys.* **1997,** *81*, 6692.

10. Xu, J.; Yang, B.; Hammouda, B., Thermal conductivity and viscosity of self-assembled alcohol/polyalphaolefin nanoemulsion fluids. *Nanoscale Res. Lett.* **2011,** *6*, 274.

11. Farid, M. M.; Khudhair, A. M.; Razack, S. A. K.; Al-Hallaj, S., A review on phase change energy storage: materials and applications. *Energy Convers. Manage.* **2004,** *45*, 1597.

12. Barber, J.; Brutin, D.; Sefiane, K.; Tadrist, L., Bubble confinement in flow boiling of FC-72 in a "rectangular" microchannel of high aspect ratio. *Exp. Therm Fluid Sci.* **2010,** *34*, 1375.

13. Anandan, S. S.; Ramalingam, V., Thermal management of electronics: a review of literature. *Therm. Sci.* **2008,** *12*, 5.

14. Zhang, Y.; Christofferson, J.; Shakouri, A.; G., Z.; Bowers, J. E., On-chip high speed localized cooling using superlattice microrefrigerators. *IEEE Trans. Compon. Packag. Technol.* **2006,** *29*, 395.

15. A., S. W., *Cooling of electronic equipment*. John Wiley and Sons - Interscience: New York, 1974.

16. Florio, L. A.; Harnoy, A., Combination technique for improving natural convection cooling in electronics. *Int. J. Therm. Sci.* **2007,** *46*, 76.

17. Tso, C. P.; Tou, K. W.; Bhowmik, H., Experimental and numerical thermal transient behavior of chips in a liquid channel during loss of pumping power. *J. Electron. Packaging* **2004,** *126*, 546.

18. Bhowmik, H.; Tou, K. W., Experimental study of transient natural convection heat transfer from simulated electronic chips. *Exp. Therm Fluid Sci.* **2005,** *29*, 485.

19. Kercher, D. S.; Jeong-Bong, L.; Brand, O.; Allen, M. G.; Glezer, A., Microjet cooling devices for thermal management of electronics. *IEEE T. Compon. Pack. T.* **2003,** *26*, 359.

20. Lee, S.; Culham, J. R.; Yovanovich, M. M., The effect of common design parameters on the thermal performance of micro electronic equipment, part 1 - Natural convection. *Heat Transfer Electron. Equip.* **1991,** *171*, 47.

21. Barcohen, A., Thermal management of electronic components with dielectric liquids. *JSME*

Int J., Ser. B **1993,** *36*, 1.

22. You, S. M.; Simon, T. W.; Barcohen, A., A technique for enhancing boiling heat-transfer with application to cooling of electronic equipment. *IEEE T. Compon. Hybr.* **1992,** *15*, 823.

23. Hummel, R. L.; Marto, P. J.; Vachon, R. I., Discussion of pool boiling heat transfer from teflon-coated stainless steel. *J. Heat Transfer* **1969,** *91*, 369.

24. Betz, A. R.; Xu, J.; Qiu, H. H.; Attinger, D., Do surfaces with mixed hydrophilic and hydrophobic areas enhance pool boiling? *Appl. Phys. Lett.* **2010,** *97*, 141909.

25. Yang, Y. T.; Lai, F. H., Numerical study of heat transfer enhancement with the use of nanofluids in radial flow cooling system. *Int. J. Heat Mass Transfer* **2010,** *53*, 5895.

26. Xing, Y. F.; Weigand, B., Experimental investigation of impingement heat transfer on a flat and dimpled plate with different crossflow schemes. *Int. J. Heat Mass Transfer* **2010,** *53*, 3874.

27. Naphon, P.; Wongwises, S., Investigation on the jet liquid impingement heat transfer for the central processing unit of personal computers. *Int. Commun. Heat Mass* **2010,** *37*, 822.

28. Koseoglu, M. F.; Baskaya, S., The role of jet inlet geometry in impinging jet heat transfer, modeling and experiments. *Int. J. Therm. Sci.* **2010,** *49*, 1417.

29. Kanokjaruvijit, K.; Martinez-Botas, R. F., Heat transfer correlations of perpendicularly impinging jets on a hemispherical-dimpled surface. *Int. J. Heat Mass Transfer* **2010,** *53*, 3045.

30. Sung, M. K.; Mudawar, I., Effects of jet pattern on two-phase performance of hybrid micro-channel/micro-circular-jet-impingement thermal management scheme. *Int. J. Heat Mass Transfer* **2009,** *52*, 3364.

31. Robinson, A. J., A thermal-hydraulic comparison of liquid microchannel and impinging liquid jet array heat sinks for high-power electronics cooling. *IEEE T. Compon. Pack. T.* **2009,** *32*,

347.

32. Kandlikar, S. G.; Bapat, A. V., Evaluation of jet impingement, spray and microchannel chip cooling options for high heat flux removal. *Heat Transfer Eng.* **2007,** *28*, 911.

33. Vasiliev, L. L., Micro and miniature heat pipes - Electronic component coolers. *Appl. Therm. Eng.* **2008,** *28*, 266.

34. Howard, A. H.; Peterson, G. P., Investigation of a heat pipe array for convective cooling. *J. Electron. Packaging* **1995,** *117*, 208.

35. Groll, M.; Schneider, M.; Sartre, V.; Chaker Zaghdoudi, M.; Lallemand, M., Thermal control of electronic equipment by heat pipes. *Rev. Gen. Therm.* **1998,** *37*, 323.

36. Nnanna, A. G. A., Application of refrigeration system in electronics cooling. *Appl. Therm. Eng.* **2006,** *26*, 18.

37. Bian, Z. X.; Shakouri, A., Beating the maximum cooling limit with graded thermoelectric materials. *Appl. Phys. Lett.* **2006,** *89*.

38. LaBounty, C.; Shakouri, A.; Bowers, J. E., Design and characterization of thin film microcoolers. *J. Appl. Phys.* **2001,** *89*, 4059.

39. Shakouri, A.; Bowers, J. E., Heterostructure integrated thermionic coolers. *Appl. Phys. Lett.* **1997,** *71*, 1234.

40. Atik, K., Investigation of the performance of identical two-stage connected thermoelectric modules. *Isi Bilimi Ve Teknigi Dergisi-J. Therm. Sci. Tech.* **2007,** *27*, 1.

41. Borisenko, K. B.; Chen, Y. X.; Song, S. A.; Cockayne, D. J. H., Nanoscale phase separation and building blocks of Ge2Sb2Te5N and Ge2Sb2Te5N2 thin films. *Chem. Mater.* **2009,** *21*, 5244.

42. Lafdi, K.; Mesalhy, O.; Elgafy, A., Merits of employing foam encapsulated phase change materials for pulsed power electronics cooling applications. *J. Electron. Packaging* **2008,** *130*.

43. Salaun, F.; Devaux, E.; Bourbigot, S.; Rumeau, P., Thermoregulating response of cotton fabric containing microencapsulated phase change materials. *Thermochim. Acta* **2010,** *506*, 82.

44. Halawa, E.; Saman, W., Thermal performance analysis of a phase change thermal storage unit for space heating. *Renew. Energ.* **2010,** *36*, 259.

45. Evers, A. C.; Medina, M. A.; Fang, Y., Evaluation of the thermal performance of frame walls enhanced with paraffin and hydrated salt phase change materials using a dynamic wall simulator. *Build. Enviorn.* **2010,** *45*, 1762.

46. Keblinski, P.; Phillpot, S. R.; Choi, S. U. S.; Eastman, J. A., Mechanisms of heat flow in suspensions of nano-sized particles (nanofluids). *Int. J. Heat Mass Transfer* **2002,** *45*, 855.

47. Wang, B.-X.; Zhou, L.-P.; Peng, X.-F., A fractal model for predicting the effective thermal conductivity of liquid with suspension of nanoparticles. *Int. J. Heat Mass Transfer* **2003,** *46*, 2665.

48. Yu, W.; Choi, S. U. S., The role of interfacial layers in the enhanced thermal conductivity of nanofluids: A renovated Maxwell model. *J. Nanoparticle Res.* **2003,** *5*, 167.

49. Kumar, D. H.; Patel, H. E.; Kumar, V. R. R.; Sundararajan, T.; Pradeep, T.; Das, S. K., Model for heat conduction in nanofluids. *Phys. Rev. Lett.* **2004,** *93*, 144301.

50. Prasher, R.; Bhattacharya, P.; Phelan, P. E., Thermal conductivity of nanoscale colloidal solutions (nanofluids). *Phys. Rev. Lett.* **2005,** *94*, 025901.

51. Zhang, X.; Gu, H.; Fujii, M., Effective thermal conductivity and thermal diffusivity of nanofluids of nanofluids containing spherical and cylindrical nanoparticles *Appl. Phys. Lett.*

2006, *100*, 044325.

52. Gao, L.; Zhou, X.; Ding, Y., Effective thermal and electrical conductivity of carbon nanotube composites. *Chem. Phys. Lett.* **2007,** *434*, 297.

53. Putnam, P. A.; Cahill, D. G.; Braun, P. V.; Ge, Z., Thermal conductivity of nanoparticle suspensions. *J. Appl. Phys.* **2006,** *99*, 084308.

54. Patel, H. E.; Das, S. K.; Sundararajan, T.; Nair, A. S.; George, B.; Pradeep, T., Thermal conductivities of naked and monolayer protected metal nanoparticle based nanofluids: Manifestation of anomalous enhancement and chemical effects. *Appl. Phys. Lett.* **2003,** *83*, 2931.

55. Schmidt, A. J.; Chiesa, M.; Torchinsky, D. H.; Johnson, J. A.; Nelson, K. A.; Chen, G., Thermal conductivity of nanoparticle suspensions in insulating media measured with a transient optical grating and a hotwire. *J. Appl. Phys.* **2007,** *103*, 083529.

56. Gao, J. W.; Zheng, R. T.; Ohtani, H.; Zhu, D. S.; Chen, G., Experimental investigation of heat conduction mechanisms in nanofluids. clue on clustering. *Nano Lett.* **2009,** *9*, 4128.

57. Putra, N.; Roetzel, W.; Das, S., Natural convection of nano-fluids. *Heat Mass Transfer.* **2003,** *39*, 775.

58. Khanafer, K.; Vafai, K.; Lightstone, M., Buoyancy-driven heat transfer enhancement in a two-dimensional enclosure utilizing nanofluids. *Int. J. Heat Mass Transfer* **2003,** *46*, 3639.

59. Nanna, A. G. A.; Fistrovich, T.; Malinski, K.; Choi, S. U. S. In *Thermal transport phenomena in buoyancy-driven nanofluids*, SAME Int. Mech. Eng. Cong. Rd&D Exp., Anaheim, CA, USA.

60. Xuan, Y. M.; Roetzel, W., Conceptions for heat transfer correlation of nanofluids. *Int. J. Heat Mass Transfer* **2000,** *43*, 3701.

61. Xuan, Y.; Li, Q., Investigation on convective heat transfer and flow features of nanofluids. *J. Heat Transfer* **2003,** *125*, 151.

62. Yang, Y.; Zhang, Z. G.; Grulke, E. A.; Anderson, W. B.; Wu, G., Heat transfer properties of nanoparticle-in-fluid dispersions (nanofluids) in laminar flow. *Int. J. Heat Mass Transfer* **2005,** *48*, 1107.

63. Hawlader, M. N. A.; Uddin, M. S.; Zhu, H. J., Encapsulated phase change materials for thermal energy storage. *Int. J. Energy Res.* **2002,** *26*, 159.

64. Hisham, E.; Hisham, E.-D.; Eman, A.-K., Heat transfer characteristics during melting and solidification of phase change energy storage process. *Ind. Eng. Chem. Res.* **2004,** *43*, 5350.

65. Kenisarin, M.; Mahkamov, K., Solar energy storage using phase change materials. *Renew. Sust. Energ. Rev.* **2007,** *11*, 1913.

66. Pandian, R.; Kooi, B. J.; Hosson, J. T. M. D., Influence of electron beam exposure on crystallization of phase-change materials. *J. App. Phys.* **2007,** *101*, 053529.

67. Zivkovic, B.; Fujii, I., An analysis of isothermal phase change of phase change materials within rectangular and cylindrical containers. *Solar Energy* **2000,** *70*, 51.

68. Farid, M. M.; Khudhair, A. M.; Razack, S. A. K.; Al-Hallaj, S., A review on phase change energy storage: materials and applications. *Appl. Catal., A* **2004,** *45*, 1597.

69. Su, X.; Zhao, J.; Zhao, X.; Guo, Y.; Zhu, Y.; Wang, Z., A facile synthesis of Cu_2O/SiO_2 and Cu/SiO_2 core-shell octahedral nanocomposites. *Nanotechnology* **2008,** *19*, 365610.

70. Medrano, M.; Yilmaz, M. O.; Nogues, M.; Martorell, I.; Roca, J.; Cabeza, L. F., Experimental evaluation of commercial heat exchangers for use as PCM thermal storage systems. *Applied Energy* **2009,** *86*, 2047.

71. Adine, H. A.; El Qarnia, H., Numerical analysis of the thermal behaviour of a shell-and-tube heat storage unit using phase change materials. *Appl. Math. Model.* **2009,** *33*, 2132.

72. Hamada, Y.; Ohtsu, W.; Fukai, J., Thermal response in thermal energy storage material around heat transfer tubes: effect of additives on heat transfer rates. *Solar Energy* **2003,** *75*, 317.

73. Esen, M.; Durmus, A., Geometric design of solar-aided latent heat store depending on various parameters and phase change materials. *Solar Energy* **1998,** *62*, 19.

74. Huang, M. J.; Eames, P. C.; Norton, B., Thermal regulation of building-integrated photovoltaics using phase change materials. *Int. J. Heat Mass Transfer* **2004,** *47*, 2715.

75. Sharma, A.; Won, L. D.; Buddhi, D.; Park, J. U., Numerical heat transfer studies of the fatty acids for different heat exchanger materials on the performance of a latent heat storage system. *Renew. Energ.* **2005,** *30*, 2179.

76. Wang, Y.; Amiri, A.; Vafai, K., An experimental investigation of the melting process in a rectangular enclosure. *Heat Mass Transfer.* **1999,** *42*, 3659.

77. Tuncbilek, K.; Sari, A.; Tarhan, S.; Ergunes, G.; Kaygusuz, K., Lauric and palmitic acids eutectic mixture as latent heat storage material for low temperature heating applications. *Energy* **2005,** *30*, 677.

78. Sharma, A.; Tyagi, V. V.; Chen, C. R.; Buddhi, D., Review on thermal energy storage with phase change materials and applications. *Renewable and Sustainable Energy Reviews* **2009,** *13*, 318.

79. Fukai, J.; Hamada, Y.; Morozumi, Y.; Miyatake, O., Improvement of thermal characteristics of latent heat thermal energy storage units using carbon-fiber brushes: experiments and modeling. *Int. J. Heat Mass Transfer* **2003,** *46*, 4513.

80. Ismail, K. A. R.; Alves, C. L. F.; Modesto, M. S., Numerical and experimental study on the solidification of PCM around a vertical axially finned isothermal cylinder. *Appl. Therm. Eng.* **2001,** *21*, 53.

81. Nagano, K.; Ogawa, K.; Mochida, T.; Hayashi, K.; Ogoshi, H., Performance of heat charge/discharge of magnesium nitrate hexahydrate and magnesium chloride hexahydrate mixture to a single vertical tube for a latent heat storage system. *Appl. Therm. Eng.* **2004,** *24*, 209.

82. Choi, J. C.; Kim, S. D., Heat-transfer characteristics of a latent heat storage system using MgCl2 ?6H2O. *Energy* **1992,** *17*, 1153.

83. Hong, Y.; Ding, S.; Wu, W.; Hu, J.; Voevodin, A. A.; Gschwender, L.; Snyder, E.; Chow, L.; Su, M., Enhancing heat capacity of colloidal suspension using nanoscale encapsulated phase-change materials for heat transfer. *ACS Appl. Mater. Interface* **2010,** *2*, 1685.

84. Agyenim, F.; Hewitt, N.; Eames, P.; Smyth, M., A review of materials, heat transfer and phase change problem formulation for latent heat thermal energy storage systems (LHTESS). *Renewable and Sustainable Energy Reviews* **2010,** *14*, 615.

85. Pincemin, S.; Olives, R.; Py, X.; Christ, M., Highly conductive composites made of phase change materials and graphite for thermal storage. *Sol. Energy Mater. Sol. Cells* **2008,** *92*, 603.

86. Zalba, B.; Marin, J. M.; Cabeza, L. F.; Mehling, H., Review on thermal energy storage with phase change: materials, heat transfer analysis and applications. *Appl. Therm. Eng.* **2003,** *23*, 251.

87. Gong, Z.-X.; Mujumdar, A. S., Finite-element analysis of cyclic heat transfer in a shell-and-tube latent heat energy storage exchanger. *Appl. Therm. Eng.* **1997,** *17*, 583.

88. Velraj, R.; Seeiraj, R. V.; Hafner, B.; Faber, C.; Schwarzer, K., Heat transfer enhancement in a latent heat storage system. *Solar Energy* **1999,** *65*, 171.

89. Han, Z. H.; Cao, F. Y.; Yang, B., Synthesis and thermal characterization of phase-changeable indium/polyalphaolefin nanofluids. *Appl. Phys. Lett.* **2008,** *92*, 243104.

90. Wuttig, M.; Steimer, C., Phase change materials: From materials science to novel storage devices. *Appl. Phys. A* **2007,** *87*, 411.

91. Wang, C.; Ma, L.; Chen, L.-M.; Chai, K. X.; Su, M., Scanning calorimetric detections of multiple DNA biomarkers contained in complex fluids. *Anal. Chem.* **2010,** *82*, 1838.

92. Ma, L.; Wang, C.; Hong, Y.; Zhang, M.; Su, M., Thermally addressed immunosorbent assay for multiplexed protein detections using phase change nanoparticles. *Anal. Chem.* **2010,** *82*, 1186.

93. Ma, L.; Hong, Y.; Ma, Z.; Kaittanis, C.; Perez, J. M.; Su, M., Multiplexed highly sensitive detections of cancer biomarkers in thermal space using encapsulated phase change nanoparticles. *Appl. Phys. Lett.* **2009,** *95*, 043701.

94. Stoval, T. K.; Tomlinson, J. J., A review on phase change energy storage: materials and applications. *Trans. ASME* **1995,** *117*, 318.

95. Neeper, D. A., Thermal dynamics of wallboard with latent heat storage. *Solar Energy* **2000,** *68*, 393.

96. Athienitis, A. K.; Liu, C.; Hawes, D.; Banu, D.; Feldman, D., Investigation of the thermal performance of a passive solar test-room with wall latent heat storage. *Building Environ.* **1997,** *32*, 405.

97. Mondal, S., Phase change materials for smart textiles - An overview. *Appl. Therm. Eng.*

2008, *28*, 1536.

98. Pause, B., Driving more comfortably with phase change materials. *Tech. Textiles Int.* **2002,** *11*, 24.

99. Zuckerman, J. L.; Pushaw, R. J.; Perry, B. T.; Wyner, D. M. Fabric coating containing energy absorbing phase change material and method of manufacturing same. US P6514362, 2003.

100. Pause, B. Building conditioning technique using phase change materials. 2001.

101. Zhang, X.-X.; Fan, Y.-F.; Tao, X.-M.; Yick, K.-L., Crystallization and prevention of supercooling of microencapsulated n-alkanes. *J. Colloid Interface Sci.* **2005,** *281*, 299.

102. Nagano, K.; Mochida, T.; Takeda, S.; Domanski, R.; Rebow, M., Thermal characteristics of manganese (II) nitrate hexahydrate as a phase change material for cooling systems. *Appl. Therm. Eng.* **2003,** *23*, 229.

103. Yokota, T.; Murayama, M.; Howe, J. M., In situ transmission-electron-microscopy investigation of melting in submicron Al-Si alloy particles under electron-beam irradiation. *Phys. Rev. Lett.* **2003,** *91*, 265504.

104. Isabel, P. S.; Koktysh, D. S.; Mamedov, A. A.; Giersig, M.; Kotov, N. A.; Liz-marzan, L. M., One-Pot synthesis of Ag@TiO_2 core-shell nanoparticles and their layer by layer assembly. *Langmuir* **2000,** *16*, 2731.

105. Kwon, H.-W.; Lim, Y.-M.; Tripathy, S. K.; Kim, B.-G.; Lee, M.-S.; Yu, Y.-T., Synthesis of Au/TiO_2 core shell nanoparticles from titanium isopropoxide and thermal resistance effect of TiO_2 shell. *Japn. J. Appl. Phys.* **2007,** *46*, 2567.

106. Fang, Y.; Kuang, S.; Gao, X.; Zhang, Z., Preparation and characterization of novel nanoencapsulate phase change materials. *Energ. Convers. Manage.* **2008,** *49*, 3704.

107. Prince, J.; Montoya, A.; Ferrat, G.; Valente, J. S., Proposed general sol-gel method to prepare multimetallic layered double hydroxides: synthesis, characterization, and envisaged application. *Chem. Mater.* **2009,** *21*, 5826.

108. Andreas, H. A.; Kung, S. K. Y.; McLeod, E. J.; Young, J. L.; Birss, V. I., Optimization of synthesis parameters employed during pt nanoparticle formation by in situ reduction. *J. Phys. Chem. C* **2007,** *111*, 13321.

109. Mackenzie, J. D.; Bescher, E. P., Chemical routes in the synthesis of nanomaterials using the sol-gel process. *Acc. Chem. Res.* **2007,** *40*, 810.

110. Soulantica, K.; Maisonnat, A.; Fromen, M.-C.; Casanove, M.-J.; Lecante, P.; Chaudret, B., Synthesis and self-assembly of monodisperse indium nanoparticles prepared from the organometallic precursor [In(η5-C5H5)]. *Angew. Chem. Int. Ed.* **2001,** *40*, 448.

111. Wang, Y. L.; Xia, Y. N., Bottom-up and top-down approaches to the synthesis of monodispersed spherical colloids of low melting-point metals. *Nano Lett.* **2004,** *4*, 2047.

112. Wang, F.; Rang, R.; Yu, H.; Gibbons, P. C.; Buhro, W. E., Size- and shape-controlled synthesis of bismuth nanoparticles. *Chem. Mater.* **2008,** *20*, 3656.

113. Salavati-Niasari, M.; Mir, N.; Davar, F., A novel precursor for synthesis of metallic copper nanocrystals by thermal decomposition approach. *Appl. Surf. Sci.* **2010,** *256*, 4003.

114. Salavati-Niasari, M.; Davar, F.; Mir, N., Synthesis and characterization of metallic copper nanoparticles via thermal decomposition. *Polyhedron* **2008,** *27*, 3514.

115. Nishijo, J.; Okabe, C.; Oishi, O.; Nishi, N., Synthesis, structures and magnetic properties of carbon-encapsulated nanoparticles via thermal decomposition of metal acetylide. *Carbon* **2006,** *44*, 2943.

116.D'Urso, L.; Nicolosi, V.; Compagnini, G.; Puglisi, O., Size distribution of silver nanoclusters induced by ion, electron, laser beams and thermal treatments of an organometallic precursor. *Appl. Surf. Sci.* **2004,** *226*, 131.

117.Chow, N. H.; Ke, X.; Schiffer, P.; Schaak, R. E., Room-temperature chemical synthesis of shape-controlled indium nanoparticles. *J. Am. Chem. Soc.* **2008,** *130*, 8140.

118.Chiu, H.-K.; Chiang, I. C.; Chen, D.-H., Synthesis of NiAu alloy and core–shell nanoparticles in water-in-oil microemulsions. *J. Nanopart. Res.* **2009,** *11*, 1137.

119.Zhang, Y.; Erkey, C., Preparation of supported metallic nanoparticles using supercritical fluids: A review. *J. Supercrit. Fluids* **2006,** *38*, 252.

120. Lee, Y.; Choi, J. R.; Lee, K. J.; Stott, N. E.; Kim, D., Large-scale synthesis of copper nanoparticles by chemically controlled reduction for applications of inkjet-printed electronics. *Nanotechnology* **2008,** *19*.

121. Margeat, O.; Ciuculescu, D.; Lecante, P.; Respaud, M.; Amiens, C.; Chaudret, B., NiFe nanoparticles: A soft magnetic material? *Small* **2007,** *3*, 451.

122. Juarez-Ruiz, E.; Pal, U.; Lombardero-Chartuni, J. A.; Medina, A.; Ascencio, J. A., Chemical synthesis and structural characterization of small AuZn nanoparticles. *Appl. Phys. A-Mater.* **2007,** *86*, 441.

123. Xiong, L. F.; He, T., Synthesis and characterization of ultrafine tungsten and tungsten oxide nanoparticles by a reverse microemulsion-mediated method. *Chem. Mater.* **2006,** *18*, 2211.

124. Wu, C. W.; Mosher, B. P.; Zeng, T. F., One-step green route to narrowly dispersed copper nanocrystals. *J. Nanopart. Res.* **2006,** *8*, 965.

125. Murphy, C. J.; San, T. K.; Gole, A. M.; Orendorff, C. J.; Gao, J. X.; Gou, L.; Hunyadi, S.

E.; Li, T., Anisotropic metal nanoparticles: Synthesis, assembly, and optical applications. *J. Phys. Chem. B* **2005,** *109*, 13857.

126. Sakamoto, M.; Fujistuka, M.; Majima, T., Light as a construction tool of metal nanoparticles: Synthesis and mechanism. *J. Photoch. Photobio. C* **2009,** *10*, 33.

127. Chang, D. W.; Dai, L. M., Photo-induced formation and self-assembling of gold nanoparticles in aqueous solution of amphiphilic dendrimers with oligo(p-phenylene vinylene) core branches and oligo(ethylene oxide) terminal chains. *Nanotechnology* **2007,** *18*.

128. Lavernia, E. J.; Han, B. Q.; Schoenung, J. M., Cryomilled nanostructured materials: Processing and properties. *Mat. Sci. Eng. A-Struct.* **2008,** *493*, 207.

129. Han, B. Q.; Ye, J.; Tang, F.; Schoenung, J.; Lavernia, E. J., Processing and behavior of nanostructured metallic alloys and composites by cryomilling. *J. Mater. Sci.* **2007,** *42*, 1660.

130. Witkin, D. B.; Lavernia, E. J., Synthesis and mechanical behavior of nanostructured materials via cryomilling. *Prog. Mater Sci.* **2006,** *51*, 1.

131. Witkin, D.; Han, B. Q.; Lavernia, E. J., Microstructural evolution of an ultrafine-grained cryomilled Al 5083 alloy during thermomechanical processing. *J. Mater. Res.* **2005,** *20*, 2117.

132. Zhang, X.; Wang, H.; Koch, C. C., Mechanical behavior of bulk ultrafine-grained and nanocrystalline Zn. *Rev. Adv. Mater. Sci.* **2004,** *6*, 53.

133. Raabe, D.; Hessling, D., Synthesis of hollow metallic particles via ultrasonic treatment of a metal emulsion. *Scripta Mater.* **2010,** *62*, 690.

134. Zhao, Y. B.; Liu, J.; Cao, L. Q.; Wu, Z. S.; Zhang, Z. J.; Dang, H. X., Synthesis and characterization of Pb-Bi bimetal nanoparticles by solution dispersion. *Mater. Chem. Phys.* **2006,** *99*, 71.

135. Zhao, Y. B.; Zhang, Z. J.; Liu, W. M.; Dang, H. X.; Xue, Q. J., Controlling synthesis of BiIn dendritic nanocrystals by solution dispersion. *J. Am. Chem. Soc.* **2004,** *126*, 6854.

136. Zhao, Y. B.; Zhang, Z. J.; Dang, H. X., A simple way to prepare bismuth nanoparticles. *Mater. Lett.* **2004,** *58*, 790.

137. Zhao, Y. B.; Zhang, Z. J.; Dang, H. X., Synthesis of In-Sn alloy nanoparticles by a solution dispersion method. *J. Mater. Chem.* **2004,** *14*, 299.

138. Zhao, Y. B.; Zhang, Z. J.; Dang, H. X., A novel solution route for preparing indium nanoparticles. *J. Phys. Chem. B* **2003,** *107*, 7574.

139. Hosseini, S. H.; Sheibani, S.; Valefi, Z., Characterisation of aluminium nanopowder produced by evaporation-condensation method. *Mater. Sci. Technol.* **2010,** *26*, 1207.

140. Gafner, S. L.; Gafner, Y. Y., Analysis of gas-phase condensation of nickel nanoparticles. *J. Exp. Theor. Phys.* **2008,** *107*, 712.

141. Raffi, M.; Rumaiz, A. K.; Hasan, M. M.; Shah, S. I., Studies of the growth parameters for silver nanoparticle synthesis by inert gas condensation. *J. Mater. Res.* **2007,** *22*, 3378.

142. Glaspell, G.; Abdelsayed, V.; Saoud, K. M.; El-Shall, M. S., Vapor-phase synthesis of metallic and intermetallic nanoparticles and nanowires: Magnetic and catalytic properties. *Pure Appl. Chem.* **2006,** *78*, 1667.

143. Semaltianos, N. G., Nanoparticles by Laser Ablation. *Crit. Rev. Solid State Mater. Sci.* **2010,** *35*, 105.

144. Ganeev, R. A.; Ryasnyanskiy, A. I.; Chakravarty, U.; Naik, P. A.; Srivastava, H.; Tiwari, M. K.; Gupta, P. D., Structural, optical, and nonlinear optical properties of indium nanoparticles prepared by laser ablation. *Appl. Phys. B: Lasers Opt.* **2007,** *86*, 337.

145. Tsuda, T.; Yoshii, K.; Torimoto, T.; Kuwabata, S., Oxygen reduction catalytic ability of platinum nanoparticles prepared by room-temperature ionic liquid-sputtering method. *J. Power Sources* **2010,** *195*, 5980.

146. Shishino, Y.; Yonezawa, T.; Kawai, K.; Nishihara, H., Molten matrix sputtering synthesis of water-soluble luminescent Au nanoparticles with a large Stokes shift. *Chem. Commun.* **2010,** *46*, 7211.

147. Rao, N. S.; Pathak, A. P.; Sathish, N.; Devaraju, G.; Saikiran, V.; Kulriya, P. K.; Agarwal, D. C.; Saravanan, G. S.; Avasthi, D. K., Synthesis of Ge nanocrystals by atom beam sputtering and subsequent rapid thermal annealing. *Solid State Commun.* **2010,** *150*, 2122.

148. Christodoulides, J. A.; Shevchenko, N. B.; Hadjipanayis, G. C., Preparation of Dy and Mn nanoparticles. *Nanostruct. Mater.* **1999,** *12*, 539.

149. Weber-Bargioni, A.; Schwartzberg, A.; Schmidt, M.; Harteneck, B.; Ogletree, D. F.; Schuck, P. J.; Cabrini, S., Functional plasmonic antenna scanning probes fabricated by induced-deposition mask lithography. *Nanotechnology* **2010,** *21*.

150. Rezaee, A.; Aliganga, A. K. A.; Pavelka, L. C.; Mittler, S., Control of the average spacing between aligned gold nanoparticles by varying the FIB dose. *Phys. Chem. Chem. Phys.* **2010,** *12*, 4104.

151. Xu, Q.; Rioux, R. M.; Whitesides, G. M., Fabrication of complex metallic nanostructures by nanoskiving. *ACS Nano* **2007,** *1*, 215.

152. Fischbein, M. D.; Drndic, M., Sub-10 nm device fabrication in a transmission electron microscope. *Nano Lett.* **2007,** *7*, 1329.

153. Aizawa, M.; Buriak, J. M., Block copolymer templated chemistry for the formation of

metallic nanoparticle arrays on semiconductor surfaces. *Chem. Mater.* **2007,** *19*, 5090.

154. Negishi, R.; Hasegawa, T.; Terabe, K.; Aono, M.; Ebihara, T.; Tanaka, H.; Ogawa, T., Fabrication of nanoscale gaps using a combination of self-assembled molecular and electron beam lithographic techniques. *Appl. Phys. Lett.* **2006,** *88*.

155. Chang, Y.; Huang, S. X.; Chen, Y., Biomolecular nanopatterning by electrophoretic printing lithography. *Small* **2009,** *5*, 63.

156. Lieberzeit, P. A.; Afzal, A.; Podlipna, D.; Krassnig, S.; Blumenstock, H.; Dickert, F. L., Printing materials in micro- and nano-scale: Systems for process control. *Sens. Actuators, B* **2007,** *126*, 153.

157. Ruda, H. E.; Polanyi, J. C.; Yang, J. S. Y.; Wu, Z.; Philipose, U.; Xu, T.; Yang, S.; Kavanagh, K. L.; Liu, J. Q.; Yang, L.; Wang, Y.; Robbie, K.; Yang, J.; Kaminska, K.; Cooke, D. G.; Hegmann, F. A.; Budz, A. J.; Haugen, H. K., Developing 1D nanostructure arrays for future nanophotonics. *Nanoscale Res. Lett.* **2006,** *1*, 99.

158. Wang, Y. L.; Xia, Y. N., Bottom-up and top-down approaches to the synthesis of monodispersed spherical colloids of low melting-point metals. *Nano Lett.* **2004,** *4*, 2047.

159. Li, Z. W.; Tao, X. J.; Cheng, Y. M.; Wu, Z. S.; Zhang, Z. J.; Dang, H. X., A simple and rapid method for preparing indium nanoparticles from bulk indium via ultrasound irradiation. *Mat. Sci. Eng. A-Struct.* **2005,** *407*, 7.

160. Ataee-Esfahani, H.; Wang, L.; Nemoto, Y.; Yamauchi, Y., Synthesis of bimetallic Au@Pt nanoparticles with Au core and nanostructured Pt shell toward highly active electrocatalysts. *Chem. Mater.* **2010,** *22*, 6310.

161. Stöber, W.; Fink, A.; Bohn, E., Controlled growth of monodisperse silica spheres in the

micron size range. *J. Colloid Interface Sci.* **1968,** *26*, 62.

162. Song, Y. Y.; Cao, X. B.; Guo, Y.; Chen, P.; Zhao, Q. R.; Shen, G. Z., Fabrication of mesoporous CdTe/ZnO@SiO_2 core/shell nanostructures with tunable dual emission and ultrasensitive fluorescence response to metal ions. *Chem. Mater.* **2009,** *21*, 68.

163. Darbandi, M.; Lu, W. G.; Fang, J. Y.; Nann, T., Silica encapsulation of hydrophobically ligated PbSe nanocrystals. *Langmuir* **2006,** *22*, 4371.

164. Liu, S. H.; Han, M. Y., Silica-coated metal nanoparticles. *Chem-Asian J.* **2010,** *5*, 36.

165. Liz-Marzan, L. M.; Giersig, M.; Mulvaney, P., Synthesis of nanosized gold-silica core-shell particles. *Langmuir* **1996,** *1996*, 4329.

166. Zhan, Q.; et al., A study of mesoporous silica-encapsulated gold nanorods as enhanced light scattering probes for cancer cell imaging. *Nanotechnology* **2010,** *21*, 055704.

167. Liong, M.; Lu, J.; Kovochich, M.; Xia, T.; Ruehm, S. G.; Nel, A. E.; Tamanoi, F.; Zink, J. I., Multifunctional inorganic nanoparticles for imaging, targeting, and drug delivery. *ACS Nano* **2008,** *2*, 889.

168. Morales, J. M.; Latorre, J.; Guillem, C.; Beltrán-Porter, A.; Beltrán-Porter, D.; Amorós, P., Scale-up low-cost synthesis of bimodal mesoporous silicas. *Solid State Sci.* **2005,** *7*, 415.

169. Jung, C. Y.; Kim, J. S.; Chang, T. S.; Kim, S. T.; Lim, H. J.; Koo, S. M., One-step synthesis of structurally controlled silicate particles from sodium silicates using a simple precipitation process. *Langmuir* **2010,** *26*, 5456.

170. Landfester, K.; Weiss, C., Encapsulation by miniemulsion polymerization. In *Modern Techniques for Nano- and Microreactors/-reactions*, Caruso, F., Ed. Springer Berlin / Heidelberg: 2010; Vol. 229, pp 1.

171. Montenegro, R.; Antonietti, M.; Mastai, Y.; Landfester, K., Crystallization in miniemulsion droplets. *J. Phys. Chem. B* **2003,** *107*, 5088.

172. Aschenbrenner, E. M.; Weiss, C. K.; Landfester, K., Enzymatic esterification in aqueous miniemulsions. *Chem. Eur. J.* **2009,** *15*, 2434.

173. Rossmanith, R.; Weiss, C. K.; Geserick, J.; Hüsing, N.; Hörmann, U.; Kaiser, U.; Landfester, K., Porous anatase nanoparticles with high specific surface area prepared by miniemulsion technique. *Chem. Mater.* **2008,** *20*, 5768.

174. Landfester, K., Miniemulsion polymerization and the structure of polymer and hybrid nanoparticles. *Angew. Chem. Int. Ed.* **2009,** *48*, 4488.

175. Weiss, C. K.; Kohnle, M.-V.; Landfester, K.; Hauk, T.; Fischer, D.; Schmitz-Wienke, J.; Mailänder, V., The first step into the brain: uptake of NIO-PBCA nanoparticles by endothelial cells in vitro and in vivo, and direct evidence for their blood–brain barrier permeation. *ChemMedChem* **2008,** *3*, 1395.

176. Tiarks, F.; Landfester, K.; Antonietti, M., Preparation of polymeric nanocapsules by miniemulsion polymerization. *Langmuir* **2001,** *17*, 908.

177. Luo, Y.; Zhou, X., Nanoencapsulation of a hydrophobic compound by a miniemulsion polymerization process. *J. Polym. Sci., Part A: Polym. Chem.* **2004,** *42*, 2145.

178. Cao, Z.; Shan, G., Synthesis of polymeric nanocapsules with a crosslinked shell through interfacial miniemulsion polymerization. *J. Polym. Sci., Part A: Polym. Chem.* **2009,** *47*, 1522.

179. Ni, K.-F.; Shan, G.-R.; Weng, Z.-X., Synthesis of hybrid nanocapsules by miniemulsion (co)polymerization of styrene and γ-methacryloxypropyltrimethoxysilane. *Macromolecules* **2006,** *39*, 2529.

180. Paiphansiri, U.; Tangboriboonrat, P.; Landfester, K., Polymeric Nanocapsules Containing an Antiseptic Agent Obtained by Controlled Nanoprecipitation onto Water-in-Oil Miniemulsion Droplets. *Macromol. Biosci.* **2006,** *6*, 33.

181. Knoll, M., Aufladepotentiel und Sekundäremission elektronenbestrahlter Körper. *Zeitschrift für technische Physik* **1935,** *16*.

182. http://www.hhtc.ca/microscopes/sem/s5500.htm.

183. Roussel, L. Y.; Debbie, J. S.; Gestmanna, I.; Darusb, M.; Young, R. J., Extreme high resolution scanning electron microscopy (XHR SEM) and beyond. *Proc. of SPIE* **2009,** *7387*, 73870W.

184. Yan, Z., General thermal wavelength and its applications. *Eur. J. Phys.* **2000,** *21*, 625.

185. Iriarte, G. F., Using Transmission Electron Microscopy (TEM) for chemical analysis of semiconductors. *Microscopy: Sci. Tech. Appl. Edu.* **2010**, 1888.

186. Cross, S. E.; Jin, Y.-S.; Rao, J.; Gimzewski, J. K., Nanomechanical analysis of cells from cancer patients. *Nat. Nano.* **2007,** *2*, 780.

187. Deufrene, Y. F., Atomic force microscopy and chemical force microscopy of microbial cells. *Nat. Protoc.* **2008,** *3*, 1132.

188. Touhami, A.; Nysten, B.; Dufrene, Y. F., Nanoscale mapping of the elasticity of microbial cells by atomic force microscopy. *Langmuir* **2003,** *19*, 4539.

189. Hlady, V.; Pierce, M.; Pungor, A., Novel method of measuring cantilever deflection during an AFM force measurement. *Langmuir* **1996,** *12*, 5244.

190. Radmacher, M., Chapter 4 Measuring the elastic properties of living cells by the atomic force microscope. In *Methods in Cell Biology*, Academic Press: 2002; Vol. 68, p 67.

191. Tomasetti, E.; Legras, R.; Nysten, B., Quantitative approach towards the measurement of polypropylene/(ethylene-propylene) copolymer blends surface elastic properties by AFM. *Nanotechnology* **1998,** *4*, 305.

192. Weisenhorn, A. L.; Khorsandi, M.; Kasas, S.; Gotzos, V.; Butt, H.-J., Deformation and height anomaly of soft surfaces studied with an AFM. *Nanotechnology* **1993,** *4*, 106.

193. Moran, M. J., X-ray generation by the Smith-Purcell effect. *Phys. Rev. Lett.* **1992,** *69*, 2523.

194. Goldstein, J. L., *Scanning electron microscopy and x-ray microanalysis*. 3rd ed.; Springer: New York, 2003.

195. Prati, S.; Joseph, E.; Sciutto, G.; Mazzeo, R., New advances in the application of FTIR microscopy and spectroscopy for the characterization of artistic materials. *Acc. Chem. Res.* **2010,** *43*, 792.

196. Prati, S.; Joseph, E.; Sciutto, G.; Mazzeo, R., New advances in the application of FTIR microscopy and spectroscopy for the characterization of artistic materials. *Acc. Chem. Res.* **2008,** *43*, 792.

197. Karr, C.; Kovach, J. J., Far-Infrared Spectroscopy of Minerals and Inorganics. *Appl. Spectrosc.* **1968,** *23*, 219.

198. Nyquist, R. A.; Kagel, R. O., *Infrared spectra of inorganic compounds (3800-45 cm^{-1})*. Academic: New York, 1971.

199. http://en.wikipedia.org/wiki/Table_of_standard_electrode_potentials#cite_note-van-1.

200. Bard, A. J.; Parsons, R.; Jordan, J., *Standard Potentials in Aqueous Solutions*. Marcel Dekker: New York, 1985.

201. Vanýsek, P., *Handbook of Chemistry and Physics*. 88th ed.; CRC Press: 2007.

202. Lim, T. H.; Ingham, B.; Kamarudin, K. H.; Etchegoin, P. G.; Tilley, R. D., Solution Synthesis of Monodisperse Indium Nanoparticles and Highly Faceted Indium Polyhedra. *Crystal Growth & Design* **2010,** *10*, 3854.

203. Sister, V.; Bokach, D.; Fateev, V.; Kostin, V., Prospects for making minifuel elements. *Chem. Petrol. Eng.* **2006,** *42*, 51.

204. Tan, L. P.; Yue, C. Y.; Tam, K. C.; Lam, Y. C.; Hu, X., Effects of shear rate, viscosity ratio and liquid crystalline polymer content on morphological and mechanical properties of polycarbonate and LCP blends. *Polymer Int.* **2002,** *51*, 398.

205. Mendez-Villuendas, E.; Bowles, R. K., Surface nucleation in the freezing of gold nanoparticles. *Phys. Rev. Lett.* **2007,** *98*, 185503.

206. Schmelzer, J., *Nucleation Theory and Applications*. Wiley-VCH: New York, 2005.

207. Keblinski, P.; Prasher, R.; Eapen, J., Thermal conductance of nanofluids: is the controversy over? *J. Nanopart. Res.* **2008,** *10*, 1089.

208. Khodadadi, J. M.; Hosseinizadeh, S. F., Nanoparticle-enhanced phase change materials (NEPCM) with great potential for improved thermal energy storage. *Int. Comm. Heat Mass Transfer* **2007,** *34*, 534.

209. Arico, A. S.; Bruce, P.; Scrosati, B.; Tarascon, J.-M.; Van Schalkwijk, W., Nanostructured materials for advanced energy conversion and storage devices. *Nature Mater.* **2005,** *4*, 366.

210. Kannan, R. Y.; Salacinski, H. J.; Butler, P. E.; Seifalian, A. M., Polyhedral oligomeric silsesquioxane nanocomposites: the next generation material for biomedical applications. *Acc.*

Chem. Res. **2005,** *38*, 879.

211.Gittins, D. I.; Bethell, D.; Schiffrin, D. J.; Nichols, R. J., A nanometre-scale electronic switch consisting of a metal cluster and redox-addressable groups. *Nature* **2000,** *408*, 67.

212. Trindade, T.; O'Brien, P.; Pickett, N. L., Nanocrystalline semiconductors: synthesis, properties, and perspectives. *Chem. Mater.* **2001,** *13*, 3843.

213. Graf, C.; Blaaderen, A. V., Metallodielectric colloidal core-shell particles for photonic applications. *Langmuir* **2002,** *18*, 524.

214. Velikov, K. P.; Moroz, A.; Blaaderen, A. V., Photonic crystals of core-shell colloidal particles. *Appl. Phys. Lett.* **2002,** *80*, 49.

215. Daniel, M.-C.; Astruc, D., Gold nanoparticles: assembly, supramolecular chemistry, quantum-size-related properties, and applications toward biology, catalysis, and nanotechnology. *Chem. Rev.* **2004,** *104*, 293.

216. Gao, J.; Gu, H.; Xu, B., Multifunctional magnetic nanoparticles: design, synthesis, and biomedical applications. *Acc. Chem. Res.* **2009,** *42*, 1097.

217. Lu, A.; Salabas, E. L.; Schüth, F., Magnetic nanoparticles: synthesis, protection, functionalization, and application. *Angew. Chem. Int. Ed.* **2007,** *46*, 1222.

218. Elghanian, R.; Storhoff, J. J.; Mucic, R. C.; Letsinger, R. L.; Mirkin, C. A., Selective colorimetric detection of polynucleotides based on the distance-dependent optical properties of gold nanoparticles. *Science* **1997,** *277*, 1078.

219. Faucheu, J.; Gauthier, C.; Chazeau, L.; Cavaillé, J.-Y.; Mellon, V.; Lami, E. B., Miniemulsion polymerization for synthesis of structured clay/polymer nanocomposites: short review and recent advances. *Polymer* **2010,** *51*, 6.

220. Hoeppener, S.; Maoz, R.; Cohen, S. R.; Chi, L. F.; Fuchs, H.; Sagiv, J., Metal nanoparticles, nanowires, and contact electrodes self-assembled on patterned monolayer templates - a bottom-up chemical approach. *Adv. Mater.* **2002,** *14*, 1036.

221. Wang, Y.; Xia, Y., Bottom-up and top-down approaches to the synthesis of monodipersed spherical colloids of low melting-point metals. *Nano Lett.* **2004,** *4*, 2047.

222. Schmid, G.; Corain, B., Nanoparticulated gold: syntheses, structures, electronics, and reactivities. *Eur. J. Inorg. Chem.* **2003,** *2003*, 3081.

223. Cairns, D. B.; Khan, M. A.; Perruchot, C.; Riede, A.; Armes, S. P., Synthesis and characterization of polypyrrole-coated poly(alkyl methacrylate) latex particles. *Chem. Mater.* **2003,** *15*, 233.

224. Zhang, J.; Tang, Y.; Weng, L.; Ouyang, M., Versatile strategy for precisely tailored core@shell nanostructures with single shell layer accuracy: the case of metallic shell. *Nano Lett.* **2009,** *9*, 4061.

225. Richardson, H. H.; Carlson, M. T.; Tandler, P. J.; Hernandez, P.; Govorov, A. O., Experimental and theoretical studies of light-to-heat conversion and collective heating effects in metal nanoparticle solutions. *Nano Lett.* **2009,** *9*, 1139.

226. Goel, M.; Roy, S. K.; Sengupta, S., Laminar forced convection heat transfer in microcapsulated phase change materials suspensions. *Int. J. Heat Mass Transfer* **1994,** *37*, 593.

227. Graf, C.; Vossen, D. L. J.; Imhof, A.; Blaaderen, A. V., A general method to coat colloidal particles with silica. *Langmuir* **2003,** *19*, 6693.

228. Tiarks, F.; Landfester, K.; Antonietti, M., Preparation of polymeric nanocapsules by miniemulsion polymerization. *Langmuir* **2001,** *17*, 908.

229. Jin, Z.; Wang, Y.; Liu, J.; Yang, Z., Synthesis and properties of paraffin capsules as phase change materials. *Polymer* **2008,** *49*, 2903.

230. Digilov, R. M.; Reiner, M., Mass-controlled capillary viscometer for a newtonian liquid: viscosity of water at different temperatures. *Rev. Sci. Instrum.* **2007,** *78*, 035112.

231. Joo, S. H.; Park, J. Y.; Tsung, C.-K.; Yamada, Y.; Yang, P.; Somorjai, G. A., Thermally stable pt/mesoporous silica core-shell nanocatalysts for high-temperature reactions. *Nature Mater.* **2009,** *8*, 126.

232. Narasimhan, A.; Lage, J. L., Modified Hazen-Dupuit-Darcy model for forced convection of a fluid with temperature-dependent viscosity. *J. Heat Transfer* **2001,** *123*, 31.

233. Incropera, F. P.; Dewitt, D. P., *Introduction to Heat Transfer*. 3rd ed.; John Wiley & Sons: New York, 1996.

234. Alvarado, J. L.; Marsh, C.; Sohn, C.; Vilceus, M.; Hock, V.; Phetteplace, G.; Newell, T., Characterization of supercooling suppression of microencapsulated phase change material by using DSC. *J. Therm. Anal. Calorim.* **2006,** *86*, 505.

235. Faucheux, M.; Muller, G.; Havet, M.; LeBail, A., Influence of surface roughness on the supercooling degree: Case of selected water/ethanol solutions frozen on aluminum surfaces. *Int. J. Refrig.* **2006,** *29*, 1218.

236. Fan, Y. F.; Zhang, X. X.; Wang, X. C.; Li, J.; Zhu, Q. B., Super-cooling prevention of microencapsulated phase change material. *Thermochim. Acta* **2004,** *413*, 1.

237. Tong, H. Y.; Shi, F. G., Abrupt discontinuous relationships between supercooling and melt overheating. *Appl. Phys. Lett.* **1996,** *70*, 841.

238. Turnbull, D., Kinetics of heterogeneous nucleation. *J. Chem. Phys.* **1950,** *18*, 198.

239. Zhang, J. T.; Wang, Y. N., Mechanism to diminish the supercooling of the tin freezing point by using graphite powder. *Int. J. Thermophys.* **2008,** *29*, 844.

240. Israelachvili, J. N., *Intermolecular and Surface Forces* 2nd ed.; Elsevier Science: Oxford, 1991.

241. Murashov, V. V.; Demchuk, E., Surface sites and unrelaxed surface energies of tetrahedral silica polymorphs and silicate. *Surf. Sci.* **2005,** *595*, 6.

242. Vitos, L.; Ruban, A. V.; Skriver, H. L.; Kollár, J., The surface energy of metals. *Surf. Sci.* **1998,** *411*, 186.

243. Wang, G.; Harrison, I. R., Polymer melting: heating rate effects on DSC melting peaks. *Thermochim. Acta* **1994,** *231*, 203.

244. Surianarayanan, M.; Vijayaraghavan, R.; Swaminathan, G.; Rao, P. G., Microcalorimetry and its role in thermal hazard quantification. *Curr. Sci.* **2001,** *80*, 738.

245. Ohgushi, T.; Komarneni, S.; Bhalla, A. S., Mechanism of microwave heating of zeolite A. *J. Porous Mater.* **2001,** *8*, 23.

246. Shukla, P. K.; Pushpavanam, S., Parametric sensitivity, runaway, and safety in batch reactors - experiments and models. *Ind. Eng. Chem. Res.* **1994,** *33*, 3202.

247. Vijayaraghavan, R.; Surianarayanan, M.; Armel, V.; MacFarlane, D. R.; Sridhar, V. P., Exothermic and thermal runaway behaviour of some ionic liquids at elevated temperatures. *Chem. Commun.* **2009**, 6297.

248. Mandal, B. K.; Padhi, A. K.; Shi, Z.; Chakraborty, S.; Filler, R., Thermal runaway inhibitors for lithium battery electrolytes. *J. Power Sources* **2006,** *161*, 1341.

249. Balakotaiah, V.; Kodra, D.; Nguyen, D., Runaway limits for homogeneous and catalytic

reactors. *Chem. Eng. Sci.* **1995,** *50*, 1149.

250. Bos, A. N. R.; Vandebeld, L.; Overkamp, J. B.; Westerterp, K. R., Behavior of an adiabatic packed-bed reactor. 1. experimetal-study. *Chem. Eng. Commun.* **1993,** *121*, 27.

251. Verhoeff, J.; Vandenberg, P. J., Thermal runaway in the thermal - explosion of a liquid. *J. Therm. Anal.* **1984,** *29*, 533.

252. Maider, A.; Jose, R. L.; Jose, M. A., Safety in emulsion polymerization reactors: an experimental study. *Macromol. Mater. Eng.* **2005,** *290*, 242.

253. Albert, J.; Luft, G., Runaway phenomena in the ethylene/vinylacetate copolymerization under high pressure. *Chem. Eng. Process.* **1998,** *37*, 55.

254. Henda, R.; Machac, A.; Nilsson, B., Heat and mass transport in a nonlinear fixed-bed catalytic reactor: Hot spots and thermal runaway. *Chem. Eng. J.* **2008,** *143*, 195.

255. Frikha, N.; Schaer, E.; Houzelot, J. L., Experimental study and modelling of thermal runaway: Application to dichromate catalysed hydrogen peroxide decomposition. *Thermochim. Acta* **2006,** *449*, 47.

256. Vanhove, D., Catalyst testing at a lab scale in mild oxidation: Can you control the reaction temperature? *Appl. Catal., A* **1996,** *138*, 215.

257. Quina, M. M. J.; Ferreira, R. M. Q., Thermal runaway conditions of a partially diluted catalytic reactor. *Ind. Eng. Chem. Res.* **1999,** *38*, 4615.

258. Velo, E.; Bosch, C. M.; Recasens, F., Thermal safety of batch reactors and storage tanks. Development and validation of runaway boundaries. *Ind. Eng. Chem. Res.* **1996,** *35*, 1288.

259. Bashir, S.; Chovan, T.; Masri, B. J.; Mukherjee, A.; Pant, A.; Sen, S.; Vijayaraghavan, P.; Berty, J. M., Thermal runaway limit of tubular reactors, defined at the inflection point of the

temperature profile. *Ind. Eng. Chem. Res.* **1992,** *31*, 2164.

260. Vesligaj, M. J.; Amon, C. H., Transient thermal management of temperature fluctuations during time varying workloads on portable electronics. *IEEE T. Compon. Pack. T.* **1999,** *22*, 541.

261. Welnic, W.; Pamungkas, A.; Detemple, R.; Steimer, C.; Blugel, S.; Wuttig, M., Unravelling the interplay of local structure and physical properties in phase-change materials. *Nature Mater.* **2006,** *5*, 56.

262. Wan, A.; Yeh, C.-T., Ignition of methanol partial oxidation over supported platinum catalyst. *Catal. Today* **2007,** *129*, 293.

263. Tesser, R.; Di Serio, M.; Santacesaria, E., Catalytic oxidation of methanol to formaldehyde: an example of kinetics with transport phenomena in a packed-bed reactor. *Catal. Today* **2003,** *77*, 325.

264. Li, X.-R.; Koseki, H., Thermal decomposition kinetic of liquid organic peroxides. *J. Loss Prev. Process Ind.* **2005,** *18*, 460.

265. Traxel, B. E.; Hohn, K. L., Partial oxidation of methanol at millisecond contact times. *Appl. Catal., A* **2003,** *244*, 129.

266. Tester, J. W.; Webley, P. A.; Holgate, H. R., Revised global kinetic measurements of methanol oxidation in supercritical water. *Ind. Eng. Chem. Res.* **1993,** *32*, 236.

267. Frese, K. W.; Chen, C., Methanol oxidation at p-Si/Pt electrodes. evidence for hot hole reactivity. *J. Phys. Chem.* **1995,** *99*, 6074.

268. McCabe, R. W.; McCready, D. F., Kinetics and reaction pathways of methanol oxidation on platinum. *J. Phys. Chem.* **1986,** *90*, 1428.